

Measuring Dijets From Ultra-Peripheral Heavy Ion Collisions

By

James Bowen

Submitted to the graduate degree program in Department of Physics and Astronomy and the Graduate Faculty of the University of Kansas in partial fulfillment of the requirements for the degree of Doctor of Philosophy.

Murray, Michael J., Chairperson

Baringer, Philip S.

Committee members

Fischer, Christopher

Lerner, David

Tapia Takaki, Daniel

Date defended: 3 July 2018

The Thesis Committee for James Bowen certifies
that this is the approved version of the following thesis :

Measuring Dijets From Ultra-Peripheral Heavy Ion Collisions

Murray, Michael J., Chairperson

Date approved: 25 July 2018

Abstract

The Compact Muon Solenoid Experiment measured dijets produced in photon-nuclear collisions using data taken at the Large Hadron Collider in late 2015. Dijet measurements are potentially useful in constraining the gluon density over a wide range of x and Q , which is needed in order to measure the quark-gluon plasma viscosity and to search for the color-glass condensate. Recently it has been suggested by several theoretical groups that photon induced dijets can also be used to examine the correlation between the gluons in the nucleus. This analysis focused on the latter, examining azimuthal correlations between the total transverse momentum of the dijets and the momentum difference of the dijets. Following the prescription suggested by theorists, a positive correlation was found.

Acknowledgements

The following is a list of people and organizations without whom I could not have completed this analysis and dissertation:

The University of Kansas, and the Physics Department in particular, for giving me this opportunity.

Mr. Robert Curry, for making my teaching experience as a graduate student a valuable learning experience.

My Physics 114 and 115 laboratory students from 2011 to 2015, for making my teaching experience as a graduate student rewarding and worthwhile.

Christopher R. E. Bruner, Ph.D., for teaching me how to use essential analysis tools.

Ramona Vogt, Ph.D., for developing the theoretical foundations of this analysis and for early assistance in preparations to undertake this measurement in CMS.

Professor Daniel Tapia Takaki, Ph.D.; Samuel Boren, Ph.D.; and R. Patrick Kenny, Ph.D.; for developing the experimental triggers needed to conduct this measurement in CMS.

The United States Navy, the Office of Naval Reactors/Naval Nuclear Propulsion Program, and the Naval Oceanographic Office, for providing direct employment during my studies and for providing me a fellowship that made possible my research in residence at CERN and the post-candidacy phase of my research. With regard to the fellowship, I would specifically like to thank the following for their direct assistance in my attainment of it: Major Jacque Torson, Nebraska Air National Guard/USAFR; Captain Jeanne Pricer, USNR; Lieutenant Commander David P. Montague, USN (Ret.); Senior Chief Sonar Technician Shawn Eddings, USN (Ret.); and Professor F. Marty Ytreberg, Ph.D.

Quan Wang, Ph.D., for extraordinary assistance in the use and implementation of analysis tools as well as logistical support while I was in residence at CERN.

Zhoudunming Tu, Ph.D., for assisting me in the implementation of tools needed to start this analysis.

Marta Verweij, Ph.D., for instructing me in techniques needed for this analysis.

Professor Alice C. Mignerey, Ph.D., for providing the reference data from 2010 that was needed to calibrate the ZDC.

Ayman Al-bataineh, Ph.D., for providing graphics needed in describing this analysis.

My fellow graduate students in the nuclear physics research group, James Castle, Will McBrayer, and Samuel Boren, for their help and support.

Professor Michael J. Murray, Ph.D., my advisor, for introducing me to this research and for incalculable teaching and support in ways that are too numerous to mention here.

Elizabeth L. S. Bowen, J.D., for editing this dissertation.

Finally, my parents, Richard L. Bowen, Ph.D., and Connie S. Bowen; and the rest of my family for their sacrifices and support over the course of my lifetime, which laid the foundation for this effort; as well as for their extensive support during my work on this analysis.

Contents

1	Introduction	1
2	Theory	4
2.1	Quantum Chromo-Dynamics	4
2.2	Electromagnetic Interactions in Ultra-Peripheral Heavy Ion Collisions	14
2.2.1	Electromagnetic Fields of Relativistic Heavy Ions	15
2.2.2	Photon Flux of Relativistic Heavy Ions	27
2.3	Hadronic Jets From Ultra-Peripheral Heavy Ion Collisions	30
2.4	Using UPC Jets To Examine Gluon Correlations	38
3	The Compact Muon Solenoid Experiment Part I: Experimental Apparatus	40
3.1	The Large Hadron Collider	40
3.2	Basic Detector Principles	47
3.3	The CMS Detector Complex	51
3.3.1	The Solenoid Magnet	53
3.3.2	The Silicon Tracker	54
3.3.3	The Electromagnetic Calorimeter	56
3.3.4	The Hadronic Calorimeter	59
3.3.5	The Zero Degree Calorimeter	66
3.3.6	CASTOR	70
3.3.7	Muon Detector/Tracker System	71
4	The Compact Muon Solenoid Experiment Part II: Analysis Techniques	75
4.1	Triggering and Data Gathering	75

4.2	The Particle Flow Algorithm	76
4.3	The Anti- k_T Algorithm	80
5	ZDC Calibration and Analysis	82
6	Data Analysis	96
6.1	Checking the Jet Energy Scale	96
6.2	Selecting Exclusive UPC Dijets	97
6.3	The Pseudorapidity Gap	105
6.4	Azimuthal Correlation Analysis	107
7	Cross Checks and Systematic Uncertainties	120
7.1	Comparing Forward and Backward Events	121
7.2	Varying the Exclusivity Parameter α	123
7.3	Varying the Back to Back Requirement $ \Delta\phi $	124
7.4	Varying the Vertex Requirement $ v_z $	125
7.5	Examination of Effect of Setting Limit on Conjugate ZDC	125
7.6	Systematic Analysis Results	126
8	Results and Conclusion	131

List of Figures

1.1	(courtesy of Michael J. Murray) Range of x and Q^2 (denoted as M^2 in the figure) for the LHC, RHIC, and SPS.	3
2.1	([30], 276) Two separate quarks fragment into jets. Note the link between them that ensures color neutralization.	8
2.2	([44], 66) Deep inelastic scattering: an electron scatters off of a proton. The electron emits a virtual photon, which transfers momentum between the electron and a charged parton within the proton.	10
2.3	([44], 14) Branches of a $2 \rightarrow 2$ scattering event.	11
2.4	([44], 84) Proton parton distribution functions as a function of x at $Q^2 = 10 \text{ GeV}^2/c^2$. The parton distribution functions are fits to data, and are represented as follows: solid = valence u quark, dashed = valence d quark, dot-dashed = sea u and \bar{u} quarks, dotted = sea d and \bar{d} quarks, dot-dot-dot-dashed = sea s and \bar{s} quarks, and dash-dash-dash-dotted = gluons. The gluon distribution has been divided by 10. Note how rapidly the gluon density increases as x decreases.	12
2.5	([36], 84) Phase diagram of known and QCD-hypothesized states of strong nuclear-interacting matter is shown here. Experiments at RHIC and the LHC take place in high temperature but low density regions that resemble conditions that existed throughout the universe shortly after the Big Bang. Color superconductor refers to extremely dense states of strong nuclear-interacting matter that form spin-0 pairs and behave like bosons.	13
2.6	([29], 440) The electric field lines of a point charge moving at a relativistic speed are shown here.	14

2.7	([29], 529) Coordinate axes for three inertial reference frames, S_o , S , and \bar{S} , and their speeds with respect to each other.	16
2.8	([29], 526) Parallel plate capacitor shown in frame S_o (a) and in frame S (b).	17
2.9	([29], 527) Parallel plate capacitor aligned with the yz plane.	18
2.10	([29], 530) Parallel plate capacitor aligned with the xy plane.	21
2.11	([29], 531) A long solenoid.	22
2.12	([29], 528) Diagram of a point charge in motion with respect to an arbitrary point P	24
2.13	([29], 440) The electric field lines of a point charge moving at a relativistic speed flatten out like a pancake perpendicular to the charge velocity.	26
2.14	([29], 440) The magnetic field lines of a point charge circle the direction of charge velocity, with increasing magnitude closer to the charge.	27
2.15	([35], 726) The radiation of a point charge passing in proximity to an area of space in frame S can be modeled as two pulses P_1 and P_2	29
2.16	(Courtesy of Ayman Al-bataineh) Conceptual diagram of an ultra-peripheral collision that produces dijets. In this diagram, $n_{Pb} = \frac{dl}{d\omega}$ (as defined in Section 2.2) and R is the nuclear radius.	31
2.17	([43], 1) Feynman diagram of an inclusive UPC resulting in dijets. A photon with momentum fraction x_1 from one nuclide A is absorbed by the second identical nuclide A , where quantum field fluctuations cause it to interact with a gluon of momentum fraction x_2 , and dijets with equal in magnitude and opposite in direction p_T result.	32
2.18	([43], 2) Predicted UPC dijet production rate for a Pb-Pb run of 10^6 seconds at luminosity $0.42 \times 10^{27} cm^{-2}s^{-1}$ and $\sqrt{S_{NN}} = 5.5$ TeV. Rates are in counts per bin of ± 1 GeV and $\pm 0.25x_2$	37
2.19	(Prediction specifics provided courtesy of Ramona Vogt) Predicted dijet yield as a function of p_T for a Pb-Pb run of 10^6 seconds at luminosity $0.42 \times 10^{27} cm^{-2}s^{-1}$ and $\sqrt{S_{NN}} = 5.5$ TeV.	38

2.20	([32], 2) A Feynman diagram of exclusive UPC dijet production is shown here. A $q\bar{q}$ pair interacts with a gluon pair of net color zero, resulting in a dijet with no net color or electric charge exchanged.	39
3.1	([2]) Location of LHC and experiments in the vicinity of Geneva, Switzerland. . .	41
3.2	([25], 13) Diagram of LHC and its feeder accelerators and supporting equipment. .	42
3.3	([47], 147) Diagram of a cylindrically-shaped RF cavity. The geometry with cylindrical coordinates is shown on the left. The right shows a side-view cross section, where the cavity has length h and radius r_o . Also visible on the right is the beam inlet and outlet on each end of the cavity as well as the waveguide input at the top. .	44
3.4	([1]) Photograph of LHC RF cavities.	45
3.5	([47], 156) Diagram of a klystron. A steady stream of electrons is accelerated by a voltage across a cathode ray tube consisting of a heater, cathode, and anode. The buncher cavity receives the steady stream of electrons and electromagnetic wave signals to be amplified, which organizes the electrons into bunches. The electron bunches travel through the drift tube and arrive at the catcher cavity at the frequency of the electromagnetic wave and at such a time where the electric field in the cavity opposes their motion. The amplified electromagnetic wave is then outputted through a waveguide while the decelerated electrons end their run in the collector.	46
3.6	([3]) A cutaway diagram, with components labeled, of a dipole magnet for steering the beams in the LHC.	47
3.7	([3]) Magnetic fields of an LHC diople magnet.	48
3.8	([4], 2-56) Basic diagram of a gas-filled chamber detector.	49
3.9	([4], 2-59) Diagram of a scintillation detector. The aluminum foil in this example serves to reflect the light flashes toward the photomultiplier tube.	50
3.10	([4], 2-60) Diagram of a photomultiplier tube in a scintillation detector. In this case, a total potential of 1000 volts is applied across all of the dynodes.	51

3.11 ([11], 8) The CMS detector complex and its components. Note that the ZDCs, which are located forward of the main complex on each end, are not shown.	52
3.12 ([18], 1) Diagram of the CMS structural steel skeleton is shown here. In the barrel region, there are five wheel sections (labeled with prefix W) that run the length of the barrel. These wheel sections have three layers (L) plus one extra "tail catcher" (TC) layer in the W0 wheel (see Hadronic Calorimeter subsection below). The wheels are dodecagonal-shaped with 12 azimuthal sections (S). In the two endcap sections, there are three disks (D). The "Chimneys" are for the routing of cryogenic and electrical connections. The light blue sections are the components of the muon detector/tracker.	54
3.13 ([18], 6) CMS magnetic field magnitude (left) and flux density right at a maximum of 3.8 T inside the coil. Each field line on the right represents a magnetic flux increment of 6 Wb.	55
3.14 ([19], 3) Cross-sectional diagram of the silicon detector on one side of the beamline.	56
3.15 ([11], 18) Pseudorapidity layout and limit of the silicon tracker as shown on one quarter of the tracker.	57
3.16 ([11], 20) Layout of the pixel detector, with the three barrel layers and two endcap disks on each end clearly shown.	58
3.17 ([23], 91) An electromagnetic calorimeter PbWO_4 crystal, with photomultiplier tube attached, is shown here. This particular crystal is from the endcap section. The barrel section crystals are somewhat longer and more narrow, but are otherwise similar.	59
3.18 ([34], 33) Layout of the electromagnetic calorimeter, as shown with a one quarter section. The pseudorapidity limits of the barrel section, endcap section, and preshower device are shown. Notice the angular arrangement of the PbWO_4 crystals in the barrel and endcap sections.	60

3.19	([23], 5) Electromagnetic calorimeter energy resolution as measured with test beam. Equation 3.8, with the values of S , N , and C shown in the plot, expresses these results.	61
3.20	([23], 123) Diagram of one quarter of the CMS detector complex that shows the hadronic calorimeter and specifically the locations of HB, HO, HE, and HF. Note the pseudorapidity scale plot that is superimposed up to $\eta=3.0$.	62
3.21	([23], 143) Scintillator tiles used in the hadronic calorimeter. Note the optical fibers embedded in the tiles, which collect scintillation light and transmit it to photomultiplier tubes. These particular tiles are made of Bicron BC408 scintillator and are used in HO.	63
3.22	([23], 124) Photograph of one half of HB prior to installation. The absorber layers of brass are clearly visible, as well as the gaps between them that contain the scintillator plates.	64
3.23	([23], 138) Relative location of HO and its scintillator layers shown looking from the r-direction (left) and z-direction (right).	65
3.24	([23], 142) Layout of HO scintillator layers is shown here. The central ring has two layers on each side of the iron frame it is mounted on, the other rings have one.	66
3.25	([23], 137) Diagram of HE and its segmentation and geometry is shown here. The angles of the boundaries between the towers, shown as green dashed lines emanating from the interaction point, are given in units of pseudorapidity and degrees.	67
3.26	([23], 147) Diagram of one end of HF is shown here. The absorber is the sensitive area of HF. Other components are protected by radiation shielding.	68
3.27	([23], 148) Diagram of an HF segment is shown here. Rings and wedges define the pseudorapidity and azimuthal segmentation of HF, respectively. Ring radius and respective pseudorapidity values are shown. It can also be seen that the two innermost rings have an azimuthal angle of 20° (0.35 radians) instead of 10° (0.175 radians).	69

3.28	([7]) A quarter view of HCAL and all of its components is shown here, along with the specific segmentation of each component.	70
3.29	([23], 5) Jet transverse energy resolution for the hadronic calorimeter is shown for the given pseudorapidity ranges, roughly corresponding to HB/HO, HE, and HF, respectively.	71
3.30	([23], 159) On the left a diagram of the ZDC detector is shown. EM is at the far left. It is followed by HAD, whose 45° -angled alternating tungsten and quartz layers are clearly visible. Also visible are the 4 readout channels of HAD. A photograph of HAD is shown on the right.	72
3.31	([23], 161) ZDC energy resolution as a function of the positron test beam energy is shown here.	72
3.32	([23], 157) Location of one CASTOR detector in CMS is shown here.	73
3.33	([23], 158) Diagram of CASTOR and its components is shown here. The red arrow indicates the direction away from the interaction point from which particles emerge.	73
3.34	([11], 12) Quarter diagram of the muon system is shown here.	74
4.1	([24]) A cutaway diagram of the CMS cylinder and its subsystems.	77
4.2	([24]) A diagram of the CMS particle flow process.	78
4.3	([15], 4) A sample event where jets are identified with the anti- k_T algorithm. In this case, $R=1$. Some of the clusters here are random low k_T objects that might not be true jets. Notice how when two jet clusters overlap, which occurs when there are high k_T (p_T) particles within $R < \Delta_{12} < 2R$ of each other, the relative comparison of each particle's k_T determines how conical their respective jet clusters are.	81
5.1	Time slice signals compared between ZDC+ HAD1 and all other readout channels on ZDC+.	82
5.2	Time slice signals compared between ZDC- HAD1 and all other readout channels on ZDC-.	83

5.3	Average signal in femtocoulombs (fC) for the ZDC- signal ratios EM1+EM5/EM3, EM2+EM4/EM3, HAD2/HAD1, HAD3/HAD1, and HAD4/HAD1, respectively.	85
5.4	(Courtesy of Alice Mignerey) Average signal in femtocoulombs (labeled as counts on the y-axes) for the ZDC- signal ratios EM1+EM5/EM3, EM2+EM4/EM3, HAD2/HAD1, HAD3/HAD1, and HAD4/HAD1, respectively for 2010 LHC Pb-Pb heavy ion data.	86
5.5	ZDC+/ZDC- signal ratio vs. centrality for each readout channel of ZDC+ to their ZDC- counterparts. The red lines are the zero-order polynomial average for each readout channel ratio, the value of which is labeled in each grey box as "p0".	87
5.6	ZDC+/ZDC- signal ratio vs. centrality for each readout channel of ZDC+ to their ZDC- counterparts following application of calibration constants for ZDC+ channels listed in Table 5.4.	90
5.7	ZDC+/ZDC- signal ratio vs. centrality for each readout channel of ZDC+ to their ZDC- counterparts following application of the final calibration constants for ZDC+ channels listed in Table 5.5.	92
5.8	Average ZDC signal per event vs. data run number in the 2015 CMS LHC heavy ion run data run is shown here, with ZDC+ signal where HF+ was > 5 GeV and HF- was < 5 GeV in the first column, and ZDC- signal where the energy deposited in HF- was > 5 GeV and HF+ was < 5 GeV in the second column. In the top row, the p0 averages for three groups of data runs show consistent differences in the ZDC signal strength in each of these groups on both ZDC+ and ZDC-, particularly with the earliest group. In the second row, the correction factors listed in Table 5.6 have been applied. The p0 averages here for the three groups are considerably closer, but more corrections were clearly required. Another iteration of corrections plus an additional adjustment to equalize ZDC+ and ZDC- were performed, with their results shown in the third and fourth rows, respectively.	94
5.9	ZDC- signal versus ZDC+ signal in UPC jet data. Very low energies for both ZDC+ and ZDC- are consistent with exclusive-type processes.	95

6.1	Probe jet pseudorapidity η vs. $\frac{p_{T,probe}}{p_{T,tag}}$ are shown here uncorrected (left) and corrected (right). $\frac{p_{T,probe}}{p_{T,tag}}$ is at or close to unity where $ \eta < 3$	97
6.2	Difference of azimuthal angle ϕ in the lab frame between the leading and subleading jets ($\phi_{leading} - \phi_{subleading} = \Delta\phi$) in each dijet event, before the application of the cut of $ \Delta\phi = 2$ radians. The dijets generally have a difference of π radians. The presence of a small sample that had a difference of about 0 radians necessitated the $ \Delta\phi = 2$ cut.	98
6.3	Leading and subleading jet p_T are shown here. The left plot includes no cuts on η for either the leading or the subleading jets, and the right plot applies the cuts where the leading jet has $p_T > 20$ GeV and the subleading jet has $p_T > 15$ GeV that were used in this analysis.	99
6.4	Distribution of average pseudorapidity between each dijet is shown here.	100
6.5	Two-dimensional histogram with ZDC+ signal in femtocoulombs on the x-axis and ZDC- signal in femtocoulombs on the y-axis. The tendency of an event's signal to be strong in one ZDC and weak in the other, resulting in the L-shaped plot here, is indicative of a UPC where one nuclide breaks up and the other one remains intact.	101
6.6	Two-dimensional histogram with the ratio of signal difference between ZDC+ and ZDC- to signal sum of ZDC+ and ZDC- versus dijet average η . The tendency of the signal to be strong at a ratio of -1 where $\eta < 0$ and at a ratio of 1 where $\eta > 0$ indicates that the dijets are typically produced on same end of CMS where the heavy nuclide from which they were produced breaks up.	102
6.7	Average pseudorapidity (η) and ZDC signal for cases where ZDC examination requirements were met for both ZDC+ and ZDC- (top left), ZDC+ but not ZDC- (top right), ZDC- but not ZDC+ (bottom left), and neither ZDC+ nor ZDC- (bottom right).	103

6.8	Average η and ZDC signal for the cases in Figure 6.7 where ZDC examination requirements were met for ZDC+ but not ZDC- (top row) and ZDC- but not ZDC+ (bottom row), along with their respective corresponding calculations of x_1 , x_2 , and photon Q . ZDC examination requirements being met for ZDC+ but not ZDC- resolves the x ambiguity such that x_1 is the gluon momentum fraction and x_2 is the photon momentum fraction, whereas ZDC examination requirements being met for ZDC- but not ZDC+ resolves the ambiguity between x_1 and x_2 such that x_1 is the photon momentum fraction and x_2 is the gluon momentum fraction.	104
6.9	Bjorken x and Q distributions from Figure 6.8 are shown here.	105
6.10	Average pseudorapidity, ZDC signal, x_1 and x_2 , and Q where, for each event, more than 5 GeV of energy was detected in HF- and less than 5 GeV in HF+ in the top row, and vice versa in the bottom row. The situation in the top row with stronger signals in HF- and ZDC- along with weaker signals in HF+ and ZDC+ resolves the ambiguity between x_1 and x_2 such that x_1 is the photon momentum fraction and x_2 is the gluon momentum fraction. Likewise, the situation in the bottom row with stronger signals in HF+ and ZDC+ along with weaker signals in HF- and ZDC- resolves x ambiguity such that such that x_1 is the gluon momentum fraction and x_2 is the photon momentum fraction.	106
6.11	ZDC+ and ZDC- signals where average η between the dijets is > 0 on the left and < 0 on the right.	107
6.12	Two-dimensional histogram comparing BRG and FRG for all events being analyzed. The high concentrations of events where there is high BRG and low FRG or low BRG and high FRG where $\Delta\eta > 1.2$ motivated the definitions of backward dominant and forward dominant events in this analysis.	108

6.13 Average dijet η for backward dominant events (labeled "BRG Dominant") and forward dominant events (labeled "FRG Dominant). BRG Dominant corresponds to more forward dijet pseudorapidities and FRG Dominant corresponds to more backward dijet pseudorapidities. 109

6.14 The ZDC difference/sum ratio, as a function of average η (top row) and by itself (bottom row), is shown here. Backward dominant event (BRG) are shown in the left column, and forward dominant events (FRG) are shown in the right column. BRG event tend toward a ZDC difference/sum ratio at $\eta \approx 1$, while (FRG) events tend toward to a ZDC difference/sum ratio at $\eta \approx -1$. The BRG dominant events totaled 10294, with a mean difference/sum ratio of 0.321 at a standard deviation of 0.561, and a mean average η of 0.8162 at a standard deviation of 0.5576. The FRG dominant events totaled 10316, with a mean difference/sum ratio of -0.363 at a standard deviation of 0.562, and a mean average η of -0.8196 at a standard deviation of 0.5689. 110

6.15 Leading and subleading jet vectors, with the leading jet p_T denoted by \mathbf{p}_{T1} and the subleading jet p_T denoted by \mathbf{p}_{T2} . \mathbf{Q}_T and $2\mathbf{P}_T$ are also shown, and the angle between them is denoted as Φ 111

6.16 Raw distribution of Φ between \mathbf{Q}_T and $2\mathbf{P}_T$ 112

6.17 Overall ranges of Q_T and P_T signals are shown here. Since most of the Q_T signal was between 0-25 GeV/c and most of the P_T signal was between 18-43 GeV/c, these constituted the analysis ranges for v_2 113

6.18 Two dimensional histograms of Q_T vs. P_T are shown here for raw signal (left) and mixed events (right). The raw signal again shows the principal Q_T signal between 0-25 GeV/c and the principal P_T signal between 18-43 GeV/c. 113

6.19 Raw v_2 vs. P_T (left) and Q_T (right) for BRG-dominant events and FRG-dominant events. 114

6.20	Raw v_2 vs. P_T and Q_T for BRG-dominant events and FRG-dominant events within indicated Q_T and P_T ranges.	115
6.21	Mixed events v_2 vs. P_T (left) and Q_T (right) for BRG-dominant events (red) and FRG-dominant events (blue).	116
6.22	Mixed events v_2 vs. P_T and Q_T for BRG-dominant events (red) and FRG-dominant events (blue) within indicated P_T and Q_T ranges. For v_2 vs. Q_T , many of the analysis bins have $v_2 = 0$	117
6.23	$v_{2,subtracted}$ vs. P_T (left) and Q_T (right) for BRG-dominant events (red) and FRG-dominant events (blue).	118
6.24	$v_{2,subtracted}$ vs. P_T and Q_T for BRG-dominant events (red) and FRG-dominant events (blue) within indicated P_T and Q_T ranges.	119
7.1	$v_{2,subtracted}$ results for backward dominant events, forward dominant events, and their difference is shown here.	122
7.2	Number of events for $\alpha = 0.95$, $\alpha = 0.85$, and no limits on α are shown here.	123
7.3	$\langle v_{2,subtracted} \rangle$ vs. P_T for Q_T intervals analyzed are shown here for $\alpha = 0.85$ and $\alpha = 0.95$	124
7.4	$\Delta\phi$ for $ \Delta\phi > 2.25$, $ \Delta\phi > 2$, and no limits on $ \Delta\phi $ are shown here.	125
7.5	$\langle v_{2,subtracted} \rangle$ vs. P_T for Q_T intervals analyzed are shown here for $ \Delta\phi > 2.25$ and $ \Delta\phi > 2$	126
7.6	Number of events for $ v_z < 10$, $ v_z < 20$, and no limits on $ v_z $ are shown here.	127
7.7	$\langle v_{2,subtracted} \rangle$ vs. P_T for Q_T intervals analyzed are shown here for $ v_z < 10$ and $ v_z < 20$	128
7.8	$\langle v_{2,subtracted} \rangle$ vs. P_T for Q_T intervals analyzed are shown here for where backward dominant and forward dominant dijet events are required to have less than 1000 fC in the conjugate ZDC as compared to dijet events meeting the baseline backward dominant and forward dominant criteria.	129
7.9	$\langle v_{2,subtracted} \rangle$ with the systematic error bands included are shown here.	130

8.1 $\langle v_{2,subtracted} \rangle$ vs. P_T over Q_T ranges and Q_T over P_T ranges containing the principal signal. A positive $\langle v_{2,subtracted} \rangle$ between Q_T and P_T is generally present. 133

List of Tables

2.1	Quark generations, flavors, and electric charges	5
5.1	ZDC Time Slices with Signal, shown in descending order with strongest signal listed first.	84
5.2	ZDC- Peak Ratios	87
5.3	2015 ZDC- Readout Channel Calibration Constants	88
5.4	Initial 2015 ZDC+ Readout Channel Calibration Constants	89
5.5	Final 2015 ZDC+ Readout Channel Calibration Constants	91
5.6	Average ZDC Signals for Run Number Groups in the first two plots of the top row of Figure 5.8 and Initial Correction Factors	92
5.7	Average ZDC Signals for Run Number Groups for the second two plots in the top row in Figure 5.8 and First Correction Factor Adjustments	93
5.8	Average ZDC Signals for Run Number Groups for the first two plots in the bottom row in Figure 5.8 and Second Correction Factor Adjustments	93
5.9	Average ZDC Signals for Run Number Groups for the Final Two Plots in the Bottom Row in Figure 5.8 and Final Correction Factors Applied	93
7.1	Systematic Analysis Results on $v_{2,subtracted}$	127

Chapter 1

Introduction

The purpose of the heavy ion program at Brookhaven and CERN is to understand the nature of the strong nuclear force at very high energy and density. The strong force is described by the theory of Quantum Chromo-Dynamics, or QCD. According to the theory, particles that feel the strong force, or hadrons, are made of quarks. These quarks carry a special type of charge called color. Color is the strong analog to the electric charge in electromagnetism. The strong force is mediated by the exchange of massless particles known as gluons that are analogous to photons in electromagnetic interactions. However, photons possess no charge, whereas gluons themselves do possess color; therefore, gluons can interact with other gluons. This “non-abelian” property of the gluons makes QCD calculations extremely difficult. This computational difficulty renders experimental study of the strong force all the more essential.

Heavy ion collisions are an important component of the experimental study of the strong force. One generic prediction of QCD is that, at high energy density, a plasma of quarks and gluons should be created [39]. The first compelling evidence for this state came from the STAR, PHENIX, BRAHMS, and PHOBOS experiments at the Relativistic Heavy Ion Collider (RHIC) and previously from CERN SPS experiments [6], [5], [9], [10]. This plasma seems to behave as an almost perfect fluid with a viscosity/entropy ratio close to the limit of $\frac{1}{4\pi}$ for a quantum fluid [38]. There is also evidence that the initial state of the system was not a simple superposition of proton and neutron wave functions and that the number of low momentum gluons in the nucleus was less than expected. There are three immediate questions regarding the quark-gluon plasma.

1. What are the relevant degrees of freedom in the plasma and how are colored objects (jets and

heavy quarks) affected by the plasma as they travel through it?

2. What is the ratio of viscosity to entropy of the plasma?
3. Can the initial state of the system be represented as a classical color field of gluon saturation, a “color glass condensate” [31] [39]?

In order to accurately measure the viscosity of the plasma, it is necessary to know the initial state of the system, which requires an understanding of the lead wave function. The purpose of the research presented here is to seek further understanding in the distribution of quarks and gluons inside the lead nucleus before it collides.

In experimental studies of protons, nuclei, and other hadrons, two useful quantities are Bjorken x and Q . Bjorken x is the fraction of momentum a parton (quark or gluon) possesses with respect to the hadron of which it is a component. From here on, Bjorken x will be referred to as x .

$$x = \frac{\text{momentum of parton}}{\text{momentum of hadron}}, \quad (1.1)$$

and Q is the momentum transferred to a parton when it is struck by an incoming object. Deep inelastic scattering of electrons on protons has revealed that at lower values of x , there are a larger number of gluons in the proton [44]. However, there should be a limit to this number since the size of the proton is finite. One possible result of this limit is gluon saturation, otherwise known as the “color glass condensate” [31] [39].

Figure 1.1 illustrates the ranges of x and Q that are covered in principle by the Large Hadron Collider (LHC), RHIC, and the Super Proton Synchrotron (SPS). The research presented here uses the Compact Muon Solenoid (CMS) Detector at the LHC to measure the x and Q of dijets resulting from ultra-peripheral collisions (UPCs) of ^{208}Pb nuclides. These measurements help constrain the gluon density over a wide range of x and Q . This information is useful for understanding how the initial states of the viscosity/entropy ratio fluctuate in heavy ion collisions that, in conjunction with flow measurements, would constrain viscosity/entropy in the final state.

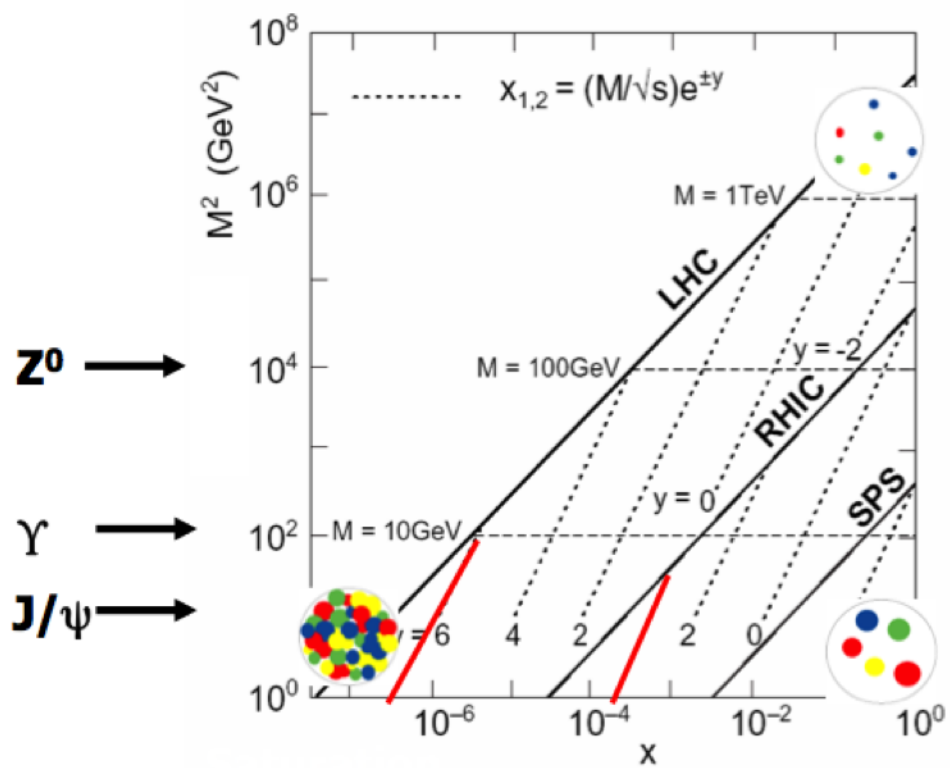


Figure 1.1: (courtesy of Michael J. Murray) Range of x and Q^2 (denoted as M^2 in the figure) for the LHC, RHIC, and SPS.

Chapter 2

Theory

This chapter lays out the theoretical background for measuring hadronic pairs of jets for ultra-peripheral collisions, or "UPC dijets". Section 2.1 summarizes what is known about quantum chromodynamics, the theory that describes the workings of the strong nuclear force. Section 2.2 provides a detailed discussion about the electromagnetic interactions between heavy ions that give rise to the photons that interact with gluons to produce UPC jets. Section 2.3 discusses how UPC jets can be used to measure the four momentum distribution of gluons in the pre-collision nuclides and concludes with the predicted UPC dijet yield from the LHC.

2.1 Quantum Chromo-Dynamics

Quantum Chromo-Dynamics (QCD) is a theoretical framework describing the workings of the strong nuclear force. According to QCD, the fundamental property of the strong nuclear force, analogous to charge in the electromagnetic force, is "color". For the electromagnetic force, there are two types of charge, positive and negative. In QCD, however, there are three sets of colors, as opposed to one set of charge in electromagnetism, for a total of six colors as opposed to two charges. They are red and anti-red, blue and anti-blue, and green and anti-green. Each color paired with its anti-color forms a colorless configuration, much like how a positive charge paired with a negative charge of equal magnitude forms a charge-neutral configuration. Colorless configurations can also be formed by a combination of red, blue, and green as well as anti-red, anti-blue, and anti-green.

In QCD, nucleons and other hadrons are modeled as being made up of subatomic particles

known as partons. These partons include quarks and gluons. Quarks are massive fermionic particles (spin $\hbar/2$, where \hbar is Planck's constant divided by 2π) that possess fractional electric charge (with respect to the electron charge, $1.60218 \times 10^{-19} C$ ([30], XVI)) and interact via the strong nuclear force. That is, they have color. There are twelve types of quarks, or rather three generations of quarks, each generation consisting of two "flavors", plus their anti-matter counterparts. They are listed in Table 2.1.

Table 2.1: Quark generations, flavors, and electric charges

Generation	Flavor	Electric Charge
first	d (down)	-1/3
	u (up)	+2/3
second	s (strange)	-1/3
	c (charm)	+2/3
third	b (bottom)	-1/3
	t (top)	+2/3
anti-first	\bar{d} (anti-down)	+1/3
	\bar{u} (anti-up)	-2/3
anti-second	\bar{s} (anti-strange)	+1/3
	\bar{c} (anti-charm)	-2/3
anti-third	\bar{b} (anti-bottom)	+1/3
	\bar{t} (anti-top)	-2/3

Gluons are massless, bosonic (integer spin \hbar) particles that mediate the strong interaction, analogous to the photon in electromagnetism. At the most basic level, QCD models the strong force as an exchange of gluons between quarks. However, unlike electromagnetism where the photons that mediate the interaction between charged particles are themselves uncharged, the gluons themselves possess color and thus interact with other gluons. Specifically, each gluon carries one color and one anti-color. This also means that a specific flavor of quark changes color upon interacting strongly with another quark; hence, whereas the electric charge of an electromagnetically-interacting particle is fixed, the color of a quark or gluon changes with every strong interaction.

Generally, hadrons are composed of 3 quarks (baryons), 3 anti-quarks (anti-baryons), or quark-anti-quark pairs (mesons). Baryonic arrangements involve three quarks that form a colorless com-

bination (red, blue, and green or anti-red, anti-blue, and anti-green), for example protons and neutrons. The quarks that form hadronic bound states, as discussed above, are known as valence quarks. Valence quarks are not the only quarks in hadrons, however. There are also sea quarks, quark-antiquark pairs, in the hadron that exist virtually. Mesonic arrangements involve a quark-antiquark pair that form a colorless combination (red and anti-red, etc.). Evidence has also recently emerged suggesting the existence of exotic mesons containing two quarks and two anti-quarks, as well as exotic baryons containing four quarks and one anti-quark [8].

Like the electromagnetic force, there is a potential energy between two particles interacting via the strong nuclear force. The potential energy of the electromagnetic force between two electric charges is well understood, and has the form

$$V(r) = \frac{1}{4\pi\epsilon_0} \frac{q^2}{r}, \quad (2.1)$$

where V is the potential energy, ϵ_0 is the permittivity of free space (see Section 2.2 for exact value), q is electric charge, and r is the distance between the two charges in question. If q is equal to the electron charge, then $q^2 = \hbar c \alpha$, and the potential is then ([30], 162)

$$V(r) = \frac{1}{4\pi\epsilon_0} \frac{\hbar c \alpha_e}{r}. \quad (2.2)$$

α_e is the fine structure constant, also known as the electromagnetic coupling constant, and has a value of $\frac{1}{137.036}$. The electric charge of a particle is not necessarily constant, however. The formation of virtual pairs of charged particles and their corresponding anti-particles result in virtual electric dipoles that partially screen electric charges and reduce their fields. This is known as vacuum polarization, where the vacuum has a dielectric effect ([30], 69). Beyond the Compton wavelength ($\lambda_c = h/mc$, where h is Planck's constant and m is the mass of the charged particle), this effect is negligible, but within the Compton wavelength this means that the magnitude of the electric charge will increase up to a certain point.

For the strong nuclear force, the potential energy between two colored partons is not well

understood. It is known to have the approximate form ([30], 173)

$$V(r) = \frac{f\hbar c\alpha_s}{r} + F(r). \quad (2.3)$$

Here, there are some additional factors compared to the electromagnetic potential between two charges. $F(r)$ is a term that apparently increases with r without limit. Its exact form is not known. $F(r) \approx r^2$, $F(r) \approx r$, and $F(r) \approx \ln(r)$ all apparently fit existing data reasonably well. They each do not differ very much over the range of distances for which sensitive probes have been available thus far. f is an additional color factor that depends on the specific color state and flavor configuration¹. α_s is the strong nuclear counterpart to the electromagnetic coupling constant. However, in QCD, the coupling "constant" is not constant at all and is therefore referred to as the running coupling constant, and is said to possess the property known as asymptotic freedom. It has the form ([44], [30], [40])

$$\alpha_s = \frac{12\pi}{(11n_c - 2n_f)\ln(Q^2/\Lambda^2)}. \quad (2.4)$$

The term n_c is the number of color-anti-color pairs and is therefore equal to 3, while n_f is the number of flavor-anti flavor pairs. The factor $11n_c - 2n_f$ accounts for an opposing vacuum polarization effect between the quarks and the gluons. Like electrically charged particles, there is a vacuum polarization effect for strongly colored partons. For quarks, the effect is similar to that of electrically-charged particles where the color magnitude increases at shorter distances. However, for gluons, the vacuum polarization effect is the opposite, and the color magnitude decreases at shorter distances. n_f depends on the energy threshold and how it compares to the quark flavor masses. For example, if Q is greater than the energy of the rest mass of the charm quark but less than that of the bottom quark, $n_f = 4$. Since there are six flavor-anti-flavor pairs, n_f has a maximum potential value of 6. Therefore, $|11n_c| > |2n_f|$ under all circumstances, so the gluon polarization effect dominates the quark polarization effect, and the color magnitude decreases overall at shorter distances. Λ is a momentum cutoff scale, which is something of a boundary between the

¹See [30], Chapter 8, Sections 3 and 4 for more details.

partonic and hadronic scales. Developing a firm understanding of the strong nuclear force and how it behaves over short and long distances is a fundamental objective of further research in nuclear physics.

This increasing strength of the strong nuclear force between partons as they get further apart means that all partons are effectively confined in bound states to other partons in color-neutral configurations. This of course includes the force between quarks in baryons and mesons, which increases if the quarks are further apart. If the energy driving two quarks apart is sufficiently high, at a separation of around 10^{-15} m new quark-anti-quark pairs are formed, thus increasing the number of hadrons. A cascading of this process results in the production of hadronic jets, with each jet moving along the direction of the original quark/anti-quark, as in Figure 2.1.

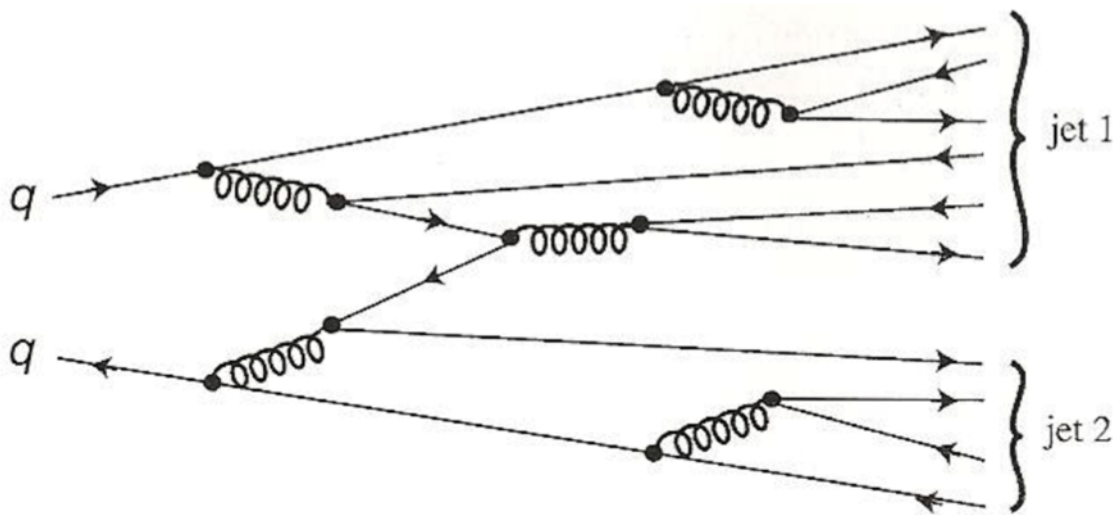


Figure 2.1: ([30], 276) Two separate quarks fragment into jets. Note the link between them that ensures color neutralization.

The relative four-momentum contributions of the valence quarks, sea quarks, and gluons to the total four-momentum of the hadron can be modeled by parton distribution functions. The four-momentum of a particle i \vec{p}_i is

$$\vec{p}_i \cdot \vec{p}_i = p_i^2 = E_i^2/c^2 - \mathbf{p}_i \cdot \mathbf{p}_i \quad (2.5)$$

where E is energy, c is the speed of light, and \mathbf{p} is the spatial momentum vector. From here on, four-momentum will be referred to as momentum. In general, the function $f(x)$ can be used to represent the parton probability density and $xf(x)$ to represent the parton momentum distribution. More specifically, $g(x)$ can be used to represent the probability density for the gluons, and $q(x)$ can be used to represent the probability density for all of the quarks. For quarks, $q(x)$ includes the contribution of both valence quarks and sea quarks,

$$q(x) = q^v(x) + q^s(x), \quad (2.6)$$

where $q^v(x)$ is the probability density for the valence quarks of a particular flavor, and $q^s(x)$ is the probability density for the sea quarks of that flavor. The total momentum of all of the partons in a hadron must add up to the momentum of the hadron, that is:

$$1 = \int_0^1 x[q(x) + g(x)]dx, \quad (2.7)$$

The momentum distribution of partons in the hadron can be studied via deep inelastic scattering with electrons or muons, as shown in Figure 2.2. The parton is struck by the virtual photon radiated from an electron, and the parton has a fraction x of the total momentum of the hadron. Consider the following situation, as illustrated in Figure 2.3, where two incoming particles with initial momenta p_1 and p_2 scatter, resulting in two outgoing particles with final momenta p_3 and p_4 . The momenta of the particles are related by the following relativistic invariants:

$$S = (\vec{p}_1 + \vec{p}_2)^2 = (\vec{p}_3 + \vec{p}_4)^2 \quad (2.8)$$

$$T = (\vec{p}_1 - \vec{p}_3)^2 = (\vec{p}_2 - \vec{p}_4)^2 \quad (2.9)$$

$$U = (\vec{p}_1 - \vec{p}_4)^2 = (\vec{p}_2 - \vec{p}_3)^2 \quad (2.10)$$

\sqrt{S} is the total momentum that is available in the collision. The square of the momentum transfer

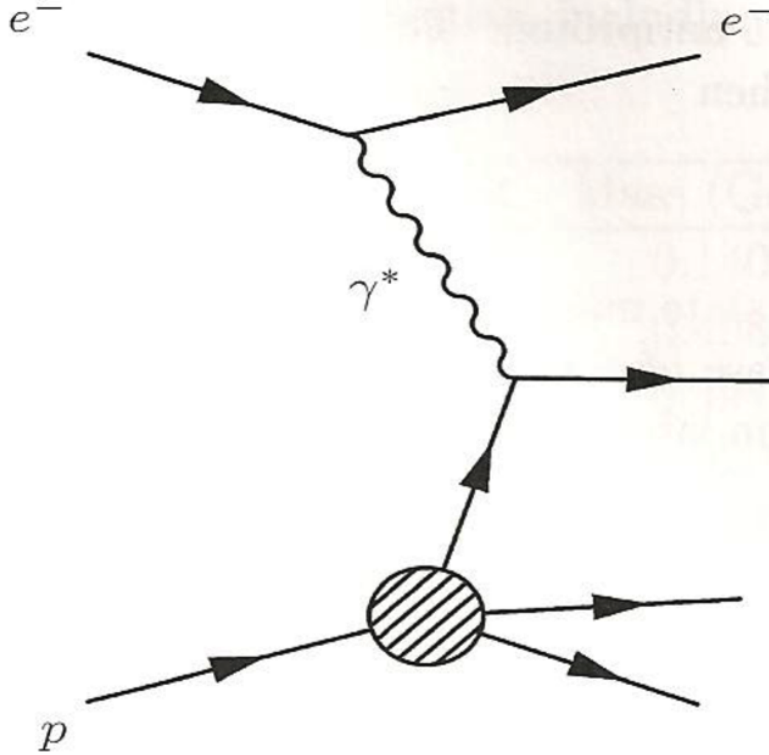


Figure 2.2: ([44], 66) Deep inelastic scattering: an electron scatters off of a proton. The electron emits a virtual photon, which transfers momentum between the electron and a charged parton within the proton.

from the electron to the parton via the virtual photon is given by T . In terms of the above variables:

$$x = T/S = Q^2/S, \quad (2.11)$$

where Q is the vector magnitude of \vec{Q} , the momentum difference between \vec{p}_1 and \vec{p}_3 . In the case of deep inelastic scattering, \vec{Q} is the momentum transferred between the electron and the parton it scatters off of. Figure 2.4 shows fits to the momentum distributions for valence quarks, sea quarks, and gluons at a $Q^2 = 10 \text{ (GeV}/c)^2$, as measured by the H1 and Zeus experiments at the HERA electron proton collider. The number of gluons increases as x decreases. However, Equation 2.7 imposes a bound on the integral of the quark and gluon densities. Therefore, at some point, this

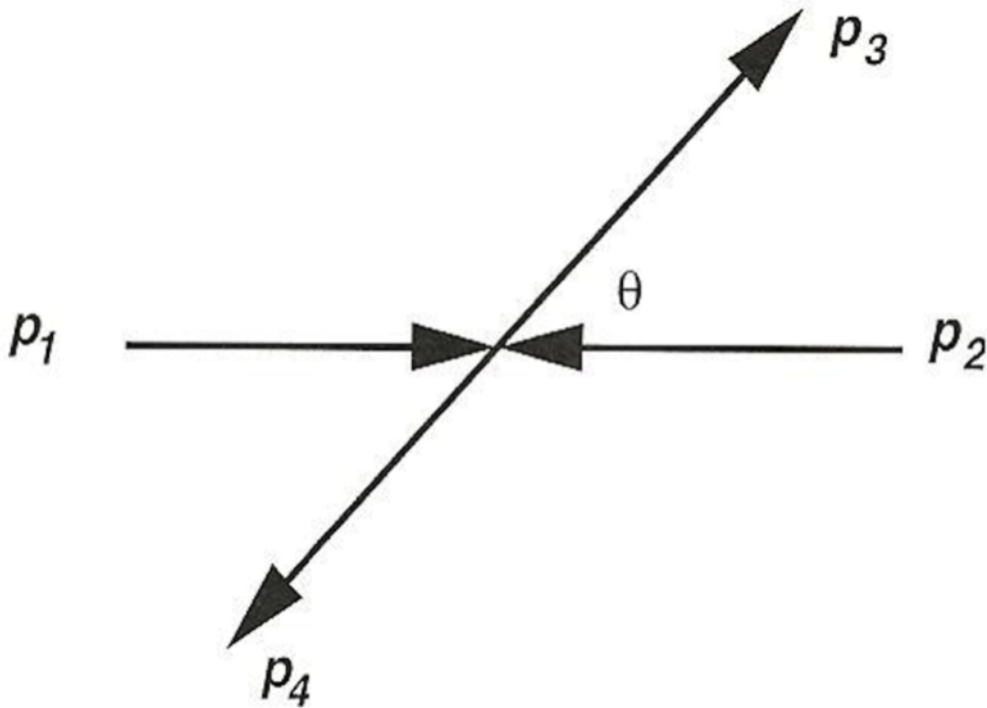


Figure 2.3: ([44], 14) Branches of a $2 \rightarrow 2$ scattering event.

trend of increasing numbers of gluons at lower x must reverse.

At both the LHC and RHIC, heavy ions are being collided at energies that result in the formation of what appears to be a decoupled state of strongly-interacting matter, a quark-gluon plasma. In a quark-gluon plasma, quarks are no longer bound in hadronic forms, and the medium behaves as a dense liquid of unbound but strongly-interacting quarks and gluons. The formation of the quark-gluon plasma from hadronic matter is a phase transition that occurs at a temperature corresponding to about 170 MeV [44]. This formation of the quark-gluon plasma duplicates conditions that are hypothesized to have existed in the universe shortly after the Big Bang, when temperatures were above this threshold. As stated in Chapter 1, experimental measurements indicate that the quark-gluon plasma is an almost perfect fluid, exhibiting little if any viscosity. Chiral symmetry is also thought to be restored at or near this phase transition. Chiral symmetry, or parity invariance, deals with "handedness" of a particle. The breaking of this symmetry, that is, the non-conservation

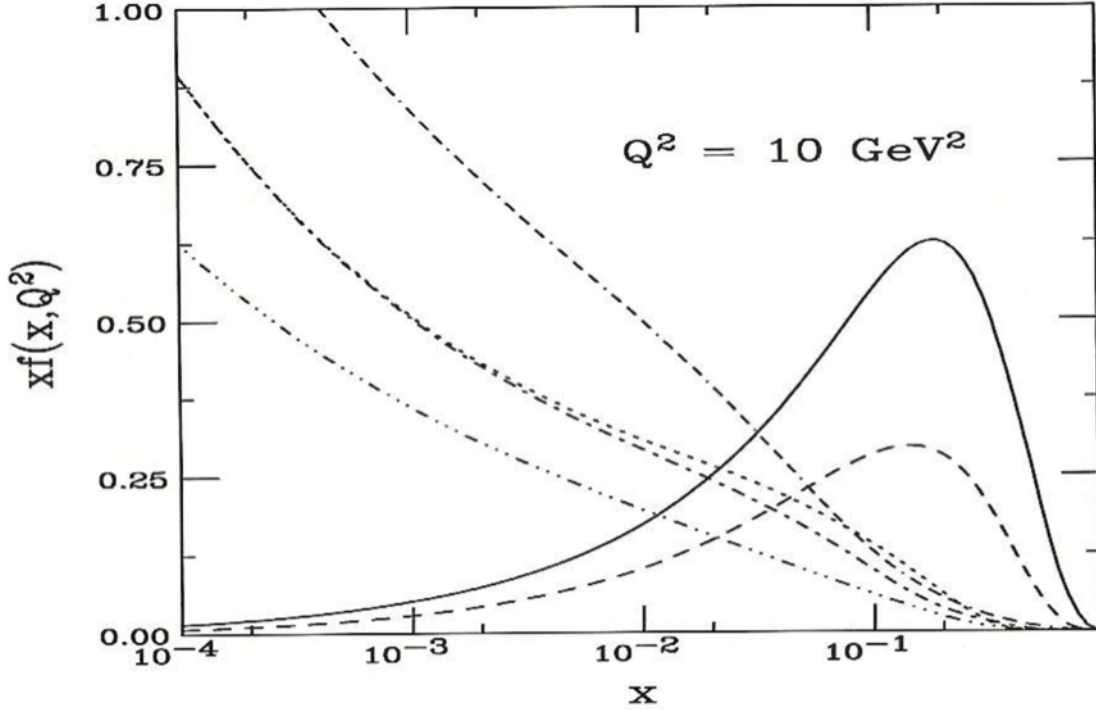


Figure 2.4: ([44], 84) Proton parton distribution functions as a function of x at $Q^2 = 10 \text{ GeV}^2/c^2$. The parton distribution functions are fits to data, and are represented as follows: solid = valence u quark, dashed = valence d quark, dot-dashed = sea u and \bar{u} quarks, dotted = sea d and \bar{d} quarks, dot-dot-dot-dashed = sea s and \bar{s} quarks, and dash-dash-dash-dotted = gluons. The gluon distribution has been divided by 10. Note how rapidly the gluon density increases as x decreases.

of parity, results in the different masses of quark flavors. After its formation, the quark-gluon plasma will quickly change phase again back to hadronic matter by freezing out into a large number of hadrons. Figure 2.5 shows a diagram of the known and hypothesized QCD states of strong nuclear matter.

As mentioned in Chapter 1, one immediate question regarding the quark-gluon plasma is whether the initial state of the strong nuclear-interacting matter prior to the formation of the quark-gluon plasma at high energies can be represented as a color glass condensate. Since the increasing number of gluons at lower values of x must reverse at some point, the gluons in the nuclides must reach a state of saturation at some low value of x . The color glass condensate is a theoretical model of this state of saturation [27]. In the color glass condensate, the sources of color appear to be randomly distributed from event to event but "frozen" on the natural time scales of strong

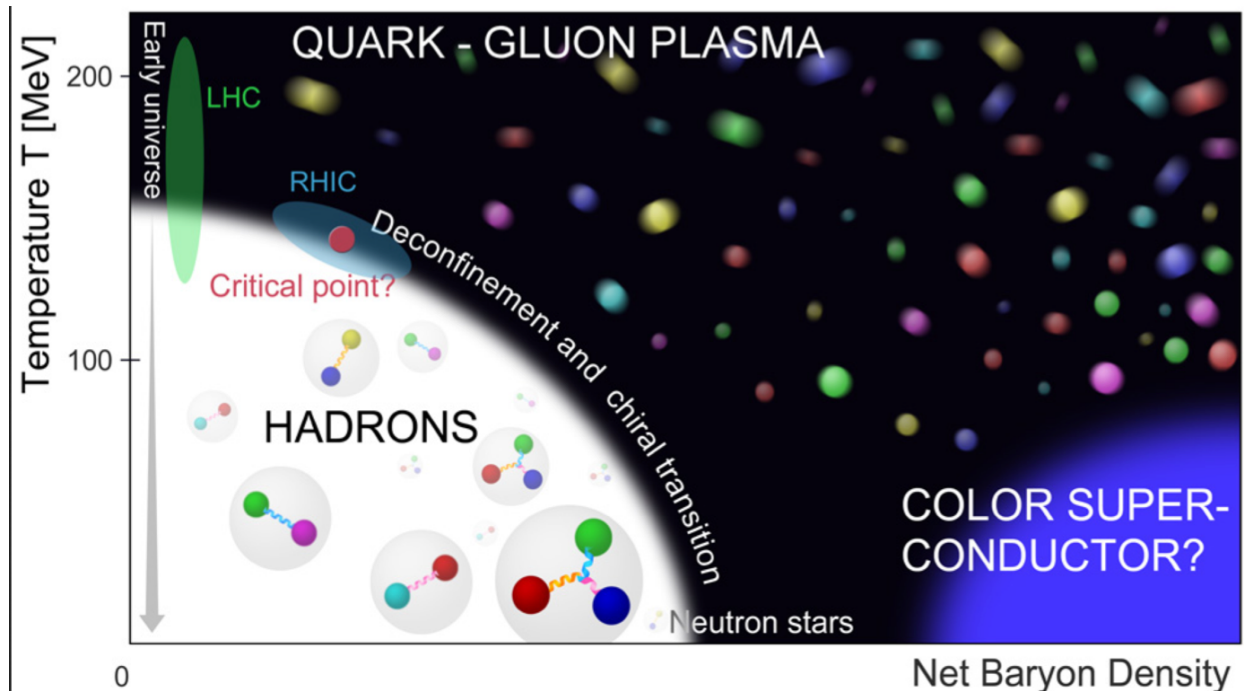


Figure 2.5: ([36], 84) Phase diagram of known and QCD-hypothesized states of strong nuclear-interacting matter is shown here. Experiments at RHIC and the LHC take place in high temperature but low density regions that resemble conditions that existed throughout the universe shortly after the Big Bang. Color superconductor refers to extremely dense states of strong nuclear-interacting matter that form spin-0 pairs and behave like bosons.

nuclear interactions due to relativistic time dilation. Meanwhile, there are dynamic fields that emanate from and couple to the color sources that are analogous to the electric and magnetic fields described by classical electromagnetic theory. The seemingly frozen state of the color sources that change slowly with time is the origin of the term "color glass," as a glass behaves like a solid on short time scales but like a liquid on long time scales. The term "condensate" refers to the high gluon density.

The optimal way to probe the initial state of the nuclides prior to the collision is via deep inelastic scattering with electrons. However, at LHC and RHIC energies, deep inelastic scattering to probe the initial state is not presently an option. There are proposals to build electron-ion colliders, including the possible conversion of RHIC into an electron-ion collider, and such initiatives are ongoing at present. At the same time, ultra-peripheral collisions can be used to study the gluon distribution [21] [22] [20]. These results serve as a probe of the initial conditions in the nuclides

prior to collision and can be used to search for the color glass condensate. In an ultra-peripheral heavy ion collision, the impact parameter of the collision is greater than the sum of the radii of the two nuclei. However, these nuclei still interact electromagnetically and exchange photons. Quantum field fluctuations can result in photons transforming into quark or gluon pairs, and those gluon pairs then go on to interact with the gluons in the nucleus, producing vector mesons, open heavy flavor mesons, or jets. These measurements could then be used to reveal properties of the initial state such as the gluon distribution, which could indicate the presence of the color glass condensate.

2.2 Electromagnetic Interactions in Ultra-Peripheral Heavy Ion Collisions

This section describes in detail how the relativistic transformation of the electromagnetic fields of heavy ions gives rise to the photon flux that can produce UPC dijets. At high energies, the fields transform in such a way that they closely resemble a ring of photons that surround each heavy ion nuclide. The electric fields specifically resemble those shown in Figure 2.6.

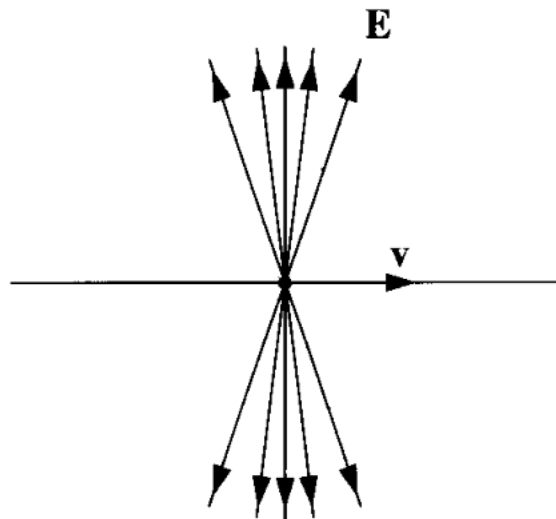


Figure 2.6: ([29], 440) The electric field lines of a point charge moving at a relativistic speed are shown here.

2.2.1 Electromagnetic Fields of Relativistic Heavy Ions

In special relativity, the Lorentz Transformations relate coordinates in four-dimensional space-time between two inertial, i.e. non-accelerating, reference frames. Specifically, the coordinate relationships between a reference frame S and a reference frame \bar{S} moving in the $+\hat{x}$ direction at a speed v relative to S , shown in Figure 2.7, are as follows ([29], 496). Going from S to \bar{S} , they are

$$\begin{aligned}\bar{t} &= \gamma\left(t - \frac{vx}{c^2}\right) \\ \bar{x} &= \gamma(x - vt) \\ \bar{y} &= y \\ \bar{z} &= z\end{aligned}\tag{2.12}$$

where c is the speed of light ($3 * 10^8$ m/s) ([29]) and $\gamma = \frac{1}{\sqrt{(1-v^2/c^2)}}$. Going from \bar{S} to S , they are

$$\begin{aligned}t &= \gamma\left(\bar{t} + \frac{v\bar{x}}{c^2}\right) \\ x &= \gamma(\bar{x} - v\bar{t}) \\ y &= \bar{y} \\ z &= \bar{z}\end{aligned}\tag{2.13}$$

To understand the electromagnetic interaction between two nuclei in ultra-peripheral heavy ion collisions, it is necessary to understand how the electromagnetic fields of the nuclei relativistically transform ([29], 525-532).

Consider the case of an electric field between the plates of a large parallel-plate capacitor that carries surface charge densities on each plate of $\pm\sigma_o$. In frame S_o , the capacitor is at rest, as shown in Figure 2.8a. The electric field between the plates is

$$\mathbf{E}_o = \frac{\sigma_o}{\epsilon_o}\hat{\mathbf{y}},\tag{2.14}$$

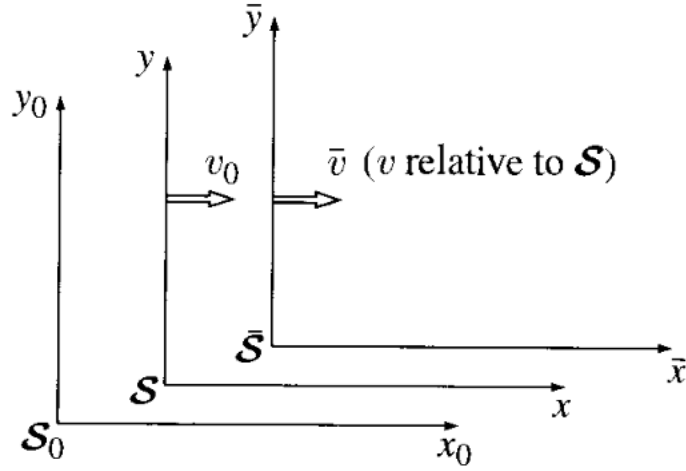


Figure 2.7: ([29], 529) Coordinate axes for three inertial reference frames, S_o , S , and \bar{S} , and their speeds with respect to each other.

where ϵ_o is the permittivity of free space ($8.85 \times 10^{-12} \text{ C}^2/\text{Nm}^2$ [29]). In frame S , which is moving to the right at speed v_o , the capacitor is observed to move left as shown in Figure 2.8b. Here, the electric field is

$$\mathbf{E} = \frac{\sigma}{\epsilon_o} \hat{y}. \quad (2.15)$$

Charge is invariant. All observers in any inertial reference frame will agree on the quantity of charge. However, observers in frame S will measure a different length in the \hat{x} -dimension than will be seen in S_o . Therefore, the charge density σ will increase over σ_o such that

$$\sigma = \gamma_o \sigma_o \quad (2.16)$$

where $\gamma_o = \frac{1}{\sqrt{1-v_o^2/c^2}}$. The components of the electric field perpendicular to the capacitor plates are therefore

$$\begin{aligned} E_{,perp} &= \frac{\gamma_o \sigma_o}{\epsilon_o} \\ &= \gamma_o E_{o,perp} . \end{aligned} \quad (2.17)$$

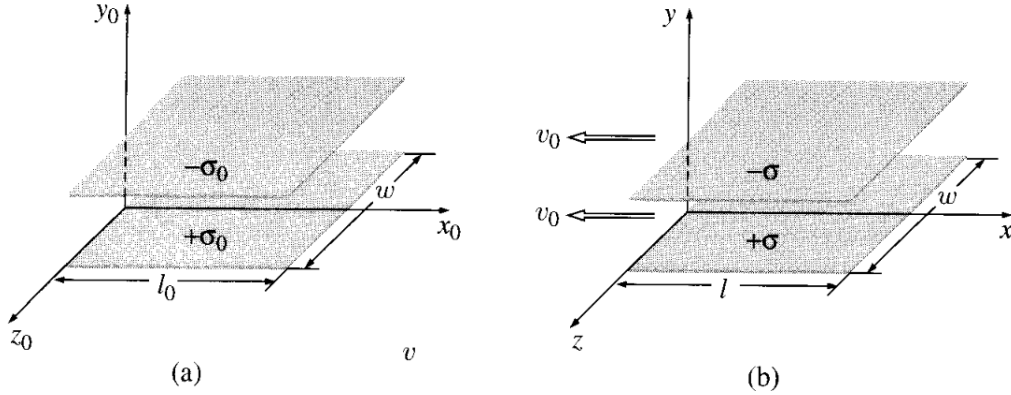


Figure 2.8: ([29], 526) Parallel plate capacitor shown in frame S_o (a) and in frame S (b).

The electric field for parallel components can be found by considering the capacitor aligned with the yz plane, as shown in Figure 2.9. This time it is plate separation distance d that is length-contracted in frame S , whereas length l and width w are the same in both S and S_o . Therefore, the charge density σ_o is the same in both frames as well, and the parallel components of the electric fields in frames S and S_o are

$$E_{,par} = E_{o,par}. \quad (2.18)$$

In frame S , there is also a magnetic field due to the surface currents

$$\mathbf{K}_{\pm} = \mp \sigma v_o \hat{\mathbf{x}}. \quad (2.19)$$

By the right-hand rule, this magnetic field points in the $-\hat{z}$ direction. By Ampere's Law, its magnitude is

$$B_z = -\mu_o \sigma v_o, \quad (2.20)$$

where μ_o is the permeability of free space ($4\pi * 10^{-7} N/A^2$) [29]. In the third inertial reference frame \bar{S} that is traveling to the right with speed v relative to S and \bar{v} relative to S_o , as shown in Figure 2.5, the fields are then

$$\bar{E}_y = \frac{\bar{\sigma}}{\epsilon_o} \quad (2.21)$$

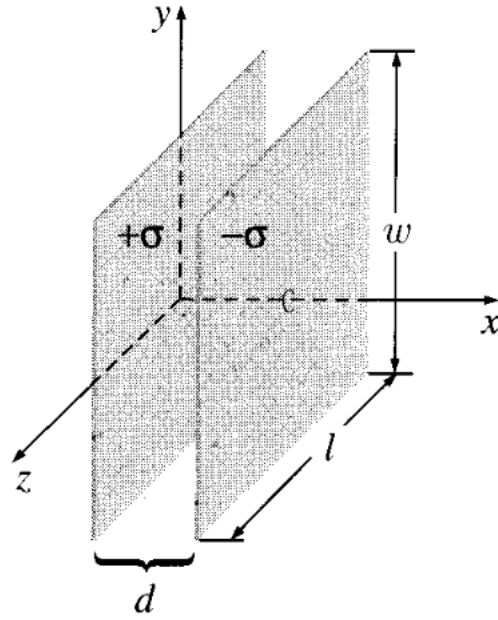


Figure 2.9: ([29], 527) Parallel plate capacitor aligned with the yz plane.

$$\bar{B}_z = -\mu_0 \bar{\sigma} \bar{v}, \quad (2.22)$$

keeping note that $E_y = \frac{\sigma}{\epsilon_0}$ by the argument in the previous paragraph.

By Einstein's velocity addition rule ([29], 498), \bar{v} , the speed of \bar{S} with respect to S_o , is

$$\bar{v} = \frac{(v + v_o)}{(1 + vv_o/c^2)} \quad (2.23)$$

where

$$\bar{\gamma} = \frac{1}{\sqrt{(1 - \bar{v}^2/c^2)}} \quad (2.24)$$

and

$$\bar{\sigma} = \bar{\gamma} \sigma_o. \quad (2.25)$$

Expressing the components of \bar{E} and \bar{B} in terms of E and B ,

$$\begin{aligned}
 \bar{E}_y &= \frac{\bar{\sigma}}{\epsilon_o} \\
 &= \frac{\tilde{\gamma}\sigma_o}{\epsilon_o} \\
 &= \frac{\tilde{\gamma}}{\epsilon_o} \left(\frac{\sigma}{\gamma_o} \right) \\
 &= \left(\frac{\tilde{\gamma}}{\gamma_o} \right) \frac{\sigma}{\epsilon_o},
 \end{aligned} \tag{2.26}$$

and

$$\begin{aligned}
 \bar{B}_z &= -\mu_o \bar{\sigma} \bar{v} \\
 &= -\mu_o \tilde{\gamma} \sigma_o \bar{v} \\
 &= -\mu_o \tilde{\gamma} \left(\frac{\sigma}{\gamma_o} \right) \bar{v} \\
 &= -\left(\frac{\tilde{\gamma}}{\gamma_o} \right) \mu_o \bar{v}.
 \end{aligned} \tag{2.27}$$

Now, after doing some algebra,

$$\frac{\tilde{\gamma}}{\gamma_o} = \gamma \left(1 + \frac{v v_o}{c^2} \right). \tag{2.28}$$

Inserting this into the above equations for \bar{E}_y and \bar{B}_z ,

$$\begin{aligned}
 \bar{E}_y &= \left(\frac{\tilde{\gamma}}{\gamma_o} \right) \left(\frac{\sigma}{\epsilon_o} \right) \\
 &= \gamma \left(1 + \frac{v v_o}{c^2} \right) \left(\frac{\sigma}{\epsilon_o} \right) \\
 &= \gamma \left(\frac{\sigma}{\epsilon_o} + \frac{v v_o \sigma}{\epsilon_o c^2} \right) \\
 &= \gamma \left(E_y - \frac{v B_z}{\mu_o \epsilon_o c^2} \right),
 \end{aligned} \tag{2.29}$$

and

$$\begin{aligned}
\bar{B}_y &= -\left(\frac{\bar{\gamma}}{\gamma_o}\right)\mu_o\sigma\bar{v} \\
&= -\frac{\gamma(1+vv_o/c^2)\mu_o\sigma(v+v_o)}{(1+vv_o/c^2)} \\
&= -\gamma\mu_o\sigma(v+v_o) \\
&= -\gamma(\mu_o\epsilon_o E_y v - B_z) \\
&= \gamma(B_z - \mu_o\epsilon_o v E_y) .
\end{aligned} \tag{2.30}$$

Since $\mu_o\epsilon_o = \frac{1}{c^2}$,

$$\bar{E}_y = \gamma(E_y - vB_z) , \tag{2.31}$$

and

$$\bar{B}_z = \gamma\left(B_z - \frac{vE_y}{c^2}\right) . \tag{2.32}$$

In order to find \bar{E}_z and \bar{B}_y in terms of E_z and B_y , the capacitor is aligned parallel to the xy plane instead of the xz plane, as shown in Figure 2.10. Therefore, in frame S ,

$$E_z = \frac{\sigma}{\epsilon_o} , \tag{2.33}$$

and

$$B_y = \mu_o\sigma v_o . \tag{2.34}$$

Again, the right-hand rule is used to determine the direction and therefore the sign of B_y . The rest of the process is the same as in the last paragraph, where E_z replaces E_y and $-B_y$ replaces B_z :

$$\bar{E}_z = \gamma(E_z + vB_y) , \tag{2.35}$$

and

$$\bar{B}_y = \gamma\left(B_y + \frac{vE_z}{c^2}\right) . \tag{2.36}$$

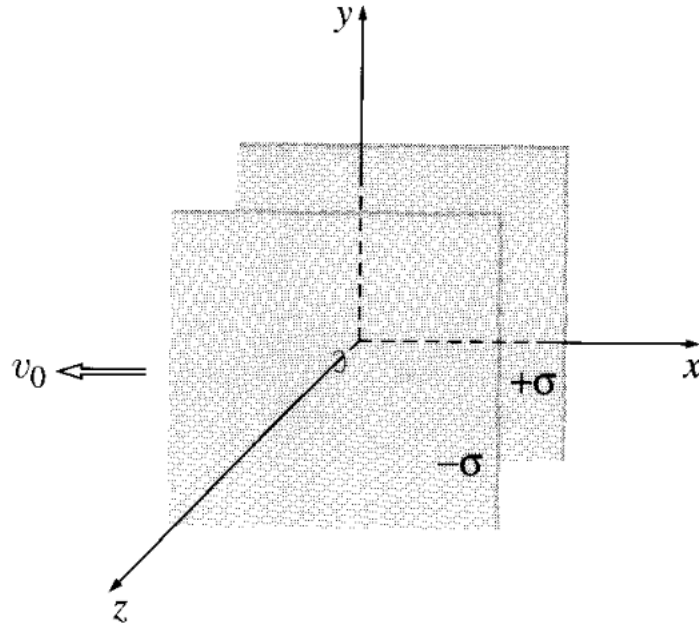


Figure 2.10: ([29], 530) Parallel plate capacitor aligned with the xy plane.

As far as the x components are concerned,

$$\vec{E}_x = E_x \quad (2.37)$$

for the reason, previously detailed, that the field does not depend upon the distance between the capacitor plates when the capacitor is aligned with the yz plane. However, this being the case, there is no associated magnetic field in this situation. To find out how B_x transforms, it is necessary to consider another arrangement: a long solenoid, as shown in Figure 2.11. By Ampere's Law ([29], 227-228), the magnetic field inside the solenoid is:

$$B_x = \mu_0 n I , \quad (2.38)$$

with I being the solenoid current and n being the number of turns per unit length. In \bar{S} , there is

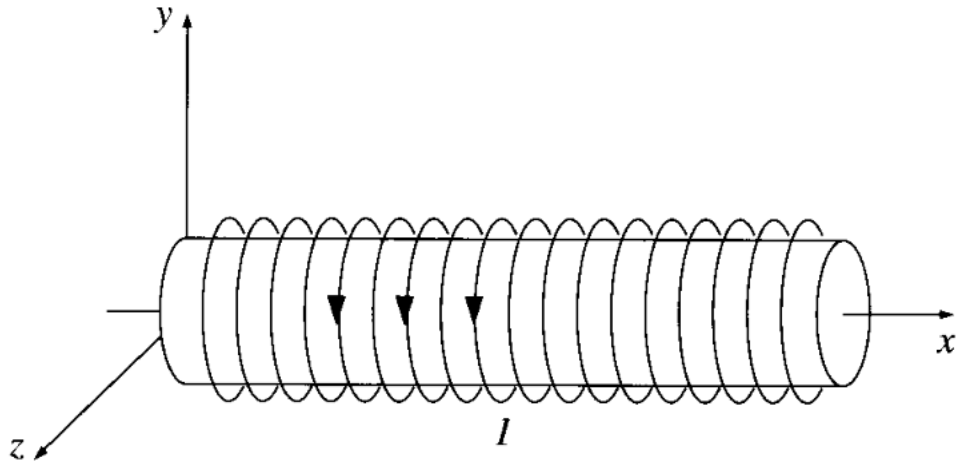


Figure 2.11: ([29], 531) A long solenoid.

length contraction and time dilation, so n gets larger and I gets smaller:

$$\bar{n} = \gamma n, \bar{I} = \frac{I}{\gamma}. \quad (2.39)$$

So,

$$\bar{B}_x = \frac{\mu_o \gamma n I}{\gamma} = \mu_o n I = B_x; \quad (2.40)$$

as with the component of the electric field parallel to the direction of motion, the component of the magnetic field parallel to the motion is also unchanged.

The complete list of transformation rules for the components of the electric and magnetic fields

is therefore:

$$\begin{aligned}
 \bar{E}_x &= E_x \\
 \bar{E}_y &= \gamma(E_y - vB_z) \\
 \bar{E}_z &= \gamma(E_z + vB_y) \\
 \bar{B}_x &= B_x \\
 \bar{B}_y &= \gamma\left(B_y + \frac{vE_z}{c^2}\right) \\
 \bar{B}_z &= \gamma\left(B_z - \frac{vE_y}{c^2}\right).
 \end{aligned} \tag{2.41}$$

Note that if $\mathbf{B} = 0$ in S ,

$$\begin{aligned}
 \bar{\mathbf{B}} &= \frac{\gamma v(E_z \hat{\mathbf{y}} - E_y \hat{\mathbf{z}})}{c^2} \\
 &= \frac{v(\bar{E}_z \hat{\mathbf{y}} - \bar{E}_y \hat{\mathbf{z}})}{c^2};
 \end{aligned} \tag{2.42}$$

or, more generally, being that $\mathbf{v} = v\hat{\mathbf{x}}$,

$$\bar{\mathbf{B}} = -\frac{(\mathbf{v} \times \bar{\mathbf{E}})}{c^2}. \tag{2.43}$$

Likewise, if $\mathbf{E} = 0$ in S ,

$$\begin{aligned}
 \bar{\mathbf{E}} &= -\gamma v(B_z \hat{\mathbf{y}} - B_y \hat{\mathbf{z}}) \\
 &= -v(\bar{B}_z \hat{\mathbf{y}} - \bar{B}_y \hat{\mathbf{z}});
 \end{aligned} \tag{2.44}$$

or again, more generally,

$$\bar{\mathbf{E}} = (\mathbf{v} \times \bar{\mathbf{B}}). \tag{2.45}$$

These transformation rules can be used to transform the fields of a point charge. A heavy nuclide can be approximated as a point charge. If a point charge q is at rest at the origin of S_0 , the

components of the electric field \mathbf{E}_o in S (moving at velocity \mathbf{v}_o relative to S_o) are

$$\begin{aligned} E_{x_o} &= \frac{qx_o}{4\pi\epsilon_o(x_o^2 + y_o^2 + z_o^2)^{3/2}}, \\ E_{y_o} &= \frac{qy_o}{4\pi\epsilon_o(x_o^2 + y_o^2 + z_o^2)^{3/2}}, \\ E_{z_o} &= \frac{qz_o}{4\pi\epsilon_o(x_o^2 + y_o^2 + z_o^2)^{3/2}}. \end{aligned} \quad (2.46)$$

From Equations 2.17 and 2.18, these become

$$\begin{aligned} E_x &= E_{x_o} = \frac{qx_o}{4\pi\epsilon_o(x_o^2 + y_o^2 + z_o^2)^{3/2}}, \\ E_y &= \gamma_o E_{y_o} = \frac{\gamma_o qy_o}{4\pi\epsilon_o(x_o^2 + y_o^2 + z_o^2)^{3/2}}, \\ E_z &= \gamma_o E_{z_o} = \frac{\gamma_o qz_o}{4\pi\epsilon_o(x_o^2 + y_o^2 + z_o^2)^{3/2}}. \end{aligned} \quad (2.47)$$

With the geometry of a point charge at some arbitrary point P , as shown in Figure 2.12, the elec-

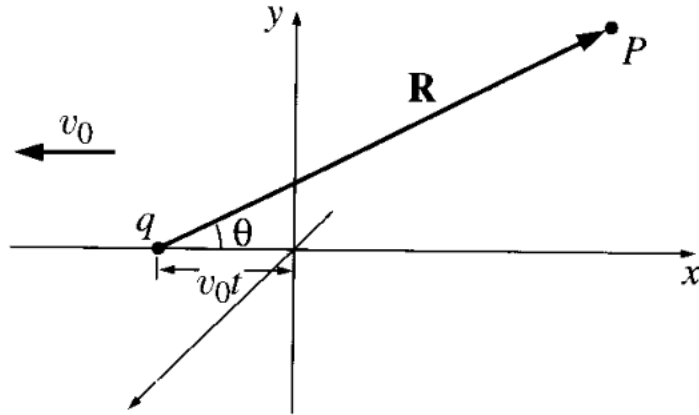


Figure 2.12: ([29], 528) Diagram of a point charge in motion with respect to an arbitrary point P .

tric field \mathbf{E} can be expressed in terms of the vector \mathbf{R} from the charge in S . Using the Lorentz

transformations (Equation 2.13),

$$\begin{aligned}
 x_o &= \gamma_o(x + v_o t) = \gamma_o R_x , \\
 y_o &= y = R_y , \\
 z_o &= z = R_z .
 \end{aligned}
 \tag{2.48}$$

The electric field is then

$$\mathbf{E} = \frac{\gamma_o q \mathbf{R}}{4\pi\epsilon_o(\gamma_o^2 R^2 \cos^2\theta + R^2 \sin^2\theta)^{3/2}} .
 \tag{2.49}$$

After some algebra, this simplifies to

$$\mathbf{E} = \frac{q(1 - v_o^2/c^2)\hat{\mathbf{R}}}{4\pi\epsilon_o R^2 [1 - (v_o^2/c^2)\sin^2\theta]^{3/2}} .
 \tag{2.50}$$

As for the magnetic field, note that the magnetic field is zero everywhere in the point charge's rest frame S_o . Therefore, Equation 2.43 can be used to find the magnetic field in S :

$$\begin{aligned}
 \mathbf{B} &= -\frac{\mathbf{v}_o \times \mathbf{E}}{c^2} \\
 &= -\mu_o \epsilon_o (\mathbf{v}_o \times \mathbf{E}) \\
 &= -\frac{\mu_o \epsilon_o q (1 - v_o^2/c^2)}{4\pi\epsilon_o R^2 (1 - (v_o^2/c^2)\sin^2\theta)^{3/2}} (\mathbf{v}_o \times \mathbf{R}) ,
 \end{aligned}
 \tag{2.51}$$

simplifying to

$$\mathbf{B} = \frac{\mu_o q v_o (1 - v_o^2/c^2) \sin\theta}{4\pi R^2 (1 - (v_o^2/c^2)\sin^2\theta)^{3/2}} \hat{\boldsymbol{\phi}} ,
 \tag{2.52}$$

where, by the right-hand rule, $\hat{\boldsymbol{\phi}}$ points counterclockwise when facing the oncoming charge. The field lines of the electric and magnetic fields of the point charge in S are shown in Figures 2.13 and 2.14, respectively (note that \mathbf{v}_o is simply denoted as " \mathbf{v} " here). The electric field lines of a fast moving point charge are flattened out like a pancake in the direction perpendicular to the velocity of the charge due to the factor of $\sin^2\theta$ in the denominator ([29], 439). The magnetic field lines, meanwhile, circle around the charge and increase in magnitude closer to the charge.

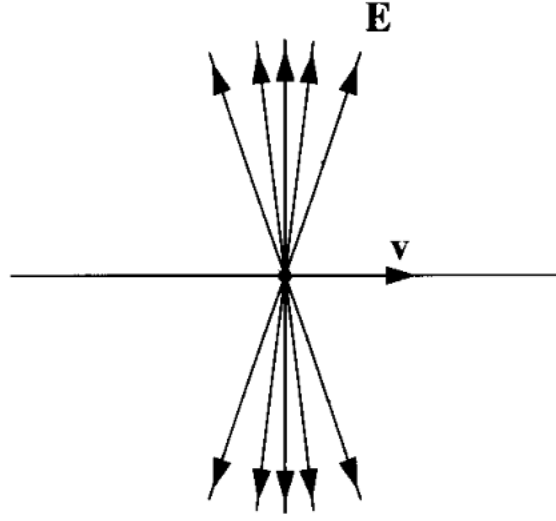


Figure 2.13: ([29], 440) The electric field lines of a point charge moving at a relativistic speed flatten out like a pancake perpendicular to the charge velocity.

The power per unit area, that is, the energy per unit time per unit area, transported by these electromagnetic fields is known as the Poynting vector ([29], 347, 533):

$$\begin{aligned}
 \mathbf{S}_P &= \frac{\mathbf{E} \times \mathbf{B}}{\mu_o} \\
 &= -\frac{\mu_o \epsilon_o}{\mu_o} \mathbf{E} \times (\mathbf{v}_o \times \mathbf{E}) \text{ (by Equation 2.51)} \\
 &= -\epsilon_o [\mathbf{v}_o (\mathbf{E} \cdot \mathbf{E}) - \mathbf{E} (\mathbf{E} \cdot \mathbf{v}_o)] \\
 &= -\mathbf{v}_o \epsilon_o |\mathbf{E}|^2 .
 \end{aligned} \tag{2.53}$$

For the point charge in S , the Poynting vector is

$$\begin{aligned}
 \mathbf{S}_P &= \frac{\mu_o v_o (q(1 - v_o^2/c^2))^2 \sin \theta}{\mu_o \epsilon_o (4\pi R^2 (1 - (v_o^2/c^2) \sin^2 \theta)^{3/2})^2} \hat{\mathbf{R}} \times \hat{\boldsymbol{\phi}} \\
 &= \frac{v_o q^2 (1 - v_o^2/c^2)^2 \sin \theta}{16\pi^2 \epsilon_o R^4 (1 - (v_o^2/c^2) \sin^2 \theta)^3} \hat{\mathbf{v}}_o
 \end{aligned} \tag{2.54}$$

since, by the right-hand rule, $\hat{\mathbf{R}} \times \hat{\boldsymbol{\phi}} = \mathbf{v}_o$, the direction of motion of the point charge. When v_o approaches c , at a distance away from the trajectory of the point charge, the electromagnetic fields

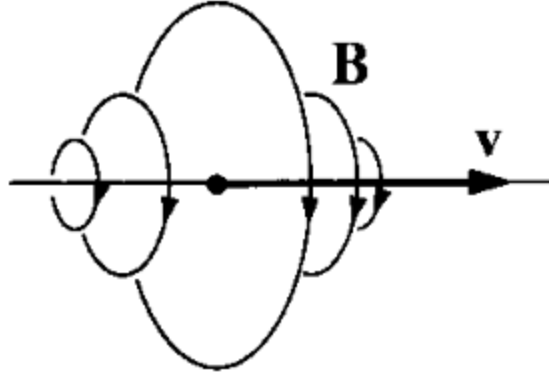


Figure 2.14: ([29], 440) The magnetic field lines of a point charge circle the direction of charge velocity, with increasing magnitude closer to the charge.

of the point charge just described resemble those of propagating electromagnetic waves ([12], [26], [45], [46]). Therefore, these electromagnetic fields can be modeled as a flux of photons around the fast-moving charge; and another charged particle, such as another heavy nuclide, that passes through the electromagnetic field of this fast-moving charge at this distance will pass through this flux of photons.

2.2.2 Photon Flux of Relativistic Heavy Ions

For ultra-peripheral heavy ion collisions, the energy of these photons can be estimated from the energy-time uncertainty principle:

$$\Delta t \Delta E \geq \frac{\hbar}{2}, \quad (2.55)$$

where Δt is the time of the collision and ΔE is the range of photon energies. The time of the collision in S is

$$\Delta t = \frac{2R_{nuc}}{\gamma_0 v_0}, \quad (2.56)$$

since S is time-dilated with respect to S_o , and R_{nuc} is the nuclear radius. Therefore,

$$\begin{aligned} \frac{2R_{nuc}\Delta E}{\gamma_o v_o} &\geq \frac{\hbar}{2} \\ \Rightarrow \Delta E &\geq \frac{\gamma_o v_o \hbar}{4R_{nuc}} . \end{aligned} \quad (2.57)$$

The energies of the photons surrounding the nuclide will have energies close to these values. Note that the energy of a photon is, generally, $E = \hbar\omega$, where ω is the angular frequency of the electromagnetic waves surrounding the nuclide.

The flux of photons surrounding the nuclide, N , is estimated using the quasi-classical Wiezsäcker-Williams Method of Virtual Quanta ([12], [26], [45], [46], [28], [35] 724-729, [44] 98-100). The Wiezsäcker-Williams Method is summarized as follows. The Fourier Transform of \mathbf{E} is

$$\mathbf{E}(\omega) = \frac{1}{2\pi} \int_{-\infty}^{+\infty} \mathbf{E}(t)e^{i\omega t} dt , \quad (2.58)$$

with the Fourier Transform of $\mathbf{E}(t)$ to $\mathbf{E}(\omega)$, \mathbf{S}_P is equal to the frequency spectrum, that is, the energy per unit time per unit frequency interval $\frac{dI}{d\omega}$ ([35], 726):

$$|\mathbf{S}_P| = v_o \epsilon_o |\mathbf{E}(\omega)|^2 = \frac{dI}{d\omega} . \quad (2.59)$$

For a relativistic charged particle passing an area in S , the radiation from the charge can be modeled as two pulses, P_1 and P_2 , as shown in Figure 2.15. The frequency spectra for these pulses are

$$\begin{aligned} \frac{dI_1}{d\omega}(\omega, b) &= \frac{1}{\pi^2} \left(\frac{c}{v_o}\right)^2 \frac{1}{b^2} \left(\frac{\omega b}{\gamma_o v_o}\right)^2 K_1^2\left(\frac{\omega b}{\gamma_o v_o}\right) = v_o \epsilon_o |E_2(\omega)|^2, \text{ and} \\ \frac{dI_2}{d\omega}(\omega, b) &= \frac{1}{\pi^2} \left(\frac{c}{v_o}\right)^2 \frac{1}{b^2} \frac{1}{\gamma_o^2} \left(\frac{\omega b}{\gamma_o v_o}\right)^2 K_0^2\left(\frac{\omega b}{\gamma_o v_o}\right) = v_o \epsilon_o |E_1(\omega)|^2, \end{aligned} \quad (2.60)$$

where b is the impact parameter (the distance of the charged particle to the center of the area of concern in S at the charged particle's closest point of approach), K_0 and K_1 are modified Bessel functions ([44], 98), and E_1 and E_2 are the magnitudes of the components of $\mathbf{E}(\omega)$ as shown in

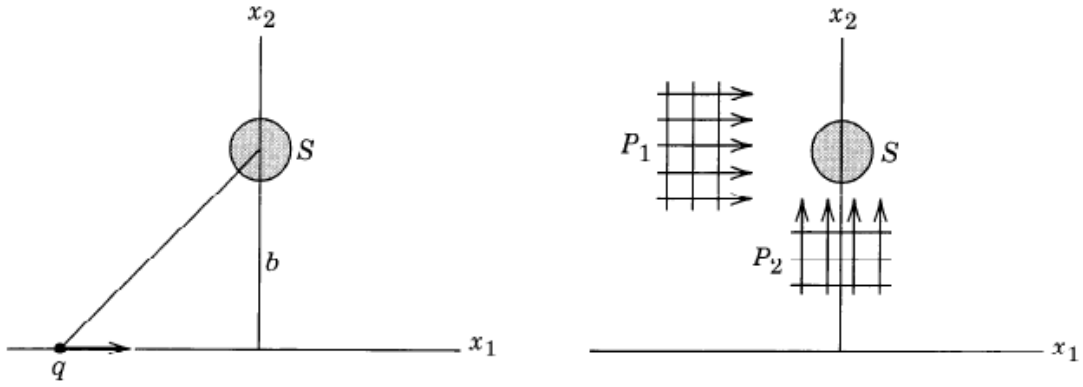


Figure 2.15: ([35], 726) The radiation of a point charge passing in proximity to an area of space in frame S can be modeled as two pulses P_1 and P_2 .

Figure 2.13. The total frequency spectrum is yielded by:

$$\frac{dI}{d\omega}(\omega) = 2\pi \int_{b_{min}}^{\infty} \left[\frac{dI_1}{d\omega}(\omega, b) + \frac{dI_2}{d\omega}(\omega, b) \right] b db \quad (2.61)$$

resulting in

$$\frac{dI}{d\omega}(\omega) = \frac{2}{\pi} \frac{q^2}{c} \left(\frac{c}{v_o} \right)^2 \left\{ x K_0(x) K_1(x) - \frac{v_o^2}{2c^2} x^2 [K_1^2(x) - K_0^2(x)] \right\}, \quad (2.62)$$

where $x = \frac{\omega b_{min}}{\gamma_o v_o}$.

The quasi-classical estimate of the photon flux is yielded by the relation

$$\frac{dI}{d\omega}(\omega) d\omega = \hbar \omega N(\hbar \omega) d(\hbar \omega), \quad (2.63)$$

where $N(\hbar \omega)$ is the number spectrum of virtual quanta, i.e., the photon flux per unit energy interval.

Therefore,

$$N(\hbar \omega) = \frac{1}{\hbar^2 \omega} \frac{dI}{d\omega}(\omega). \quad (2.64)$$

It should be noted that P_2 is very small compared to P_1 in the relativistic limit, hence these electromagnetic fields approximating a ring of photons around a highly relativistic heavy ion.

2.3 Hadronic Jets From Ultra-Peripheral Heavy Ion Collisions

The photons from this flux can interact with gluons by means of photon-gluon fusion ([43] [44] 96-98 [12] [37]) in which quantum field fluctuations allow for the two particles to interact via the strong nuclear force. A quark-antiquark pair is the result of this interaction, which then cascades into two jets. In this process, the photon is defined as having momentum fraction x_1 , and the gluon is defined as having momentum fraction x_2 . In the LHC experiment being detailed here, the photon and the gluon collide at an angle of 180° , or π radians. Therefore, the total sum of the momentum vectors of the dijets that result will be entirely along the directional axis of the original path along which the photon and gluon were moving before fusion, i.e., "along the beam line." In other words, the total momentum of the system will have an entirely longitudinal direction, parallel or anti-parallel to the original path of the photon and gluon. This means that any transverse momentum (p_T) the jets have, that is, any momentum the jets have that is perpendicular to the beamline, will sum to zero. A schematic diagram of this process is shown in Figure 2.16, and a Feynman diagram is shown in Figure 2.17.

In order to find x_1 and x_2 , and subsequently Q , for the gluons that combine with the photons to produce dijets, the relationship between x_1 and x_2 and quantities that are directly measurable needs to be clear. Particles of concern, in this case photons and gluons, have momenta with the general components

$$\vec{p} = (E, p_T, p_z) \quad (2.65)$$

where E is the energy as defined in Equation 2.5, and p_z is the longitudinal momentum of particle, i.e., the momentum along the beamline. The vector sum of p_T and p_z is the particle's spatial momentum vector. Since the photons and the gluons interact, it is necessary to use the momenta of the partons in the hadrons. Therefore, parton momentum is the product of x and the hadron

γ-Pb interaction

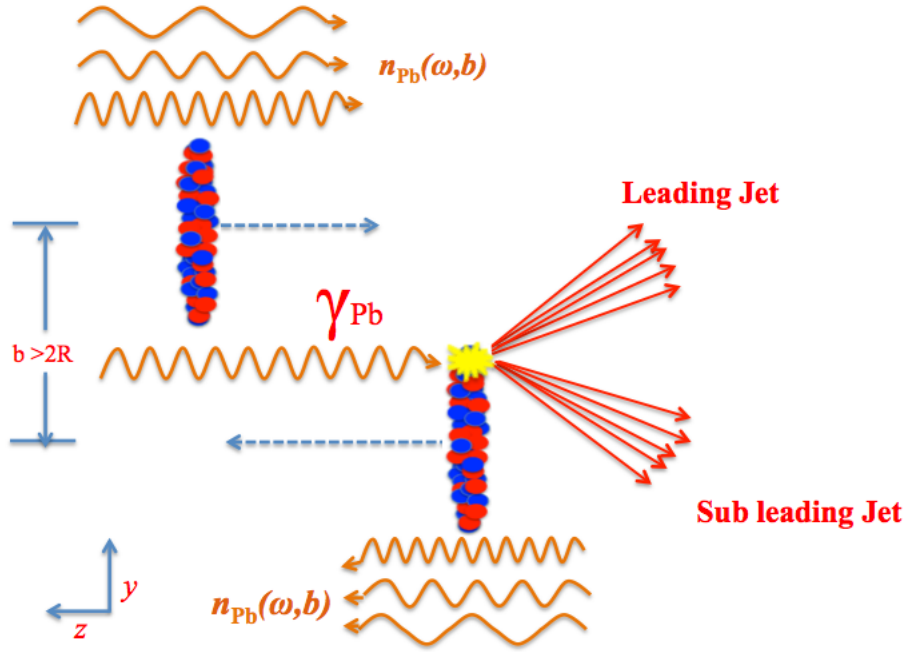


Figure 2.16: (Courtesy of Ayman Al-bataineh) Conceptual diagram of an ultra-peripheral collision that produces dijets. In this diagram, $n_{pb} = \frac{dI}{d\omega}$ (as defined in Section 2.2) and R is the nuclear radius.

momentum:

$$p'_1 = x_1 p_1, \text{ and} \tag{2.66}$$

$$p'_2 = x_2 p_2,$$

where p'_1 and p'_2 are the parton momenta and p_1 and p_2 are the hadron momenta. Both photons and gluons are massless, so the components of p'_1 and p'_2 are

$$\vec{p}'_1 = \left(\frac{E'_1}{c}, p'_{T1}, p'_{z1} \right) = \left(\frac{x_1 \sqrt{S}}{2}, 0, \frac{x_1 \sqrt{S}}{2} \right), \text{ and} \tag{2.67}$$

$$\vec{p}'_2 = \left(\frac{E'_2}{c}, p'_{T2}, p'_{z2} \right) = \left(\frac{x_2 \sqrt{S}}{2}, 0, -\frac{x_2 \sqrt{S}}{2} \right),$$

where S was defined in Equation 2.8. For the specific interaction between the photon and gluon, a

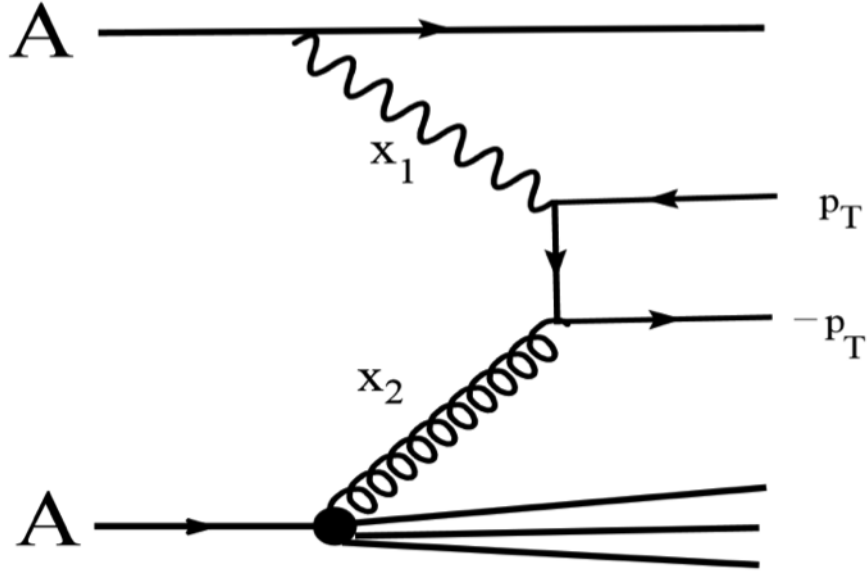


Figure 2.17: ([43], 1) Feynman diagram of an inclusive UPC resulting in dijets. A photon with momentum fraction x_1 from one nuclide A is absorbed by the second identical nuclide A, where quantum field fluctuations cause it to interact with a gluon of momentum fraction x_2 , and dijets with equal in magnitude and opposite in direction p_T result.

relativistic invariant s can be defined according to Equation 2.8:

$$s = (\vec{p}'_1 + \vec{p}'_2)^2 = (\vec{p}'_3 + \vec{p}'_4)^2 \quad (2.68)$$

where \vec{p}'_3 and \vec{p}'_4 are the momenta of the respective dijets. Expanding this out for the former case,

$$s = p_1'^2 + 2\vec{p}'_1 \cdot \vec{p}'_2 + p_2'^2. \quad (2.69)$$

Since the photons and gluons are massless,

$$\frac{E'_1}{c} = |\mathbf{p}'_1| \Rightarrow p_1'^2 = \frac{E_1'^2}{c^2} - |\mathbf{p}'_1|^2 = 0, \quad (2.70)$$

and, likewise, $p_2'^2 = 0$. Therefore,

$$\begin{aligned}
s &= 2p_1' \cdot p_2' \\
&= 2\left(\frac{x_1\sqrt{S}}{2}, 0, \frac{x_1\sqrt{S}}{2}\right) \cdot \left(\frac{x_2\sqrt{S}}{2}, 0, -\frac{x_2\sqrt{S}}{2}\right) \\
&= 2\left(\frac{x_1x_2S}{4} - -\frac{x_1x_2S}{4}\right) \\
&= 2\left(\frac{2x_1x_2S}{4}\right) \\
&= x_1x_2S.
\end{aligned} \tag{2.71}$$

At this point, it is necessary to define a quantity known as rapidity, y :

$$y = \frac{1}{2} \ln \frac{E + p_z c}{E - p_z c}. \tag{2.72}$$

y can also be expressed in terms of the particle's speed if the direction of the particle's velocity is wholly along the beamline:

$$y = \frac{1}{2} \ln \frac{1 + \beta}{1 - \beta} \tag{2.73}$$

since $\beta = \frac{p_z c}{E}$ in this case ². Now,

$$\sinh y = \frac{e^y - e^{-y}}{2}, \quad \cosh y = \frac{e^y + e^{-y}}{2}. \tag{2.74}$$

Therefore,

$$\begin{aligned}
e^y &= \left(\frac{E + p_z c}{E - p_z c}\right)^{\frac{1}{2}} = \sqrt{\frac{E + p_z c}{E - p_z c}}, \\
e^{-y} &= \left(\frac{E + p_z c}{E - p_z c}\right)^{-\frac{1}{2}} = \sqrt{\frac{E - p_z c}{E + p_z c}}
\end{aligned} \tag{2.75}$$

²In general, $\beta = \frac{|p|c}{E}$

$$\begin{aligned}
\Rightarrow e^y + e^{-y} &= \sqrt{\frac{E + p_z c}{E - p_z c}} + \sqrt{\frac{E - p_z c}{E + p_z c}} \\
&= \sqrt{\frac{(E + p_z c)(E + p_z c)}{(E - p_z c)(E + p_z c)}} + \sqrt{\frac{(E - p_z c)(E - p_z c)}{(E + p_z c)(E - p_z c)}} \\
&= \frac{(E + p_z c)}{\sqrt{E^2 - p_z^2 c^2}} + \frac{(E - p_z c)}{\sqrt{E^2 - p_z^2 c^2}} \\
&= \frac{2E}{\sqrt{E^2 - p_z^2 c^2}},
\end{aligned} \tag{2.76}$$

and

$$\cosh y = \frac{e^y + e^{-y}}{2} = \frac{E}{\sqrt{E^2 - p_z^2 c^2}}. \tag{2.77}$$

Similarly,

$$\sinh y = \frac{e^y - e^{-y}}{2} = \frac{p_z c}{\sqrt{E^2 - p_z^2 c^2}}. \tag{2.78}$$

It is convenient to restate $\sinh y$ and $\cosh y$ in terms of the quantity called transverse mass, m_T .

A particle's relativistic invariant is

$$m^2 c^4 = E^2 - p_z^2 c^2 - p_T^2 c^2. \tag{2.79}$$

Adding the p_T term to both sides,

$$m^2 c^4 + p_T^2 c^2 = E^2 - p_z^2 c^2 = m_T^2 c^4. \tag{2.80}$$

Therefore,

$$m_T c^2 = \sqrt{E^2 - p_z^2 c^2}, \tag{2.81}$$

and $\sinh y$ and $\cosh y$ become

$$\begin{aligned}
\sinh y &= \frac{p_z c}{m_T c^2}, \\
\cosh y &= \frac{E}{m_T c^2}.
\end{aligned} \tag{2.82}$$

Using these terms, the jet momenta p'_3 and p'_4 have the components

$$\begin{aligned} p'_3 &= \left(\frac{E'_3}{c}, p'_{T3}, p'_{z3} \right) = (m'_{T3} \cosh y'_3, p'_{T3}, m'_{T3} \sinh y'_3) \\ p'_4 &= \left(\frac{E'_4}{c}, p'_{T4}, p'_{z4} \right) = (m'_{T4} \cosh y'_4, p'_{T4}, m'_{T4} \sinh y'_4). \end{aligned} \quad (2.83)$$

Now,

$$p'_1 + p'_2 = p'_3 + p'_4. \quad (2.84)$$

Filling in the components of p'_1 , p'_2 , p'_3 , p'_4 in Equation 2.84, which are given in Equations 2.67 and 2.83, yields the following results:

$$\frac{x_1 \sqrt{S}}{2} + \frac{x_2 \sqrt{S}}{2} = m'_{T3} \cosh y'_3 + m'_{T4} \cosh y'_4, \quad (2.85)$$

$$0 + 0 = p'_{T3} + p'_{T4} = 0 \quad (2.86)$$

since $p'_{T3} = -p'_{T4}$, and

$$\frac{x_1 \sqrt{S}}{2} - \frac{x_2 \sqrt{S}}{2} = m'_{T3} \sinh y'_3 + m'_{T4} \sinh y'_4. \quad (2.87)$$

The objective here is to solve for x_1 and x_2 . To do this, first add Equations 2.85 and 2.87:

$$\frac{2x_1 \sqrt{S}}{2} = m'_{T3} (\cosh y'_3 + \sinh y'_3) + m'_{T4} (\cosh y'_4 + \sinh y'_4). \quad (2.88)$$

Next, subtract Equation 2.87 from Equation 2.85:

$$\frac{2x_2 \sqrt{S}}{2} = m'_{T3} (\cosh y'_3 - \sinh y'_3) + m'_{T4} (\cosh y'_4 - \sinh y'_4). \quad (2.89)$$

At this point, the hyperbolic trigonometric identities of Equation 2.74 are again called upon:

$$\begin{aligned} x_1 \sqrt{S} &= m'_{T3} \left(\frac{e^{y'_3} + e^{-y'_3} + e^{y'_3} - e^{-y'_3}}{2} \right) + m'_{T4} \left(\frac{e^{y'_4} + e^{-y'_4} + e^{y'_4} - e^{-y'_4}}{2} \right) \\ &= m'_{T3} e^{y'_3} + m'_{T4} e^{y'_4}, \end{aligned} \quad (2.90)$$

$$\Rightarrow x_1 = \frac{m'_{T3} e^{y'_3} + m'_{T4} e^{y'_4}}{\sqrt{S}} \quad (2.91)$$

and similarly,

$$x_2 = \frac{m'_{T3} e^{-y'_3} + m'_{T4} e^{-y'_4}}{\sqrt{S}}. \quad (2.92)$$

From Equation 2.80,

$$m_T = \sqrt{m^2 + \frac{p_T^2}{c^2}}. \quad (2.93)$$

Therefore,

$$x_1 = \frac{e^{y'_3} \sqrt{m_3^2 + \frac{p_{T3}^2}{c^2}} + e^{y'_4} \sqrt{m_4^2 + \frac{p_{T4}^2}{c^2}}}{\sqrt{S}}, \quad (2.94)$$

$$x_2 = \frac{e^{-y'_3} \sqrt{m_3^2 + \frac{p_{T3}^2}{c^2}} + e^{-y'_4} \sqrt{m_4^2 + \frac{p_{T4}^2}{c^2}}}{\sqrt{S}}. \quad (2.95)$$

Bjorken x_1 and x_2 are now entirely in terms of quantities which can be experimentally determined. Note, however, that while x_1 has been arbitrarily defined as the momentum fraction of the photon and x_2 has been arbitrarily defined as the momentum fraction of the gluon, the reality is that the two are experimentally ambiguous. Bjorken x_1 can be the momentum fraction of the gluon and Bjorken x_2 can be the momentum fraction of the photon. It is therefore necessary to be able to resolve this experimental ambiguity by having a device that can measure the nuclear breakup. The nuclide containing the gluon that is struck by the photon is likely to at least partially break up, and evidence of this breakup can be detected in the form of neutrons and other particles. Measurements of these particles on one side of the collision but not the other side will yield the original photon direction [7], and thereby resolve the ambiguity between the photon x and the gluon x . With this information, Q can then be found using Equation 2.11 [7]. The x and Q distributions measured

from this analysis are discussed in Chapter 6, Section 6.2.

The hypothesized cross section for photon-gluon fusion that results in UPC jets, $\sigma_{\gamma g \rightarrow q\bar{q}}$ is [12]

$$\sigma_{\gamma g \rightarrow q\bar{q}}(W_{\gamma g}) = \frac{\pi e_q^2 \alpha_e \alpha_s(Q^2) \hbar^2 c^2}{W_{\gamma g}} \left[(3 - \beta^4) \ln\left(\frac{1 + \beta}{1 - \beta}\right) - 2\beta(2 - \beta^2) \right], \quad (2.96)$$

where e_q is the quark electric charge, $W_{\gamma g}$ is the photon-gluon center of momentum energy, $\beta = \left(1 - \frac{4m_q^2 c^4}{W_{\gamma g}^2}\right)$, m_q being the mass of the quark or antiquark, and α_s is evaluated at $Q^2 = m_q^2 c^2 + p_T^2$. A plot of the predicted UPC dijet production rate in the LHC is shown in Figure 2.18. The data used

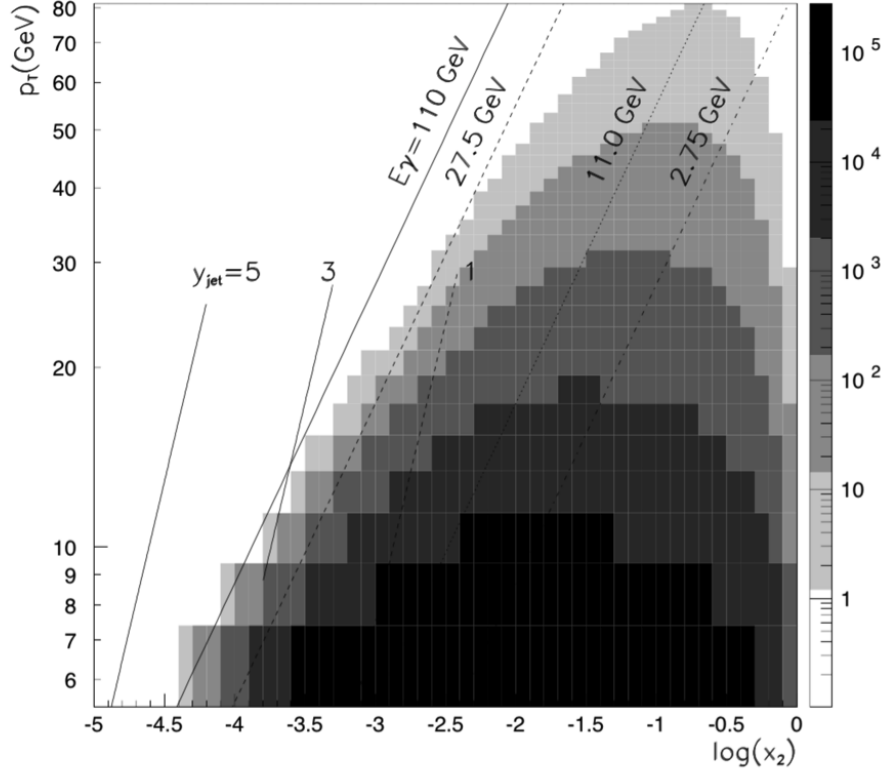


Figure 2.18: ([43], 2) Predicted UPC dijet production rate for a Pb-Pb run of 10^6 seconds at luminosity $0.42 \times 10^{27} \text{ cm}^{-2} \text{ s}^{-1}$ and $\sqrt{S_{NN}} = 5.5 \text{ TeV}$. Rates are in counts per bin of $\pm 1 \text{ GeV}$ and $\pm 0.25x_2$.

to produce the predicted dijet production rate in Figure 2.18 were also used to plot the predicted number of dijets produced strictly as a function of p_T . This is shown in Figure 2.19.

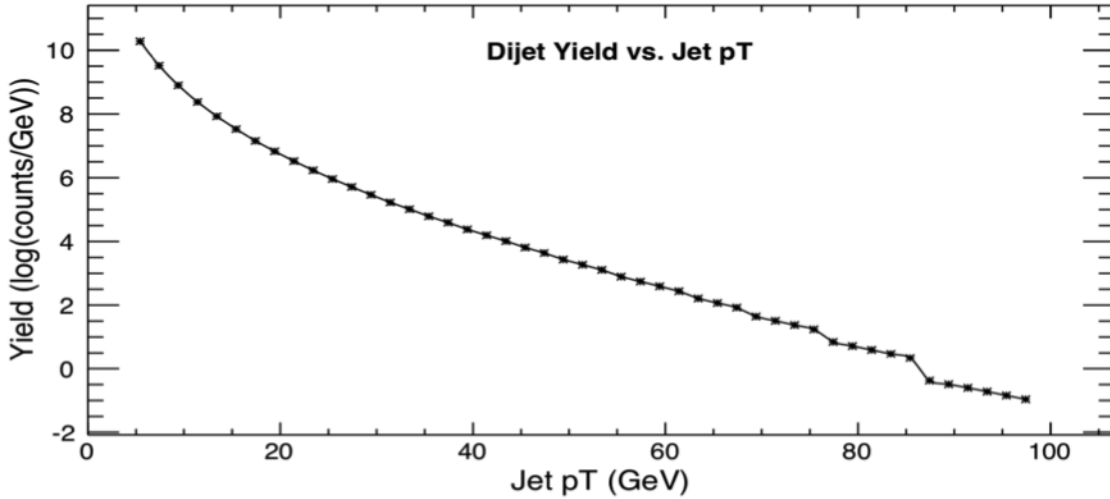


Figure 2.19: (Prediction specifics provided courtesy of Ramona Vogt) Predicted dijet yield as a function of p_T for a Pb-Pb run of 10^6 seconds at luminosity $0.42 \times 10^{27} \text{ cm}^{-2} \text{ s}^{-1}$ and $\sqrt{S_{NN}} = 5.5$ TeV.

2.4 Using UPC Jets To Examine Gluon Correlations

The most detailed distribution of the nucleus is given by the Wigner distribution, $W(x, \vec{b}, \vec{q}_T)$. This encodes the three dimensional, x, \vec{b}, \vec{q}_T , distribution of partons within nuclei, where \vec{q}_T is the transverse momentum of a parton and \vec{b} the impact parameter vector. Recently it has been proposed that angular correlations in the exclusive production of dijets in ultra-peripheral heavy ion collisions might be sensitive to the correlations between the \vec{b} and \vec{q}_T distribution of gluons [32]. For such exclusive processes there is no net electric charge or color exchanged. If the photon fluctuates into a quark-antiquark ($q\bar{q}$) pair within the Pb nuclide, both q and \bar{q} can interact, respectively, with a pair of gluons that have a net color of zero, as shown in Figure 2.20. The angular correlation between the vector sum and vector difference of the two jets in exclusive UPC events is expected to be sensitive to the correlations between gluons [32]. The search for these azimuthal correlations was a principal focus of this analysis. Preliminary results of the azimuthal correlations measurement are described in Chapter 6, systematic effects on the azimuthal correlations measurement are described in Chapter 7, and the final results of the azimuthal correlations measurement for this analysis are given in Chapter 8.

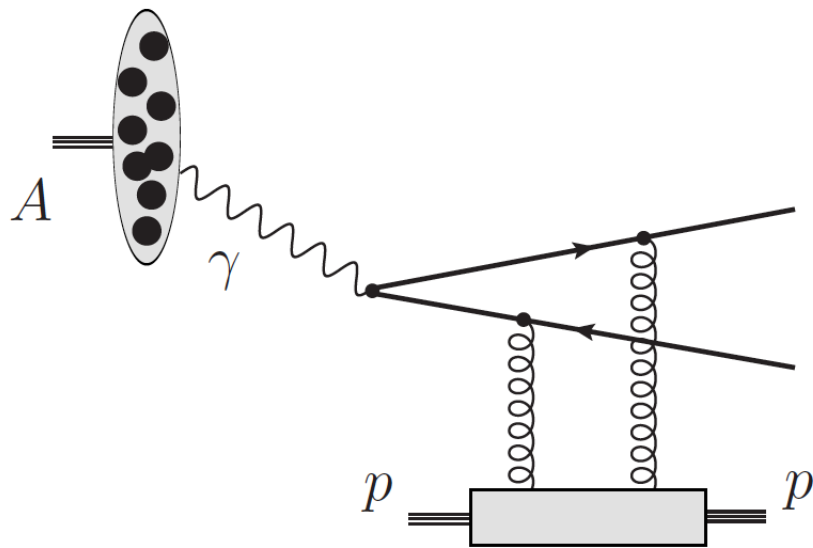


Figure 2.20: ([32], 2) A Feynman diagram of exclusive UPC dijet production is shown here. A $q\bar{q}$ pair interacts with a gluon pair of net color zero, resulting in a dijet with no net color or electric charge exchanged.

Chapter 3

The Compact Muon Solenoid Experiment Part I: Experimental Apparatus

This chapter describes in detail the experimental equipment that was used to gather the data used to perform this UPC dijet analysis. Section 3.1 describes the LHC, the particle collider that was used to accelerate Pb nuclides to the energies at which they were collided. Section 3.2 summarizes the basic principles behind the workings of the types of particle detectors used by the CMS detector. Section 3.3 provides a description of the CMS detector and each of its sub-systems.

3.1 The Large Hadron Collider

The Compact Muon Solenoid (CMS) is one of the detector systems operated by an experimental collaboration at the Large Hadron Collider, which is located at the European Organization for Nuclear Research (CERN). CERN is a laboratory that is a joint project of 22 member states, mostly European, and researchers and institutions throughout the world participate in research activities there. CERN is located on the Franco-Swiss border near Geneva, Switzerland, and its facilities are located in both France and Switzerland. The Large Hadron Collider was built to find the Higgs boson. The Higgs boson was found in 2012, and further studies of the Higgs boson are ongoing. At the same time, the LHC is being used for several other purposes, including searches for physics beyond the standard model and studies of heavy ion physics. The LHC is a proton-proton collider and Pb-Pb collider (specifically, lead-208 isotopes). Two beams of protons or Pb ions are accelerated in opposite directions. The beams cross over into a common beam line at four locations. At those locations are four detector systems that are run by four respective experimental collabo-

rations. These are ALICE, ATLAS, CMS, and LHCb. The LHC has a circumference of about 27 kilometers and is located between 50 and 175 meters underground (tunnel constructed at a slope with a gradient of 1.4%) [25]. A picture of the location of the LHC and the four experiments is shown in Figure 3.1.



Figure 3.1: ([2]) Location of LHC and experiments in the vicinity of Geneva, Switzerland.

Particle accelerators such as the LHC accelerate hadrons with an electric field following the basic principle

$$\mathbf{F} = q\mathbf{E}, \quad (3.1)$$

where \mathbf{E} is the electric field and \mathbf{F} is the force that the electric field exerts on the charged particle q (in the case of the LHC a hadron). The energy the charged particle gains from the electric field that accelerates it is

$$E = qV, \quad (3.2)$$

where V is the electric potential difference across the electric field through which the particle is

accelerated (not to confuse energy E with electric field \mathbf{E}). V is related to \mathbf{E} by

$$V = \int_a^b \mathbf{E} \cdot d\mathbf{l} \quad (3.3)$$

where $d\mathbf{l}$ is an infinitesimal unit of length of the field through which the particle is accelerated and a and b mark the beginning and end points of where the field accelerates the particle.

Prior to entering the LHC, protons and Pb ions are pre-accelerated by a series of smaller accelerators [25] [17]. A diagram of the LHC and its support complex is shown in Figure 3.2. For

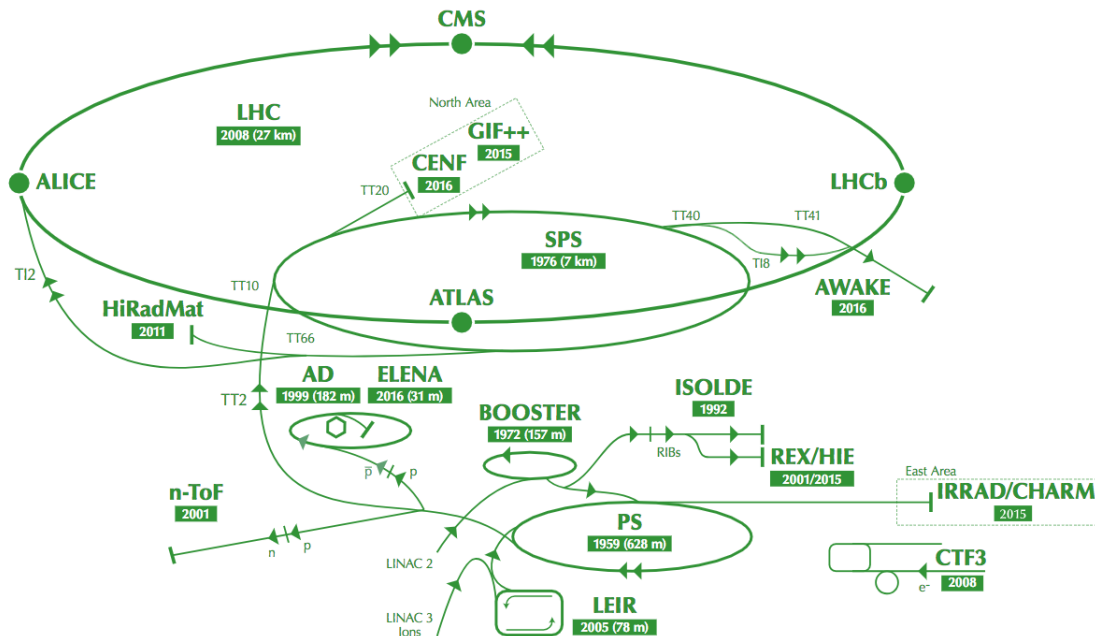


Figure 3.2: ([25], 13) Diagram of LHC and its feeder accelerators and supporting equipment.

protons, the process begins with a bottle of hydrogen from which atoms are taken from and ionized by electric fields. The ionized hydrogen, i.e., protons, are given an initial boost in LINAC2. After LINAC2 they are fed into the PS Booster where they are accelerated to an energy of 50 MeV¹. The PS Booster accelerates them to 1.4 GeV, and they are then fed into the Proton Synchrotron

¹An electron volt (eV) is a unit of energy that is equal to the amount of energy an electron receives after being accelerated through a 1 volt potential. MeV stands for mega, or million, electron volts. Additionally, GeV is a giga-, or billion, electron volts, and TeV is a tera-, or trillion, electron volts.

(PS) where they are accelerated to 25 GeV. Following this, the protons are injected into the Super Proton Synchrotron (SPS) where they are accelerated to 450 GeV. It is at this energy that protons are injected into both rings of the LHC, clockwise in one ring and counter-clockwise in the other ring.

For Pb ions, the process is somewhat different. They are produced from a highly purified ^{208}Pb sample that is heated to a temperature of about 800°C . The Pb vapor that results is partly ionized (stripped of electrons) by an electron current. The partially ionized Pb nuclides are accelerated to 4.2 MeV/u (that is, MeV per nucleon) by LINAC3. They then pass through a carbon foil which ionizes them further. They are next injected into the Low Energy Ion Ring (LEIR), which accelerates them to 72 MeV/u. Following this they are transferred to the PS, which accelerates them to 5.9 GeV/u. They are sent through a second foil which completely ionizes them before being sent to the SPS. The SPS accelerates them to 177 GeV/u, and they are then injected into both rings of the LHC, clockwise and counterclockwise as with the protons. Injecting Pb ions into one ring and protons into the other ring for proton-Pb collisions can also be done. Protons and Pb ions are injected into the LHC in groupings called bunches, which are grouped in the booster machines.

The LHC itself accelerates protons up to 6.5 TeV and Pb nuclides up to 2.51 TeV/u. The electric fields which accelerate the particles are supplied by 16 radiofrequency (RF) cavities, with 8 RF cavities per ring. An RF cavity is an open space inside a conducting material that has dimensions causing electromagnetic waves at certain frequencies to resonate, thereby establishing a standing wave and consequently a steady electric field from which charged particles can be accelerated [47]. An RF cavity diagram is shown in Figure 3.3, and a photograph of the exterior of the LHC's RF cavities is shown in Figure 3.4. Each RF cavity on the LHC is supplied with electromagnetic waves by a single klystron that is connected to the cavity by a waveguide [14]. A klystron, shown in Figure 3.5, is a device that uses a stream of electrons to amplify the power of an electromagnetic wave signal [47] [33]. The electrons are first emitted/accelerated by a cathode ray tube and then bunched together in a resonant cavity by the electromagnetic wave signal to be amplified. Those electron bunches then arrive at another resonant cavity. The bunches arrive at the other cavity at the

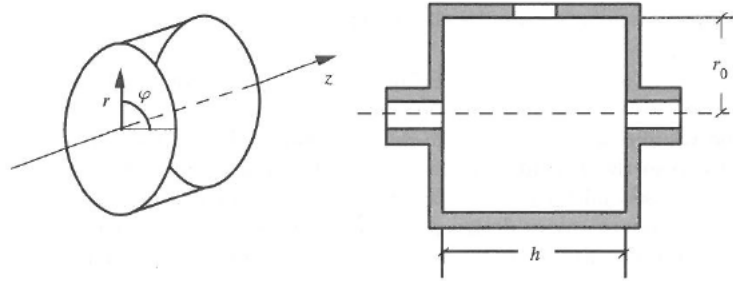


Figure 3.3: ([47], 147) Diagram of a cylindrically-shaped RF cavity. The geometry with cylindrical coordinates is shown on the left. The right shows a side-view cross section, where the cavity has length h and radius r_0 . Also visible on the right is the beam inlet and outlet on each end of the cavity as well as the waveguide input at the top.

frequency of the electromagnetic signal, and also arrive just when the electric field of the signal acts to slow down the electrons. Electron kinetic energy is converted to electric field potential energy, thereby amplifying the power of the electromagnetic wave. The amplified electromagnetic waves are subsequently sent to the RF cavity by the waveguide. The electromagnetic waves that accelerate particles in the LHC have a frequency of 400 megahertz (MHz), and their electric fields have a strength of 5 MeV/m, each RF cavity yielding a total of 2 MeV per pass. The electromagnetic wave frequency can be changed so that it is synchronized with the increasing speed of the particle as the particle is accelerated. However, in the LHC, this change is not more than a few Hertz in practice because the particles are already traveling at nearly the speed of light when they are injected. Due to the special relativistic limit of the energy of a massive particle going to infinity at the speed of light, the large energy increase that the LHC imparts on the protons and lead ions results in extremely little speed increase. The RF cavities take about 20 minutes to accelerate protons and lead ions from their injection energy to their maximum energy for collisions. The electric fields established by the RF cavities also serve the purpose of keeping the bunches of protons or lead nuclides tightly bunched.

The protons and lead nuclides in the LHC are accelerated radially, i.e., "steered" around the rings, by magnetic fields provided by superconducting magnets [25] [33]. An electric charge

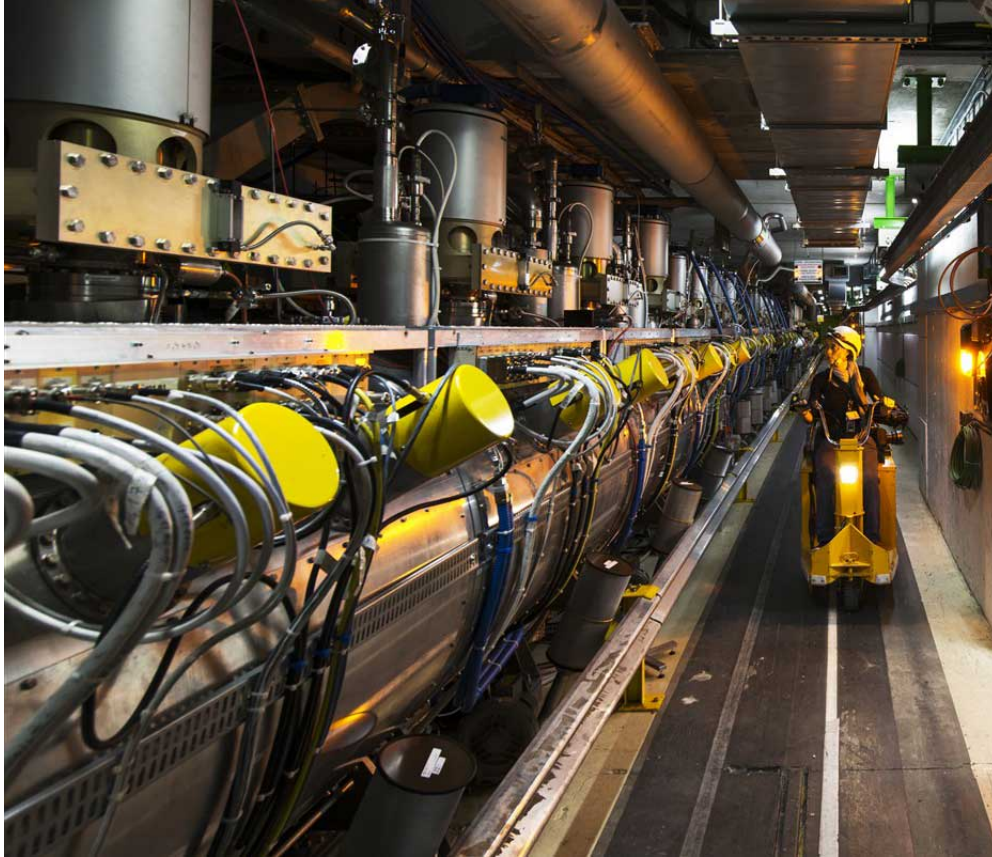


Figure 3.4: ([1]) Photograph of LHC RF cavities.

moving through a magnetic field experiences a force

$$\mathbf{F} = q\mathbf{v} \times \mathbf{B} \quad (3.4)$$

where \mathbf{F} is the force the magnetic field \mathbf{B} exerts on charge q and \mathbf{v} is the velocity of q . The LHC has 1232 main dipole magnets for steering the beams. Each produces a magnetic field of 7.74 tesla (T). This is accomplished by the use of cables made of a niobium-titanium alloy. There are 36 windings of this cable within a few cm, and the cable has a diameter of 15 mm. These cables become superconducting at 10 K (-263.2°C). In a superconducting state, they have no electrical resistance. They are cooled to a temperature of 1.9 K (-271.3°C) by a refrigeration system using liquid nitrogen and helium as working fluids. This enables the cables to carry an electric current of as much as 11850 Amperes (A), and produce the magnetic fields for steering the beam that are

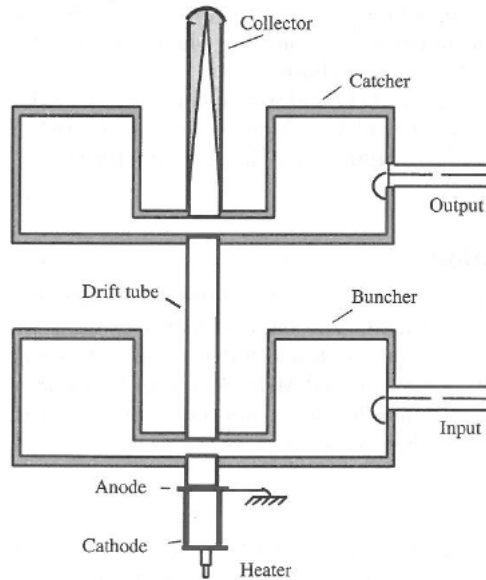


Figure 3.5: ([47], 156) Diagram of a klystron. A steady stream of electrons is accelerated by a voltage across a cathode ray tube consisting of a heater, cathode, and anode. The buncher cavity receives the steady stream of electrons and electromagnetic wave signals to be amplified, which organizes the electrons into bunches. The electron bunches travel through the drift tube and arrive at the catcher cavity at the frequency of the electromagnetic wave and at such a time where the electric field in the cavity opposes their motion. The amplified electromagnetic wave is then outputted through a waveguide while the decelerated electrons end their run in the collector.

designed to get as high as 8.33 T. There are also 392 quadrupole magnets that focus the beams. In total, the LHC contains 9593 magnets. A cutaway diagram of an LHC dipole magnet is shown in Figure 3.6, and the shape of its magnetic fields is shown in Figure 3.7.

The protons in the LHC collide at the crossover points where the detector complexes are located. The bunch spacing and frequency in each ring is established such that the bunches will collide at the centers of the detectors. The bunch spacing is 7.5 m, corresponding to a time of 25 nanoseconds (ns) between collisions [25]. The proton-proton collisions have a center of momentum energy of 13 TeV, and the Pb-Pb collisions have one of 5.02 TeV. The design parameters of the LHC allow for a maximum possible proton beam energy of 7 TeV and maximum possible Pb ion energy of 2.76 TeV/u in the future, and maximum possible center of momentum energy of 14 TeV and 5.52 TeV/u, respectively [14]. The beamlines are maintained at a vacuum of 10^{-13}

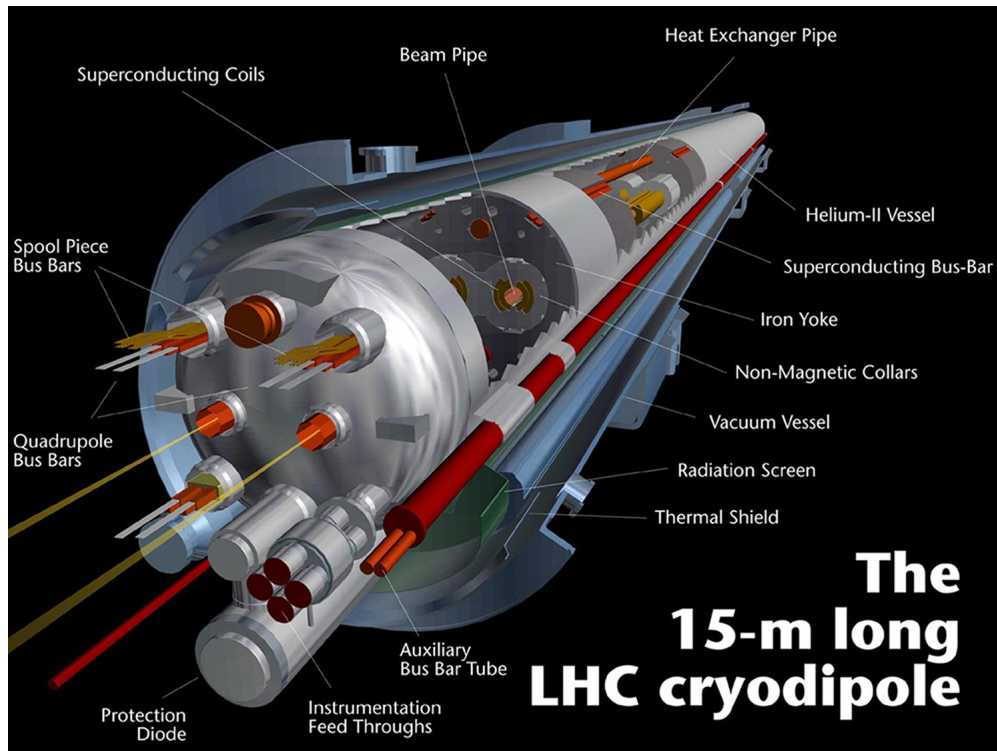


Figure 3.6: ([3]) A cutaway diagram, with components labeled, of a dipole magnet for steering the beams in the LHC.

atmospheres to avoid collisions with gas molecules as much as possible.

3.2 Basic Detector Principles

Detectors of high energy nuclear/subatomic interactions rely on the ionization of nearby materials that such interactions cause in order to detect and ultimately reconstruct those interactions. There are three basic categories of detectors that CMS utilizes.

The first is that of semiconductor detectors. Semiconductor detectors consist of a semiconductor material, such as silicon, connected in an electrical circuit. Radiation that results from high energy nuclear/subatomic interactions elevates the energy of atomic electrons when it passes through the semiconductor. A number of these electrons are elevated to conduction energy levels. With a potential difference, i.e., voltage, applied across the semiconductor, the electrons then constitute a pulse of current that is directly measurable as a signal.

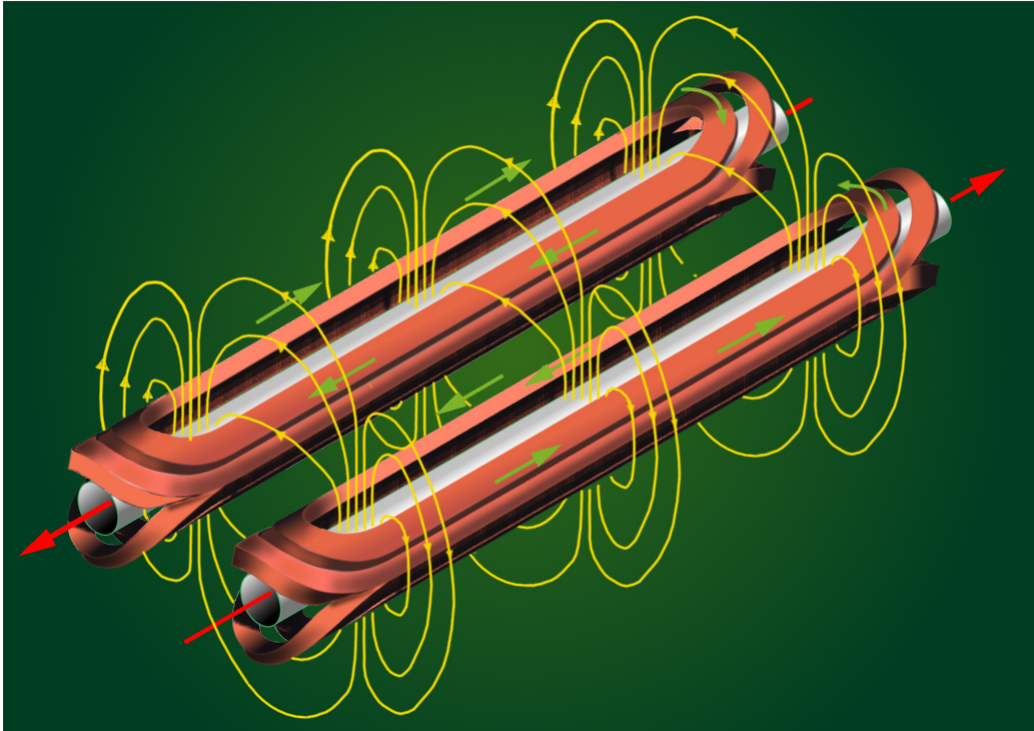


Figure 3.7: ([3]) Magnetic fields of an LHC dipole magnet.

The second category is that of gas-filled chambers ([4], 2-55 - 2-58). Gas-filled chambers consist of a hollow metal cylinder and a conducting wire that runs along the cylinder's axis, as shown in Figure 3.8. The hollow cylinder is filled with gas. A large voltage is applied between the cylinder, which serves as the negative electrode (cathode), and the wire, which serves as the positive electrode (anode). Radiation from high energy nuclear/subatomic interactions that pass through the chamber will cause ionizations of the gas atoms or molecules, resulting in the formation of ion pairs of electrons and positively charged ions. The electric potential will accelerate the electrons toward the positively-charged central wire and the ions toward the negatively-charged cylinder. When the electrons reach the wire, the result is a pulse of current that corresponds to a signal. In general, a higher voltage applied across the chamber will make it more sensitive to a lower flux of ionizing radiation.

The third category is that of scintillation detectors ([4], 2-58 - 2-60). Scintillation detectors depend upon solid or liquid materials, known as phosphors, that emit light when radiation from

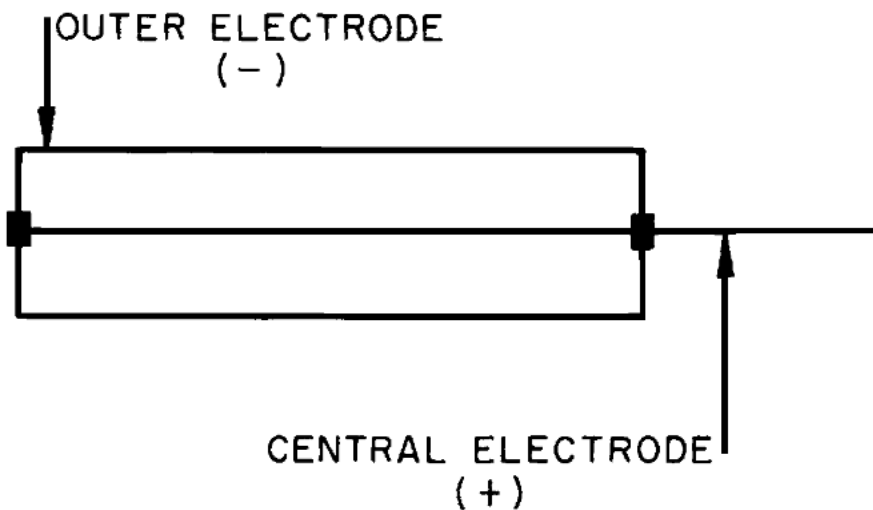


Figure 3.8: ([4], 2-56) Basic diagram of a gas-filled chamber detector.

high energy nuclear/subatomic interactions interacts with/ionizes the material. When this happens, the atoms or molecules of the material then emit the energy they have gained from the radiation as light. This flash of light from each interacting particle is known as a scintillation. The overall intensity of the light is proportional to the energy of the radiation. A basic diagram of a scintillation detector is showing in Figure 3.9. The scintillating material is optically connected to a photomultiplier tube. A photomultiplier tube collects a light signal and converts it into an electronic signal that can be measured. Figure 3.10 shows a diagram of how a photomultiplier tube works. It consists of a photocathode followed by a series of electrodes called dynodes. Its basic working principle is as follows. Scintillation light strikes a photocathode, which frees electrons via the photoelectric effect. There is a voltage applied between the dynodes, and the overall voltage across the chain of dynodes is large. The voltage difference between the photocathode and the first dynode causes the electrons to accelerate toward the first dynode, and when they strike it, they cause additional ionizations, which free more electrons. This amplified number of electrons is then accelerated toward the second dynode, where yet more ionizations occur and more electrons are freed. The overall effect is a cascade of electrons that yield a pulse of current at the last dynode that corresponds to a signal. The strength of that signal is ultimately proportional to the energy

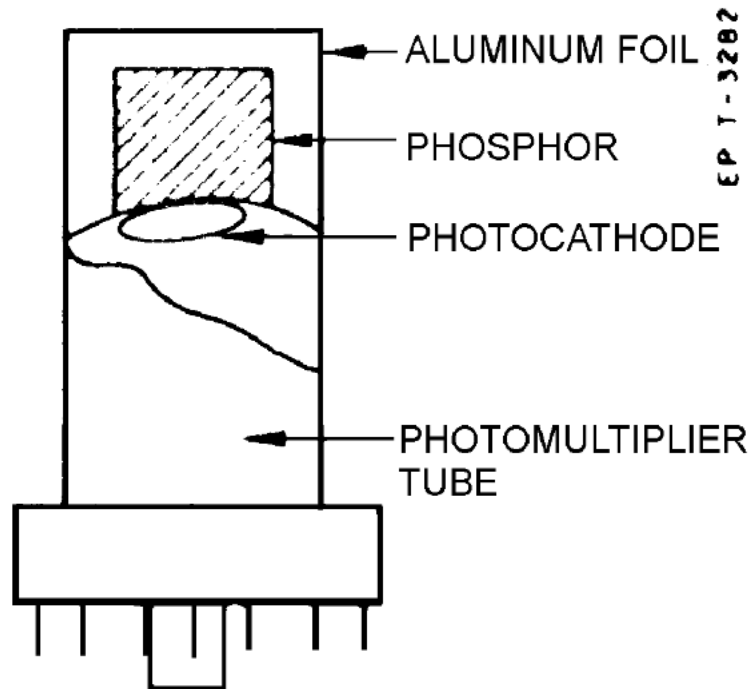


Figure 3.9: ([4], 2-59) Diagram of a scintillation detector. The aluminum foil in this example serves to reflect the light flashes toward the photomultiplier tube.

of the radiation that caused the initial scintillation. This makes scintillation detectors optimal for measuring the energy of high energy nuclear interactions.

A special type of scintillation detector is known as a Cherenkov detector. Instead of a phosphor, a Cherenkov detector is built with a dielectric. A dielectric is an electrically insulating material that becomes polarized in the presence of an applied electric field, resulting in the establishment of an electric field within the material that partially cancels the applied electric field. A charged particle traveling through the dielectric applies such a field that causes polarization. If the particle moves at a faster speed than the dielectric medium can respond, the changes in the electric field are not steady, and electromagnetic radiation in the form of scintillation light is emitted as a result. The speed of light in a dielectric medium is slower than c (the speed of light in a vacuum), and if the particle's speed exceeds that of light in the medium, the light will be emitted as a Mach cone with its apex at the moving particle (similar in principle to a sonic boom). The angle of this cone

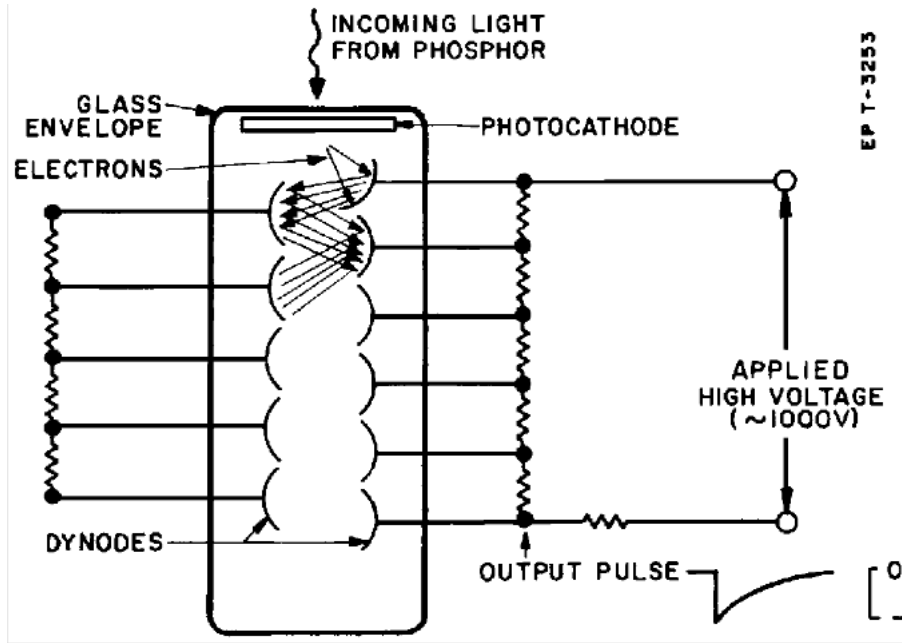


Figure 3.10: ([4], 2-60) Diagram of a photomultiplier tube in a scintillation detector. In this case, a total potential of 1000 volts is applied across all of the dynodes.

apex, which can be measured, yields the speed of the particle by the following relation:

$$\cos \theta = \frac{c}{nv}, \quad (3.5)$$

where θ is the cone apex angle, n is the index of refraction of the phosphor, and v is the speed of the particle.

3.3 The CMS Detector Complex

The Compact Muon Solenoid is a cylindrical detector complex that is built within and around a solenoid magnet. It is 21.6 meters long and 14.6 meters in diameter, and has a mass of 12,500 tonnes ([11], 9). The cylindrical complex is generally constructed with a "barrel" region and two "endcaps" on each end of the barrel. Aside from the solenoid magnet, CMS consists of a silicon tracker, an electromagnetic calorimeter, a hadronic calorimeter, and a muon detector/tracker system. The muon detector is located outside of the solenoid coils, and the other sections are located

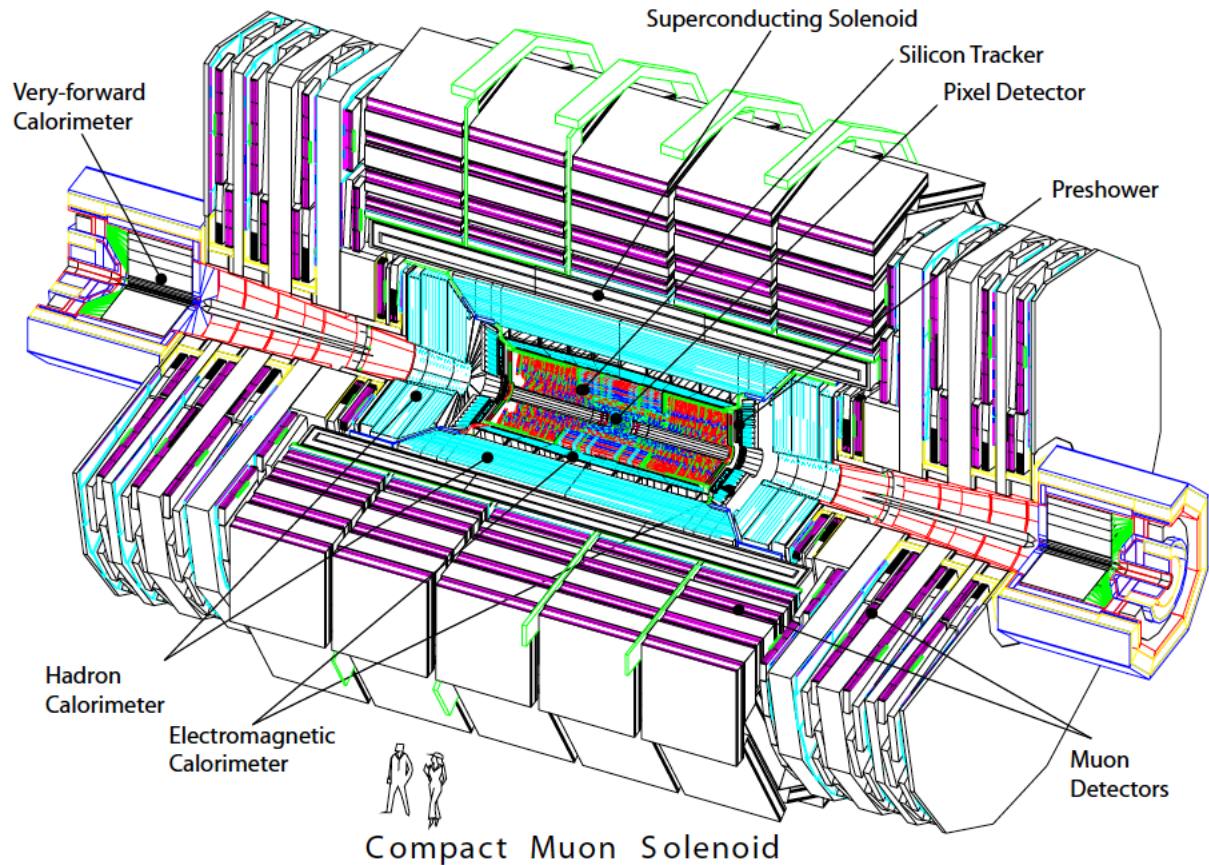


Figure 3.11: ([11], 8) The CMS detector complex and its components. Note that the ZDCs, which are located forward of the main complex on each end, are not shown.

inside of the coils. The silicon tracker is the innermost component surrounding the beamline and interaction point. The electromagnetic calorimeter is located outside of the silicon tracker, and the hadronic calorimeter surrounds the electromagnetic calorimeter. The hadronic calorimeter includes the hadronic forward (HF) detectors at each end of the silicon tracker. The muon detector, silicon tracker, the electromagnetic calorimeter, and the hadronic calorimeter all provide full azimuthal coverage of the interaction point in CMS. Additionally, there are two more calorimeters in the forward regions of the detector, CASTOR and the Zero Degree Calorimeter (ZDC). A diagram of the CMS Detector and its components is shown in Figure 3.11.

The coordinate convention for CMS is a right-handed coordinate system ([19], 3). In the rectangular coordinate system, \hat{x} points toward the center of the LHC ring, \hat{y} points up and perpendicular

to the plane of the LHC ring, and \hat{z} points in the counter-clockwise direction at any point along the LHC beamline when looking at the plane of the LHC ring from above. For the convenience of CMS, other coordinates are also used. r refers to the radial distance from the beamline, the angle θ is defined relative to $+\hat{z}$, and the azimuthal angle ϕ is defined relative to the \hat{x} -axis in the x - y plane. It is even more convenient to express the angle θ in terms of a quantity that is relativistically invariant in all reference frames. That quantity is known as pseudo-rapidity, η :

$$\eta = -\ln \left[\tan \frac{\theta}{2} \right]. \quad (3.6)$$

When $pc \gg mc^2$, as is often the case with particles produced in high energy collisions, pseudo-rapidity approaches equality with rapidity, that is

$$\eta \approx y. \quad (3.7)$$

3.3.1 The Solenoid Magnet

The central feature of the CMS detector is the superconducting solenoid magnet. The magnet generates a magnetic field, the purpose of which is to radially accelerate charged particles. The curvature of the path of those particles, as measured by the silicon tracker and (for muons) the muon detector, can then be used to determine the magnitude of the spatial momentum vector of the charged particles. The magnetic field is generated specifically by a superconducting coil with 2168 turns, a length of 12.9 meters, and an inner bore diameter of 5.9 meters ([11], 9-10). The coil carries a current of 19.5 kA. Exterior to the coil is a steel skeleton for CMS that serves three purposes: 1) to provide structural form and integrity to the CMS cylindrical detector complex as a whole, 2) to provide a specific structural frame for the muon detector/tracker, and 3) to "capture" the magnetic field of the solenoid outside of the coil such that the muon detector/tracker components have a uniform magnetic field. The steel skeleton consists of five three-layered dodecagonal wheels in the barrel region and three disks at either endcap region, as shown in Figure 3.12 [18]. The steel

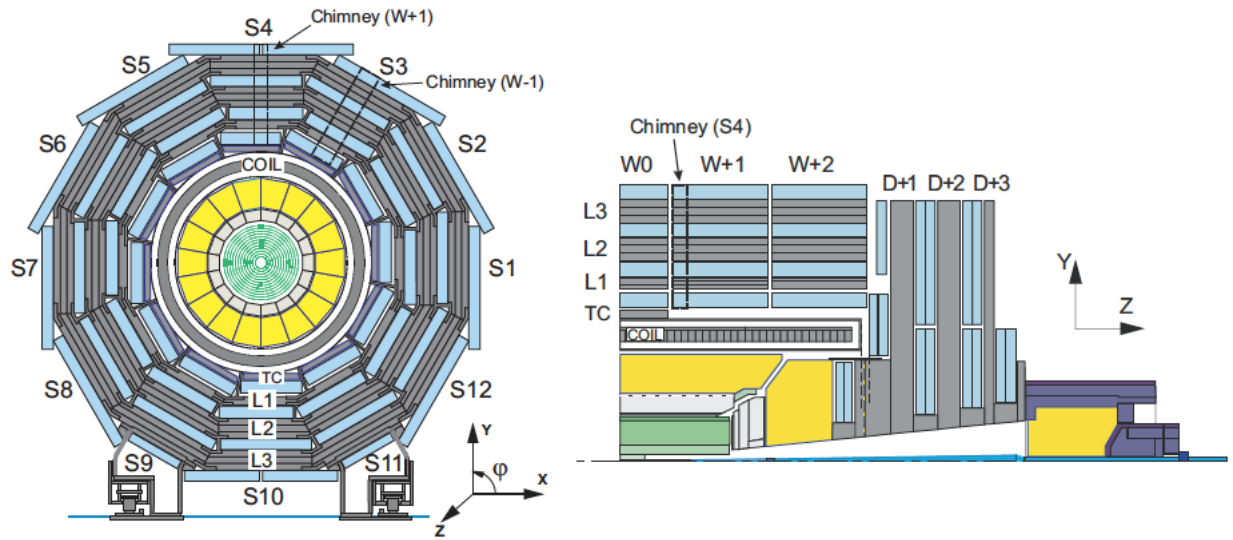


Figure 3.12: ([18], 1) Diagram of the CMS structural steel skeleton is shown here. In the barrel region, there are five wheel sections (labeled with prefix W) that run the length of the barrel. These wheel sections have three layers (L) plus one extra "tail catcher" (TC) layer in the W0 wheel (see Hadronic Calorimeter subsection below). The wheels are dodecagonal-shaped with 12 azimuthal sections (S). In the two endcap sections, there are three disks (D). The "Chimneys" are for the routing of cryogenic and electrical connections. The light blue sections are the components of the muon detector/tracker.

skeleton has a mass of 12000 tonnes, making up the bulk of the mass of the CMS detector. The solenoid generates a magnetic field of up to 4 T inside the coil and up to 2 T in the sections of the steel skeleton containing the muon detector/tracker components, and can store up to 2.7 GJ of energy. Thus far, however, the CMS solenoid magnet has been operated at a maximum of 3.8 T inside the coil and up to 1.9 T in the muon detector. Figure 3.13 shows a map of the design magnetic field strength and flux from the CMS solenoid magnet.

3.3.2 The Silicon Tracker

The silicon tracker is a semiconductor detector. It is the CMS component that lies closest to the interaction point, immediately surrounding the beamline [19]. The purpose of the silicon tracker is to provide position measurements of the charged particles that strike it. It is 5.8 meters long and has a diameter of 2.5 meters. The silicon tracker consists of two principal components: a small

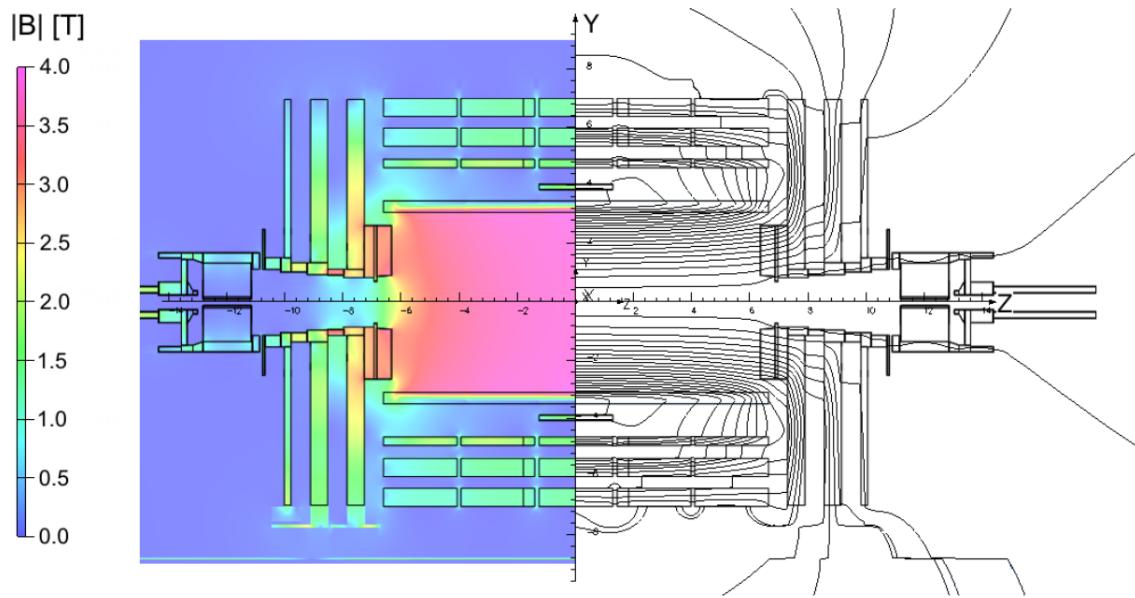


Figure 3.13: ([18], 6) CMS magnetic field magnitude (left) and flux density right at a maximum of 3.8 T inside the coil. Each field line on the right represents a magnetic flux increment of 6 Wb.

pixel detector closest to the beamline and a large strip detector outside of the pixel detector. A cross-sectional diagram of one half of the silicon tracker is shown in Figure 3.14. Pseudo-rapidity ranges of $-2.4 < \eta < 2.4$ are fully covered by the silicon tracker, as shown in detail in Figure 3.15.

The pixel detector consists of three cylindrical barrel layers at radii of 4.4 cm, 7.3 cm, and 10.2 cm, respectively. It also consists of two endcap disks on each end at $z = \pm 34.5$ cm and ± 46.5 cm. It has a total area of about 1m^2 and contains 66 million pixels. The pixels are roughly square in shape with an area of $100 \times 150 \mu\text{m}^2$, their silicon layer has a thickness of $285 \mu\text{m}$, and they have a resolution of about $10 \mu\text{m}$ for $r\phi$ and $20\text{-}40 \mu\text{m}$ for z ([19], 3-4; [11], 19-20). A basic layout of the pixel detector is shown in Figure 3.16.

The strip detector is made up of four sections: the Tracker Inner Barrel (TIB), the Tracker Inner Disks (TID), the Tracker Outer Barrel (TOB), and the Tracker End Caps (TEC) ([19], 3-4; [11], 19-20). The TIB and TID cover $r < 55$ cm and $|z| < 118$ cm. The TIB has four barrel layers, and the TID has three disks on each end of the TIB. The TIB provides position measurements in $r\phi$ with a resolution of $23\text{-}34 \mu\text{m}$ and in z with a resolution of $230 \mu\text{m}$; and the TIDs provides position

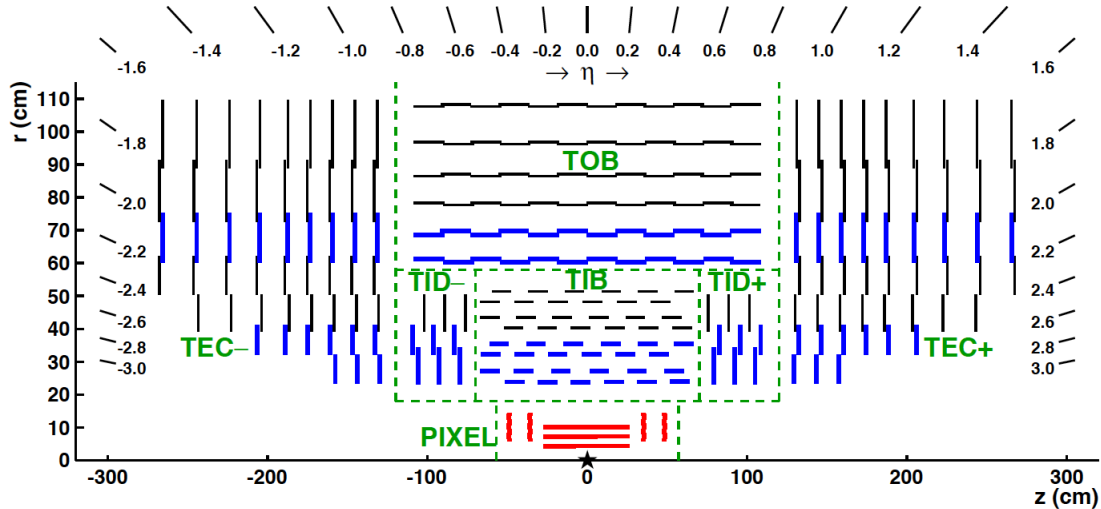


Figure 3.14: ([19], 3) Cross-sectional diagram of the silicon detector on one side of the beamline.

measurements in $r\phi$ with a similar resolution. The TOB covers $r > 55$ cm and $|z| < 118$ cm. It has six barrel layers that yield position measurements in $r\phi$ with a resolution of $35\text{-}52\ \mu\text{m}$ and in z with a resolution of $530\ \mu\text{m}$. The two TECs on each end have nine disks. The TECs cover the ranges $124 < |z| < 282$ cm and have a similar resolution in $r\phi$ to the TOB. The strip detector has a total area of about $198\ \text{m}^2$ and contains 9.6 million strips. In the TIB, TID, and inner three TEC rings, the silicon layer of the strips is $320\ \mu\text{m}$ thick, while the TOB and the rest of the TEC have strips with a silicon layer thickness of $500\ \mu\text{m}$.

3.3.3 The Electromagnetic Calorimeter

Lying outside of the silicon tracker is the electromagnetic calorimeter [11], [23]. The electromagnetic calorimeter is a scintillation detector, the purpose of which is to measure the energy of electrons, positrons, and photons. It also works in concert with the hadronic calorimeter to measure the energy and position of hadronic jets. The scintillation material in the electromagnetic calorimeter is a high density, transparent material lead tungstate (PbWO_4). PbWO_4 has a short radiation length X_0 (that is, it will attenuate the energy of photons and electrons/positrons over a small distance) of 0.89 cm, and the scintillation events in PbWO_4 are fast such that 80% of the

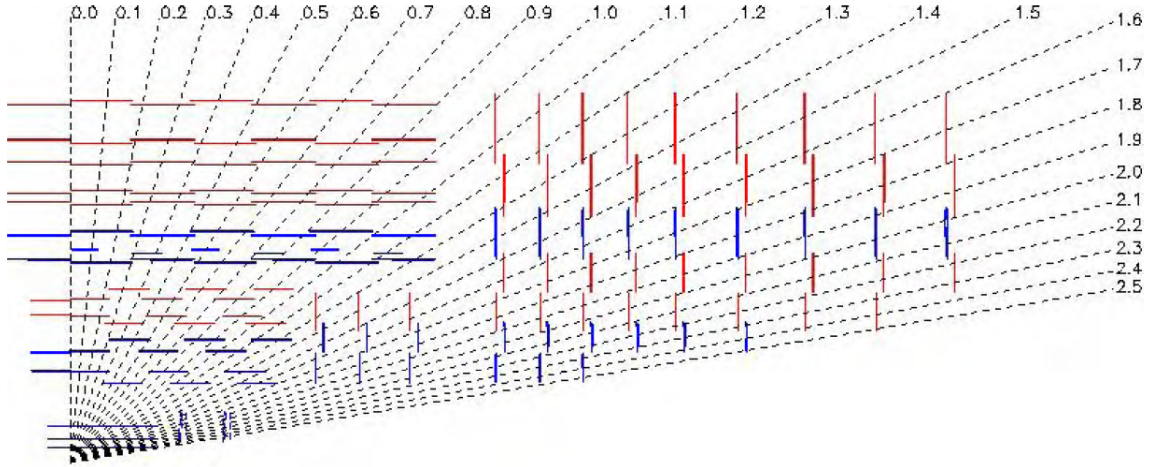


Figure 3.15: ([11], 18) Pseudorapidity layout and limit of the silicon tracker as shown on one quarter of the tracker.

light in the event is emitted within 25 ns (the time interval between LHC particle bunches).

The electromagnetic calorimeter has a barrel section and two endcap sections on each end of the barrel section. The barrel section consists of 61200 PbWO_4 crystals and each endcap section consists of 7324 PbWO_4 crystals, for a total of 75848 crystals in the electromagnetic calorimeter. A PbWO_4 crystal from the electromagnetic calorimeter is shown in Figure 3.17. The inner radius of the barrel section is 129 cm, and the barrel section covers the pseudorapidity range $0 < |\eta| < 1.479$. The granularity of each crystal in the barrel section is $\Delta\eta \times \Delta\phi = 0.0174 \times 0.0174$ (1° in $\Delta\eta$ and $\Delta\phi$). These crystals have a front face area of $22 \times 22 \text{ mm}^2$, a rear face area of $26 \times 26 \text{ mm}^2$ ([23] 92), and a length of 23 cm ($= 25.8X_0$). The crystals are angularly aligned with the interaction point plus an additional offset of 3° in both ϕ and η , the offset being there to avoid the boundary between crystals aligning with possible particle trajectories. The faces of the endcaps are located at $|z| = 314$ cm, and the endcaps cover the pseudorapidity range $1.479 < |\eta| < 3.0$. The crystals in the endcaps have a front face area of $28.62 \times 28.62 \text{ mm}^2$, a rear face area of $30.00 \times 30.00 \text{ mm}^2$ ([23] 93,) and a length of 22 cm ($= 24.7X_0$). The endcap crystals align with a focus 130 cm beyond the interaction point so that there is an angular offset of between 2° and 8° , again to avoid crystal boundaries lining up with particle trajectories.

There is also a preshower detector attached to the front of the endcaps [23]. The main purpose

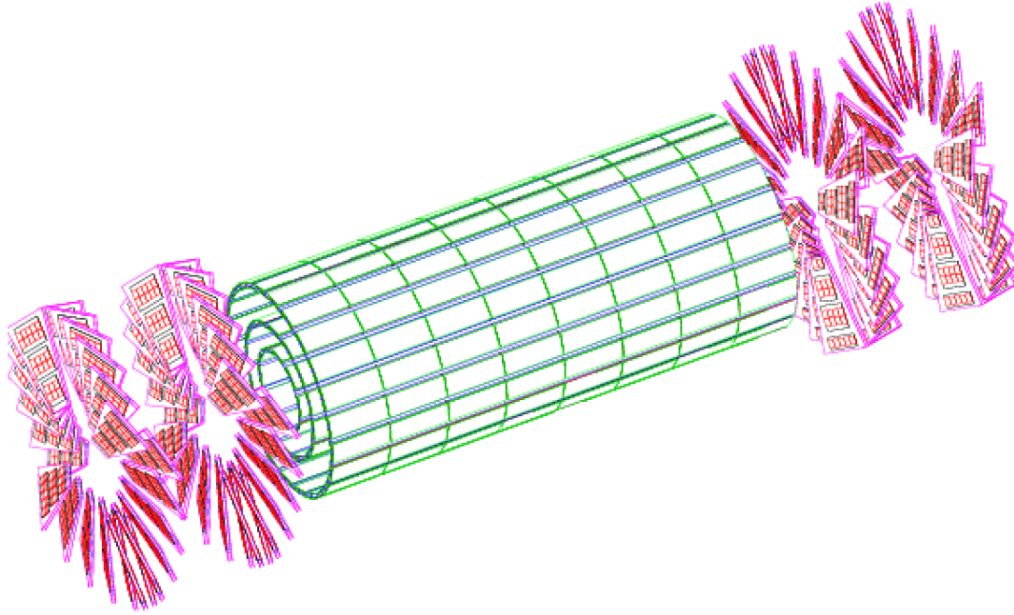


Figure 3.16: ([11], 20) Layout of the pixel detector, with the three barrel layers and two endcap disks on each end clearly shown.

of the preshower detector is to identify neutral pions in the pseudorapidity ranges $1.653 < |\eta| < 2.6$, which the preshower detector covers. It also helps to distinguish electrons from minimum ionizing particles and improves the position measurement of electrons and photons. The preshower detector consists of two layers of lead, each of which is backed by a silicon strip detector. The preshower detector is a total of 20 cm thick. The layout of the electromagnetic calorimeter is shown in Figure 3.18.

The energy resolution of the electromagnetic calorimeter was measured with an electron test beam at CERN [11] [23]. The result of this test is shown in Figure 3.19. The energy resolution improves with increasing energy and is expressed by

$$\left(\frac{\sigma}{E}\right)^2 = \left(\frac{S}{\sqrt{E}}\right)^2 + \left(\frac{N}{E}\right)^2 + C^2, \quad (3.8)$$

where S accounts for stochastic effects, N accounts for noise, and C is a constant. The measured results for these terms are given in Figure 3.19.

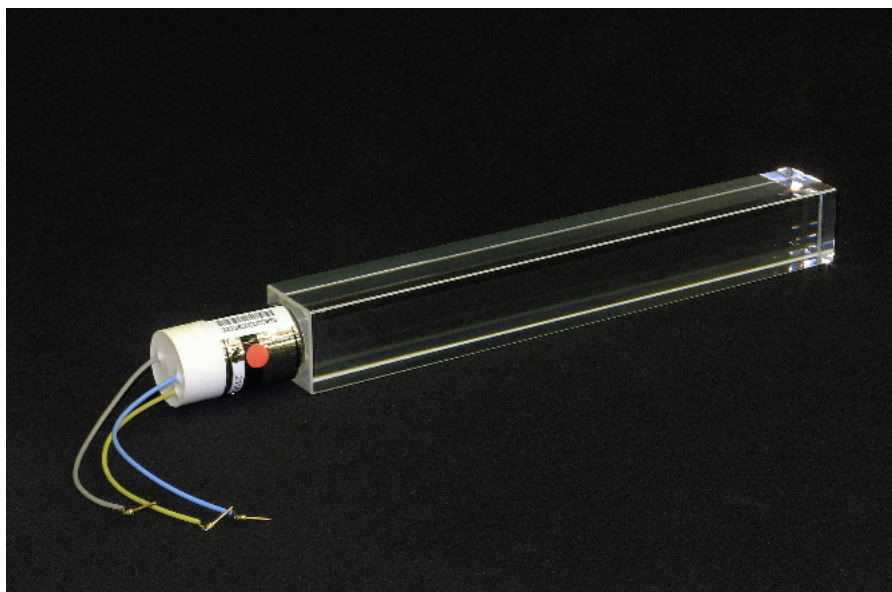


Figure 3.17: ([23], 91) An electromagnetic calorimeter PbWO_4 crystal, with photomultiplier tube attached, is shown here. This particular crystal is from the endcap section. The barrel section crystals are somewhat longer and more narrow, but are otherwise similar.

3.3.4 The Hadronic Calorimeter

The hadronic calorimeter is largely positioned between the electromagnetic calorimeter and the solenoid magnet coil, although it has components beyond the coil and in very forward regions on the end of the CMS cylinder [11] [23]. It has four general sections: the hadron barrel (HB), the hadron outer (HO), the hadron endcap (HE), and the hadron forward (HF). The hadronic calorimeter is a scintillation detector whose purpose is to measure the energy of hadrons such as protons, anti-protons, neutrons, pions, etc. It measures the energy and position of hadronic jets, with assistance from the electromagnetic calorimeter. Figure 3.20 shows the overall layout of the hadronic calorimeter and its four general sections.

There is an additional challenge, as compared to the electromagnetic calorimeter, posed by measuring hadronic energy in a scintillation detector. The interactions that the hadrons undergo with the calorimeter materials, which allow their energy to be measured, typically occur by means of the strong nuclear force, but the interactions behind the workings of a scintillation detector are electromagnetic. It is therefore necessary for a scintillation detector that measures hadron energy

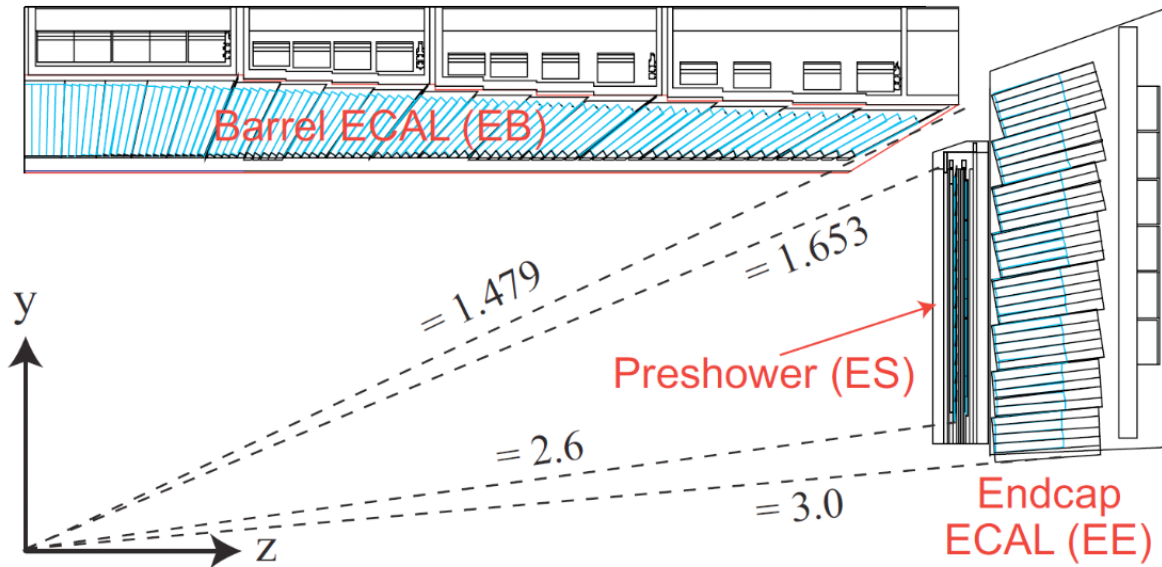


Figure 3.18: ([34], 33) Layout of the electromagnetic calorimeter, as shown with a one quarter section. The pseudorapidity limits of the barrel section, endcap section, and preshower device are shown. Notice the angular arrangement of the PbWO_4 crystals in the barrel and endcap sections.

to incorporate absorber material, in which the hadronic interactions take place, to be interspersed with scintillation material, in which the radiation that results from the hadronic interaction in the absorber material causes the ionizations that yield scintillation. Tiles of scintillator material used in the hadronic calorimeter are shown in Figure 3.21.

The necessity of capturing all of the hadronic energy in the calorimeter along with the general need to confine the hadronic calorimeter to the space between the electromagnetic calorimeter and the magnet coil (so as not to interfere with the design of the muon detector) greatly influenced the design and construction of the hadronic calorimeter. This resulted in the use of very heavy, dense, and mostly non-magnetic absorber materials in the hadronic calorimeter to make interaction lengths as short as practical, to minimize the amount of scintillator material to as little as necessary, and to avoid distorting the solenoidal magnetic field of CMS.

The HB section surrounds the barrel section of the electromagnetic calorimeter and lies immediately inside of the solenoid magnet coil. For absorber material, it has 14 non-magnetic brass layers plus two external stainless steel layers for structural strength. These layers are parallel to

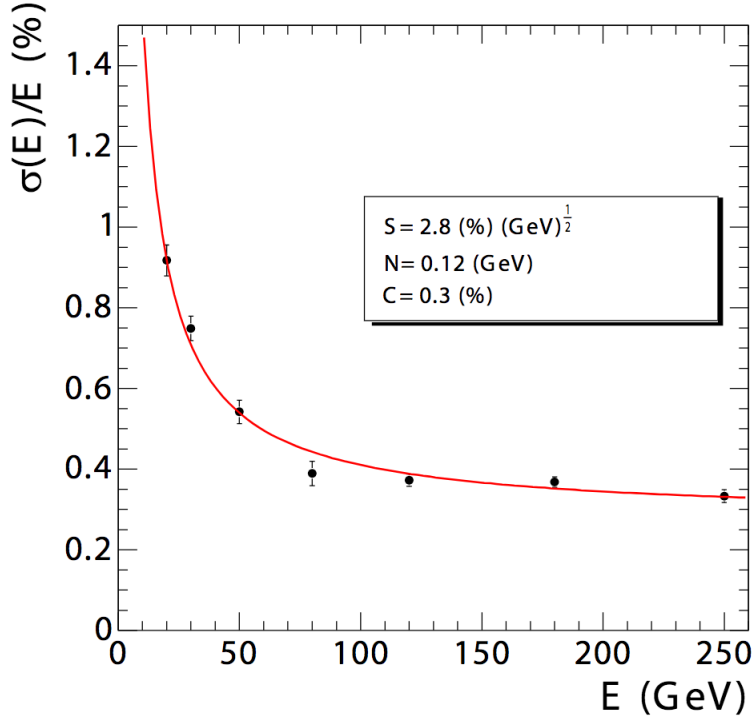


Figure 3.19: ([23], 5) Electromagnetic calorimeter energy resolution as measured with test beam. Equation 3.8, with the values of S , N , and C shown in the plot, expresses these results.

the beamline. The brass is known as C26000 cartridge brass. It is 70% copper and 30% zinc, with a density of 8.53 g/cm^3 , a radiation length of 1.49 cm, and an interaction length² of 16.42 cm. The inner steel plate is 4 cm thick, the outer steel plate is 7.5 cm thick, the first eight brass layers are 5.05 cm thick, and the last six brass plates are 5.65 cm thick. Altogether, this adds up to 5.82 interaction lengths at 90° to the beamline. The absorber layers are interspersed with Kuraray SCSN81 plastic scintillator plates with a thickness of 3.7 mm. There are additional scintillator plates outside of the steel support plate: Bicron BC408 right outside of the electromagnetic calorimeter barrel, and Kuraray SCSN81 right inside of the magnet coil, each of which is 9 mm thick. The scintillator plates have optical fibers with a 0.94 mm diameter embedded in them for collection and transmission of the scintillation light to photomultiplier tubes. The HB covers the pseudorapidity range $-1.4 < \eta < 1.4$ and has a granularity of $\Delta\eta \times \Delta\phi = 0.087 \times 0.087$. Part of the HB is shown in Figure 3.22.

²The interaction length is the average length a hadron travels before interacting with the absorber material nuclei.

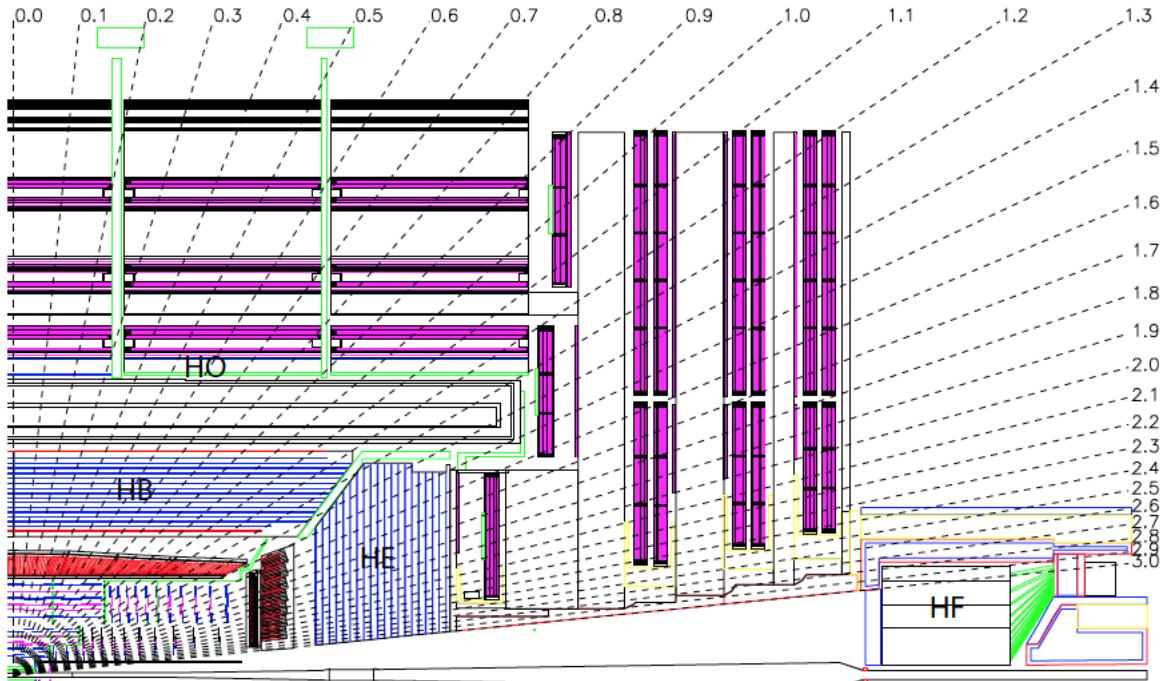


Figure 3.20: ([23], 123) Diagram of one quarter of the CMS detector complex that shows the hadronic calorimeter and specifically the locations of HB, HO, HE, and HF. Note the pseudorapidity scale plot that is superimposed up to $\eta=3.0$.

The HO section lies immediately outside of the magnet coil. It serves as a "tail catcher." The HB section is unable to capture all of the hadronic energy in the low pseudorapidity regions, so the HO serves to capture the remaining energy that escapes the HB. The HO uses the magnet coil as an absorber layer with an interaction length of 1.4 at 90° . The HO is divided into 5 sections, i.e., rings, each of which encircle the magnet coil and are mounted on an iron frame. The central ring has scintillator layers mounted on either side of the iron frame, 19.5 cm thick, at $r = 3.82$ m and 4.07 m, respectively. The other rings have one scintillator layer at 4.07 m. The iron frame serves as an additional absorber layer. The HO combined with the HB extends the total interaction length to 11.8 except at the boundary of the HB and HE. The scintillator layers are made of Bicron BC408 scintillator plates that are 10 mm thick. Optical fibers of diameter 0.94 mm are embedded in the plates for collection and transmission of scintillation light to photomultiplier tubes. HO covers the pseudorapidity range $-1.262 < \eta < 1.262$ and, like HB, has a granularity of $\Delta\eta \times \Delta\phi = 0.087 \times$

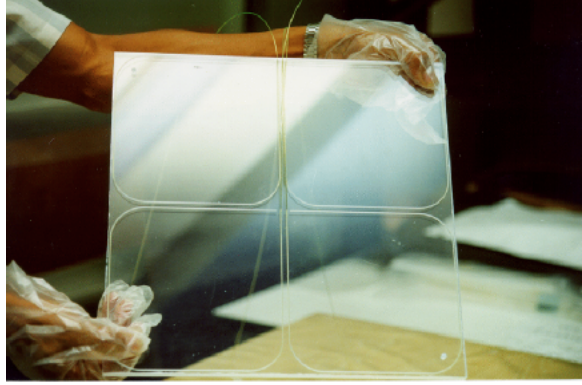


Figure 3.21: ([23], 143) Scintillator tiles used in the hadronic calorimeter. Note the optical fibers embedded in the tiles, which collect scintillation light and transmit it to photomultiplier tubes. These particular tiles are made of Bicron BC408 scintillator and are used in HO.

0.087. Each of the 5 rings is 2.536 m long in the z -direction. Relative locations and general layout of the HO scintillation layers are shown in Figures 3.23 and 3.24, respectively.

The HE lies within the magnet coil at either end of the HB and just outside the electromagnetic calorimeter endcaps. The HE is separated from HB by a gap that does not align with the interaction point, so that the combination of the HB, HO, and HE completely enclose the interactions from the beam collisions and all the particles and hadronic jets they produce. For absorber material, HE uses the same C26000 cartridge brass that HB uses. The brass layers, normal to the z -direction, are 79 mm thick. There are 18 layers of absorber material in HE, which makes for about 10 interaction lengths when the electromagnetic calorimeter endcaps are included. The scintillator plates between the brass layers are 3 mm thick SCSN81 scintillators, and there is one additional 9 mm-thick layer of Bicron BC408 on the outside of the first layer. Like HB and HO, the scintillator plates have optical fibers that collect and transmit scintillator light to photomultiplier tubes. HE covers the pseudorapidity range $1.3 < |\eta| < 3$. HE has a granularity of $\Delta\eta \times \Delta\phi = 0.087 \times 0.087$ for $|\eta| < 1.6$, and $\Delta\eta \times \Delta\phi \approx 0.17 \times 0.17$ with $\Delta\eta$ ranging from 0.09 to 0.35 for $|\eta| > 1.6$. A diagram of HE is shown in Figure 3.25.

The HF is located on each end of the CMS cylinder, the front edge being 11.2 m from the interaction point. Figure 3.26 shows a diagram of HF on one end of CMS. As this is beyond the



Figure 3.22: ([23], 124) Photograph of one half of HB prior to installation. The absorber layers of brass are clearly visible, as well as the gaps between them that contain the scintillator plates.

ends of the solenoid magnet coil, it is not necessary to use non-magnetic absorber materials like it is for the other hadronic calorimeter sections. The HF is a Cherenkov detector. It is a cylinder that is divided into two symmetric segments on each side of the beamline, extending from an inner radius of 12.5 cm to an outer radius of 130 cm. It is constructed of 5 mm-thick steel plates that are diffusion-welded together. Each plate has a square grid of grooves over its area. The grooves are roughly square-shaped with sides of about 1 mm. The center of each groove is 5 mm away from the center of adjacent grooves in the square grid. When the plates are welded together, the grooves form spaces in the steel that run the length of the cylinder parallel to the beamline. Into these grooves are inserted quartz fibers with a fused-silica core and polymer-hard cladding, which constitute the dielectric material. The fibers have a diameter of 0.63 mm, where 0.6 mm is the fused-silica core and the rest is the polymer-hard cladding. Additionally, there is a protective

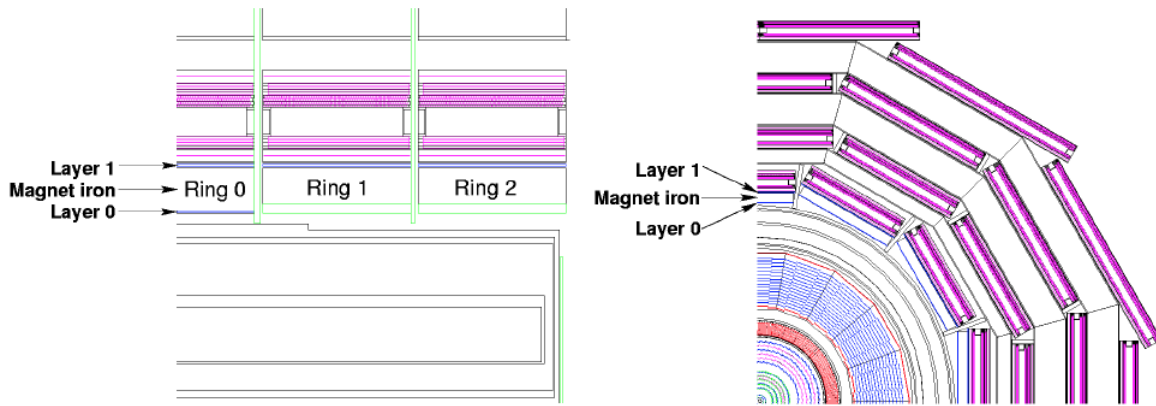


Figure 3.23: ([23], 138) Relative location of HO and its scintillator layers shown looking from the r-direction (left) and z-direction (right).

acrylate buffer layer that extends the diameter of the fiber structure in the grooves to 0.8 mm. The Cherenkov scintillation light from traversing particles is produced in the quartz fibers and travels along the fibers to connected light guides, which in turn are connected to photomultiplier tubes. The HF absorber area is 165 cm long, about 10 interaction lengths. There are two sets of quartz fibers, one of which runs the full length of HF and one of which does not run the length of the first 22 cm of the HF (i.e., 165 cm and 143 cm, respectively). Adjacent grooves alternate between containing long and short fibers. This arrangement of long and short fibers allows the signal from hadrons to be distinguished from that of electrons, positrons, and photons. The electrons, positrons, and photons deposit much of their energy in the first 22 cm of HF, while the hadrons produce nearly equal signals between the first 22 cm and the last 143 cm. Radiation shielding protects various components of HF outside of the absorber area due to the intensity of radiation in this region of CMS. HF covers the pseudorapidity range $2.866 < |\eta| < 5.205$ and has a granularity of about $\Delta\eta \times \Delta\phi = 0.175 \times 0.175$. The exceptions are the innermost segment where $\Delta\eta = 0.30$, the two innermost segments where $\Delta\phi \approx 0.35$, and the outermost segment where $\Delta\eta = 0.111$ (see Fig. 3.27). Figure 3.27 shows the segmentation of HF. Figure 3.28 shows a quarter view that includes all of the components of HCAL and displays their segmentation.

The hadronic calorimeter energy resolution is determined by examining jet transverse energy

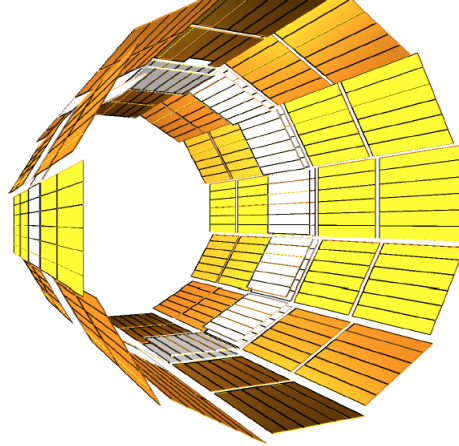


Figure 3.24: ([23], 142) Layout of HO scintillator layers is shown here. The central ring has two layers on each side of the iron frame it is mounted on, the other rings have one.

resolution and missing transverse energy resolution (transverse energy is the same thing as transverse mass, defined in Equation 2.81). The missing transverse energy refers to: (1) the momentum imbalance between the hadrons that the hadronic calorimeter measures, and (2) the initial momentum of the incoming particles that collide. The hadronic calorimeter cannot measure muons and neutrinos, as those particles are insensitive to the strong nuclear force and therefore deposit little, if any, energy in the absorber material. The energies of those particles the hadronic calorimeter cannot measure manifests as this missing transverse energy. The hadronic calorimeter jet transverse energy resolution is shown in Figure 3.29. The overall energy resolution of the hadronic calorimeter, combined with the electromagnetic calorimeter is expressed as [34]

$$\left(\frac{\sigma_E}{E}\right)^2 = \left(\frac{120\%}{\sqrt{E}}\right)^2 + (6.9\%)^2. \quad (3.9)$$

3.3.5 The Zero Degree Calorimeter

The Zero Degree Calorimeter (ZDC) consists of two identical Cherenkov detectors. Each one is respectively located on either end of the CMS detector at the points where the two LHC rings merge into a common beamline for the beams to undergo collisions in CMS [23]. This is about 140

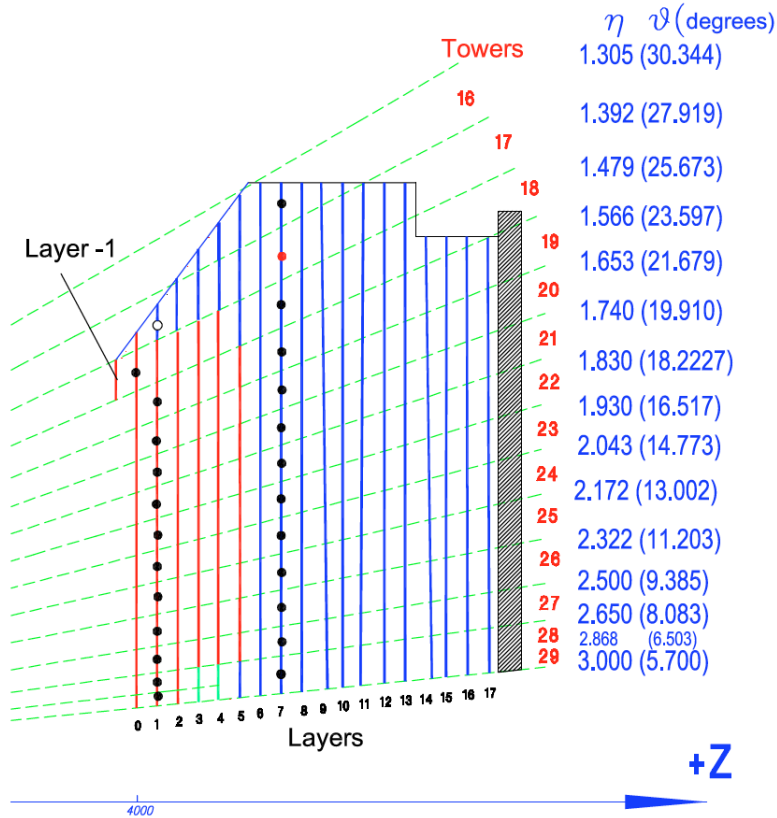


Figure 3.25: ([23], 137) Diagram of HE and its segmentation and geometry is shown here. The angles of the boundaries between the towers, shown as green dashed lines emanating from the interaction point, are given in units of pseudorapidity and degrees.

meters on each end from the interaction point, which is well outside the CMS cylinder complex and solenoid magnet. The principle purpose of the ZDC is to detect evidence of nuclear breakup in heavy ion collisions in CMS. Where the beamline separates back into two rings, neutral particles such as neutrons and photons emitted at very high pseudorapidities will not be steered by the magnets into the two separate rings. In a peripheral or an ultra-peripheral collision, the nuclides will undergo partial or total breakup, and the now free neutrons that previously were part of the nuclides will travel down the beamline until the beamline separates, at which point they strike the ZDC.

Each ZDC detector has two parts, an electromagnetic (EM) section and a hadronic (HAD) section. Photons interact with EM while hadrons interact with both EM and HAD. The EM section consists of 33 layers of 2 mm-thick tungsten plates interspersed with 33 layers of 0.7 mm diameter

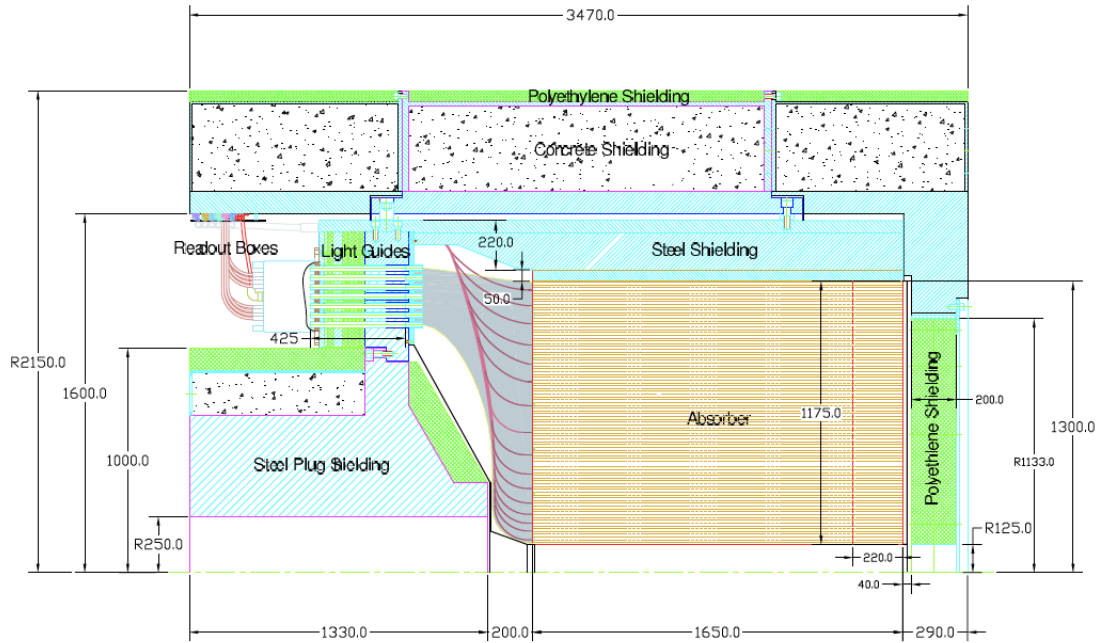


Figure 3.26: ([23], 147) Diagram of one end of HF is shown here. The absorber is the sensitive area of HF. Other components are protected by radiation shielding.

quartz fibers. The tungsten plates are oriented vertically and the quartz fibers are laid in ribbons. The HAD section consists of 24 layers of 15.5 mm thick tungsten plates interspersed with 24 layers of 0.7 mm diameter quartz fibers, which again are laid in ribbons. These plates and fibers are oriented 45° from the vertical. Overall, the ZDC EM and HAD sections combine for about 7.5 interaction lengths. The quartz fiber ribbons are grouped together to form readout bundles. In EM, there are five such bundles that are each connected directly to a photomultiplier tube. In HAD, there are four bundles, each consisting of six individual ribbons. Each bundle is connected to a light guide that carries the light to a photomultiplier tube. Each bundle in both EM and HAD forms a readout channel. The ZDC has a total of 18 readout channels, where there are five EM and four HAD channels in either ZDC detector. The ZDC covers a pseudorapidity range of $\eta \geq |8.3|$. Figure 3.30 shows a diagram of the ZDC and a photograph of HAD.

The energy resolution of the ZDC was measured with test beams consisting of electrons, positrons, pions, and muons. For different positron energies, the energy resolution is shown in

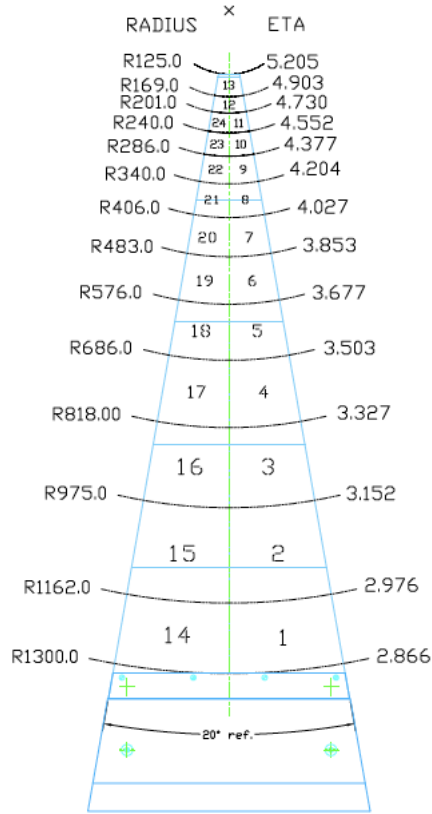


Figure 3.27: ([23], 148) Diagram of an HF segment is shown here. Rings and wedges define the pseudorapidity and azimuthal segmentation of HF, respectively. Ring radius and respective pseudorapidity values are shown. It can also be seen that the two innermost rings have an azimuthal angle of 20° (0.35 radians) instead of 10° (0.175 radians).

Figure 3.31 and can be expressed as

$$\left(\frac{\sigma}{E}\right)^2 = \left(\frac{70\%}{\sqrt{E}}\right)^2 + (8\%)^2 \quad (3.10)$$

where E is the energy in GeV. For pion energies, the resolution can be expressed as

$$\frac{\sigma}{E} = \frac{138\%}{\sqrt{E}} + 13\%. \quad (3.11)$$

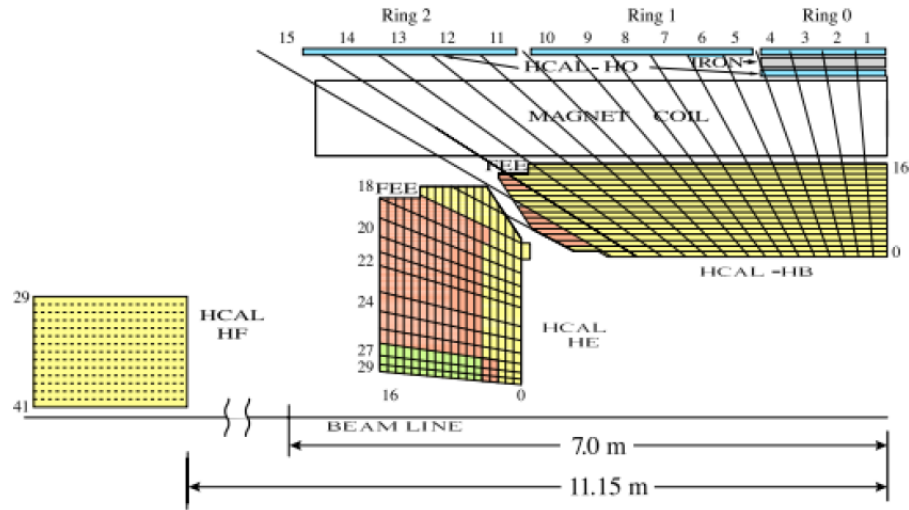


Figure 3.28: ([7]) A quarter view of HCAL and all of its components is shown here, along with the specific segmentation of each component.

3.3.6 CASTOR

CASTOR (Centauro and Strange Object Research) consists of two identical Cherenkov detectors in the very forward region on each side of the CMS detector (Figure 3.32). They are located 14.38 m from the interaction point [23] and cover the pseudorapidity ranges $5.2 < |\eta| < 6.6$. Like the ZDC, each CASTOR detector has an electromagnetic (EM) and hadronic (HAD) section. Both sections consist of layers of tungsten (W) absorber plates (density = 18.5 g/cm^3) interspersed with fused silica quartz plates (Q). The quartz plates are 2 mm and 4 mm thick in EM and HAD, respectively, while the tungsten plates in those sections are 5.0 mm and 10.0 mm thick, respectively. The layers are inclined from the beamline at 45° , forming a chevron-like structure that points toward the interaction point. The combination of one tungsten and one quartz plate is called a sampling unit (SU), and a group of five SUs forms one readout unit (RU). The light from an RU is transported by light guides to a photomultiplier tube (PMT). EM has two RUs, and HAD has 12. Each CASTOR detector has a total of 10 interaction lengths. Figure 3.33 shows a diagram of a CASTOR detector.

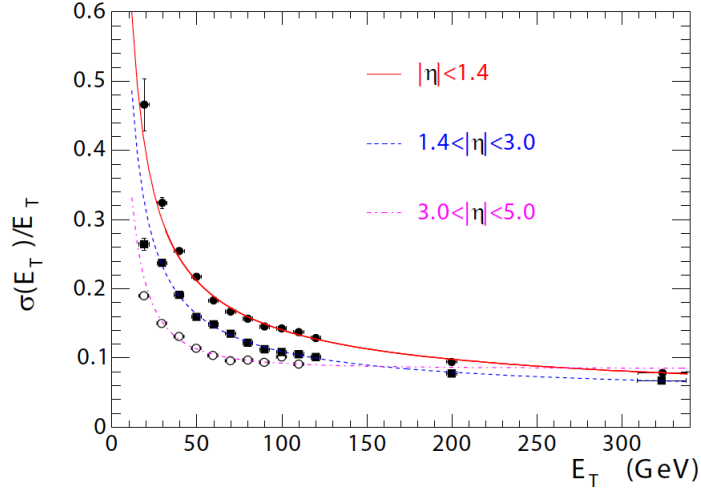


Figure 3.29: ([23], 5) Jet transverse energy resolution for the hadronic calorimeter is shown for the given pseudorapidity ranges, roughly corresponding to HB/HO, HE, and HF, respectively.

3.3.7 Muon Detector/Tracker System

CMS, as its name implies, was designed principally with the muon detector/tracker system in mind. The muon system measures the position and, in concert with the solenoidal magnetic field, the momentum of muons resulting from interactions in CMS. The muon system consists of three types of gas-filled chamber detector complexes: drift tube chambers (DT), cathode strip chambers (CSC), and resistive plate chambers (RPC) [11] [23] [7] [34]. The muon system covers the pseudorapidity ranges $|\eta| < 2.4$. The drift tubes make up a barrel region of the muon system that covers $|\eta| < 1.2$. The cathode strip chambers form an endcap region of the muon system that covers $0.9 < |\eta| < 2.4$. The resistive plate chambers fill a corner gap between the drift tubes and the cathode strip chambers, covering up to $|\eta| < 1.6$. These components of these three detector complexes are mounted to the wheels and disks of the barrel and endcap regions, respectively, of the steel skeleton (see Figure 3.12). Since the steel skeleton captures and channels the flux of the magnetic field outside of the solenoid coils, this provides a uniform magnetic field for the muon system components to measure muon momentum. A diagram of the muon system components appears in Figure 3.34.

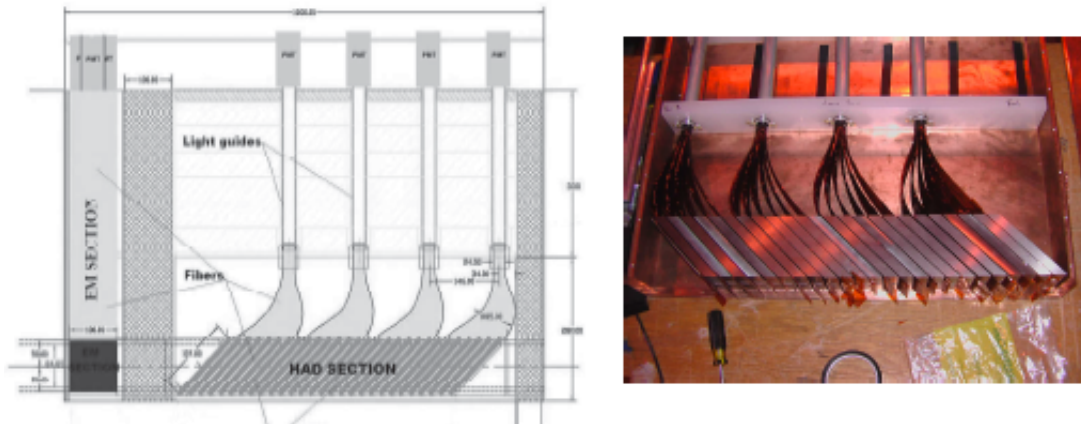


Figure 3.30: ([23], 159) On the left a diagram of the ZDC detector is shown. EM is at the far left. It is followed by HAD, whose 45° -angled alternating tungsten and quartz layers are clearly visible. Also visible are the 4 readout channels of HAD. A photograph of HAD is shown on the right.

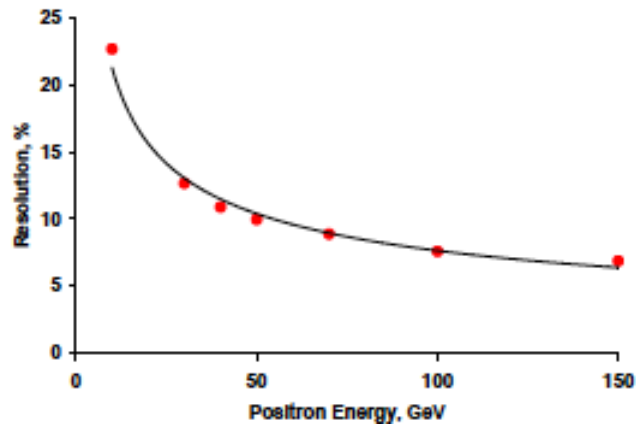


Figure 3.31: ([23], 161) ZDC energy resolution as a function of the positron test beam energy is shown here.

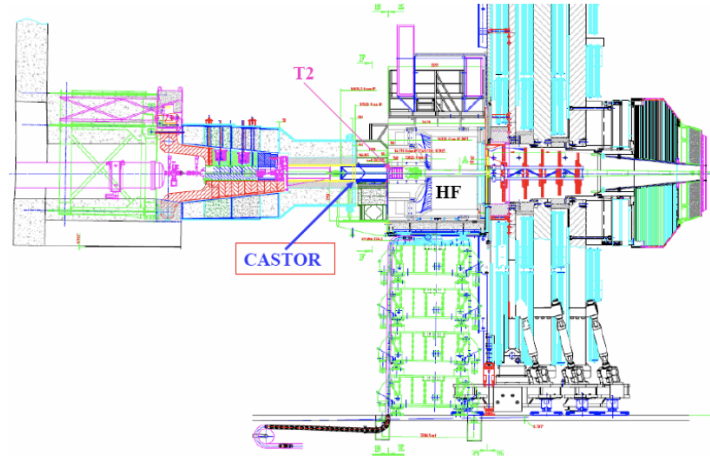


Figure 3.32: ([23], 157) Location of one CASTOR detector in CMS is shown here.

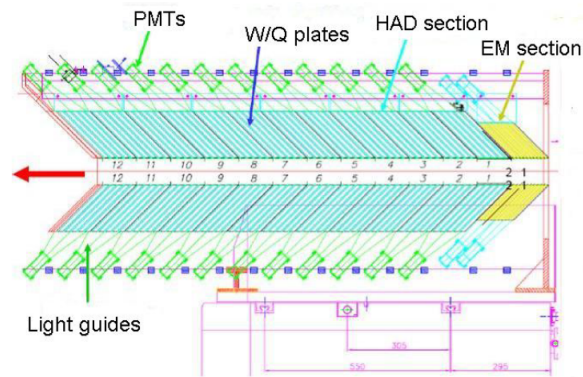


Figure 3.33: ([23], 158) Diagram of CASTOR and its components is shown here. The red arrow indicates the direction away from the interaction point from which particles emerge.

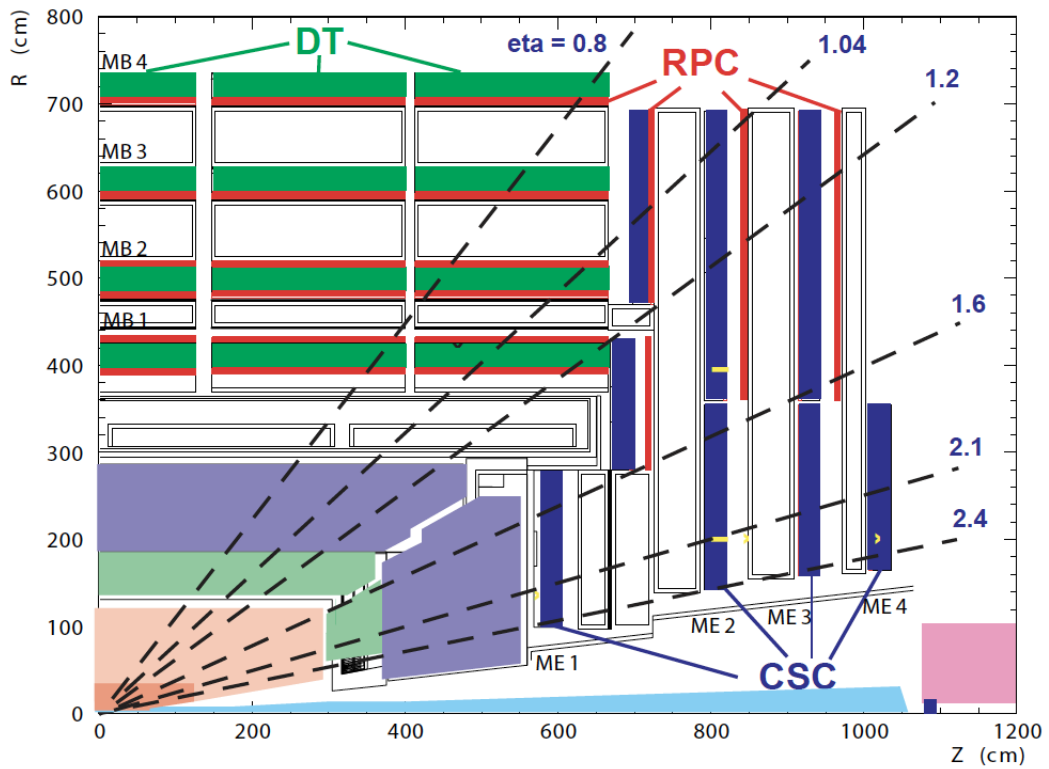


Figure 3.34: ([11], 12) Quarter diagram of the muon system is shown here.

Chapter 4

The Compact Muon Solenoid Experiment Part II: Analysis

Techniques

Chapter 3 was a description of the design principles and specifications of the CMS detector. This chapter describes how the CMS detector was utilized to detect and measure UPC dijets. Section 4.1 discusses how UPC dijet events were identified and selected from the 2015 CMS heavy ion data run. Section 4.2 describes the particle flow algorithm, which was used to identify and classify the particle detections that were used in this analysis. Section 4.3 describes the anti- k_T algorithm, which was used to identify the UPC dijets used in this analysis.

4.1 Triggering and Data Gathering

To record data in CMS, triggers must be used. A trigger is a system by which unwanted data is screened out and only useful data is recorded for analysis. This is necessary because the potential data stream from collisions/interactions in CMS is too large to be recorded in its entirety. There are about 10^9 interactions per second in CMS, yet only about 10^2 of those can be permanently recorded. CMS has hardware-based Level 1 Triggers, which use signals only from the calorimeters and muon detector, and software-based High Level Triggers to accomplish this.

For this analysis on UPC jets, an effective trigger needed to screen for and use the following characteristics of UPC jets:

- Two jets, i.e., dijets, in CMS;
- An imbalance of neutrons between ZDC+ and ZDC-; and

- A pseudorapidity gap, meaning there should be nothing in one HF calorimeter.

Although CMS does have dedicated jet triggers, it was decided not to use them because, while they work well for jets with high p_T , their efficiency falls off rapidly for jets with $p_T < 60$ GeV/c [16], where the great statistical majority of UPC jets are predicted to lie. Instead, it was decided to use a trigger that selects events meeting the following criteria:

- Electromagnetic calorimeter measures at least 5 GeV from a single particle hit (L1);
- Energy is measured exclusively in one HF calorimeter, not both (L1); and
- At least one 1 pixel track is measured (HLT).

The first criterion is what was utilized as a "jet trigger," since UPC jets are highly likely to deposit at least 5 GeV of energy in the electromagnetic calorimeter. The second criterion is indicative of a pseudorapidity gap. The third, which was an HLT trigger because tracks can only be reconstructed after tracker signals have been taken, was used because a UPC jet should have at least one charged hadron that leaves a track in the pixel detector. The ZDC was not used for triggering purposes but nonetheless served an important role in the subsequent analysis.

The data for this analysis was collected during the 2015 LHC Pb-Pb data run. This occurred from 16 November-13 December 2015. During this time, a total integrated luminosity of 0.404 nb^{-1} for the Pb-Pb beams was attained. The trigger used allowed an integrated luminosity of 0.38 nb^{-1} to be attained for this analysis. The Pb-Pb collisions had a collisional momentum per nucleon $\sqrt{s_{NN}} = 5.02 \text{ TeV}$.

4.2 The Particle Flow Algorithm

CMS identifies particles as well as missing energy by utilizing the subdetector systems, described in the previous chapter and shown again in Figure 4.1, in concert to classify the objects

¹nb is an abbreviation for nanobarn where $1 \text{ barn} \equiv 10^{-28} \text{ m}^2$. This is a unit of area that represents the probability that a subatomic collision or other reaction will happen.

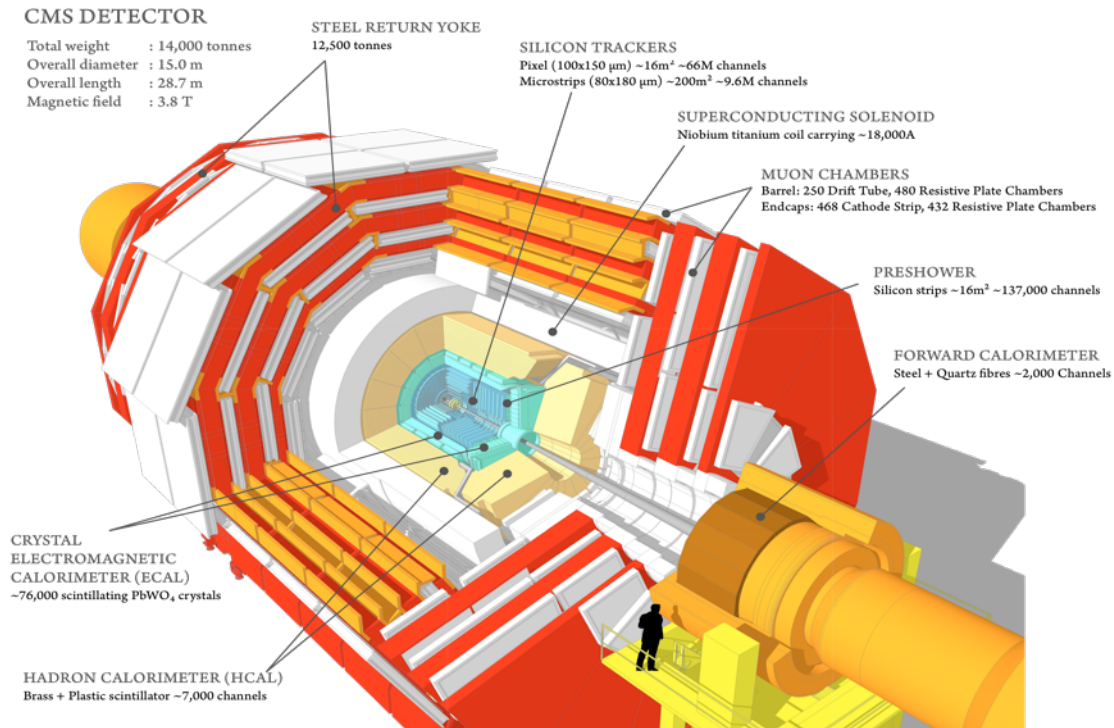


Figure 4.1: ([24]) A cutaway diagram of the CMS cylinder and its subsystems.

that they measure. There are five classes of particles that the particle flow algorithm will classify: muons, electrons/positrons, charged hadrons, neutral hadrons, and photons. Computer programs will sort through the data collected by all of the CMS subdetectors for a particular interaction event, account for the magnetic field present, and use this information to reconstruct the tracks and calorimeter hits of specific particles, which are then classified according to how they interact with the detector as a whole. The process is best summarized by Figure 4.2, and detailed explanations for each of the five classes of particles follow.

- **Muon:** A muon will leave tracks in the silicon tracker and will register in the chambers of the muon detector. A muon's track will have two radii of curvature, one in the silicon tracker and one in the muon detector, being that a muon is a charged particle traveling through the CMS magnetic field. The radii of curvature will be in opposite directions in the silicon tracker and the muon detector, as the former is inside the solenoid and the latter is outside (where the field is "captured" by the steel skeleton, to which the muon chambers are mounted). The

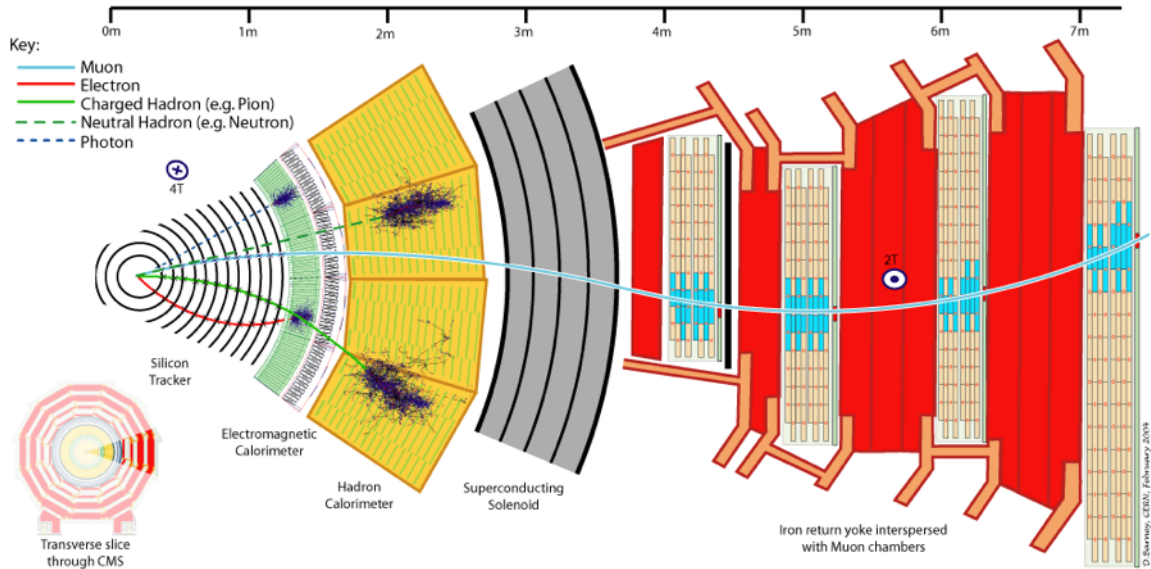


Figure 4.2: ([24]) A diagram of the CMS particle flow process.

radii of curvature are used to determine the charge and to calculate the spatial momentum vector of the muon. A muon detection is shown in blue in Figure 4.2.

- **Electron/Positron:** An electron or positron will register in the silicon tracker before depositing energy in the electromagnetic calorimeter. The electron or positron's track in the silicon tracker has a radius of curvature due to the magnetic field, and this is used to determine the charge, i.e., whether it is an electron or a positron, as well as its spatial momentum vector. The electromagnetic calorimeter then completely attenuates the electron or positron, yielding a measurement of its energy as well as a continued projection of its track. An electron/positron detection is shown in red in Figure 4.2.
- **Charged Hadron:** A charged hadron will register in the silicon tracker before depositing its energy in the hadronic calorimeter. The hadron's track in the silicon tracker has a radius of curvature due to the magnetic field, and this is used to determine the hadron's charge and spatial momentum vector. The hadronic calorimeter then completely attenuates the hadron, yielding a measurement of its energy and a continued projection of its track. A charged hadron detection is shown as a solid green line in Figure 4.2.

- Neutral Hadron: A neutral hadron will only register in the hadronic calorimeter, where it deposits its energy and yields an energy measurement. A directional track can be constructed based on the specific sections of the hadronic calorimeter where the neutral hadron's energy is deposited. A neutral hadron detection is shown as a dashed green line in Figure 4.2.
- Photon: A photon will primarily register in the electromagnetic calorimeter, where it deposits its energy and yields an energy measurement. A directional track can be constructed based on the specific sections of the electromagnetic calorimeter where the photon's energy is deposited. Since a photon has no mass, measuring its energy also yields its spatial momentum vector magnitude. A photon detection is shown as a dashed blue line in Figure 4.2.

To summarize, CMS can measure the spatial momentum of muons, electrons/positrons, charged hadrons, and photons; and it can measure the energy of electrons/positrons, charged hadrons, neutral hadrons, and photons. The particle flow algorithm utilizes the known value of muon mass to calculate muon energy. Strictly speaking, CMS is not able to measure the magnitude of neutral hadron spatial momentum. However, the energies of the already-known mass values of neutral hadrons that are long-lived enough to deposit their energy in the hadronic calorimeter are less than what the hadronic calorimeter can resolve, and neutral hadrons produced in interactions in CMS (along with all other massive particles produced in LHC interactions) are highly relativistic. Therefore, a measurement of neutral hadron energy effectively yields a measurement of neutral hadron spatial momentum magnitude. Using the combination of measurements and known data, the particle flow algorithm calculates the full momentum vector for all particles it measures.

One other important function of the particle flow algorithm is to calculate missing momentum and missing energy. CMS is designed to be a hermetically-sealed detector that completely encloses all the particles and radiation produced in the collision interactions. The input energy, spatial momentum, and momentum of the colliding protons or nuclides are known and all are conserved in the collisions. The particle flow algorithm sums up the total energy, spatial momentum, and momentum of the particles and radiation measured from the interactions and compares these sums to those of the pre-collisional protons or nuclides. An imbalance where the initial energy and

momentum differ from those of the final is missing momentum and missing energy, which is indicative of the production of particles that CMS cannot detect, such as neutrinos.

4.3 The Anti- k_T Algorithm

The particle flow algorithm identifies specific particles, but to identify hadronic jets another analysis method is needed to classify clusters of particles. CMS uses the anti- k_T jet-clustering algorithm for this purpose, k_T being transverse spatial momentum with respect to the beamline. The anti- k_T algorithm works as follows [15] [42]. An event with a few well-separated particles with relatively high k_T and many particles with relatively low k_T is considered. Two types of distances are defined, d_{ij} and d_{iB} . d_{ij} is the distance between two entities (particles or pseudojets) i and j , and d_{iB} is the distance between particle i and the beam ([15], 2). They are specifically defined as

$$d_{ij} = \frac{\min(1/k_{Ti}^2, 1/k_{Tj}^2)\Delta_{ij}^2}{R^2} \quad (4.1)$$

and

$$d_{iB} = \frac{1}{k_{Ti}^2}, \quad (4.2)$$

where

$$\Delta_{ij}^2 = (y_i - y_j)^2 + (\phi_i - \phi_j)^2. \quad (4.3)$$

y_i , and ϕ_i are, respectively, rapidity and azimuthal angle of entity i (similar for j). R , which is defined in the same y and ϕ coordinate system as Δ_{ij} , is the radius around a high k_T entity within which d_{ij} and d_{iB} are calculated. The smallest of these distances is identified. If the smallest distance is a d_{ij} , i and j are combined, that is, their momenta are summed. If the smallest distance is a d_{iB} , i is classified as a jet and removed from consideration. The process is repeated to find the next smallest distance for the remaining entities until all the entities being considered have been included in a jet cluster.

If a high k_T particle has no high k_T neighbors within a distance $2R$, all of the low k_T particles

within R of the high k_T particle are clustered into a perfectly conical jet. If there is another high k_T particle 2 where $R < \Delta_{12} < 2R$ from high k_T particle 1, there will be two jets, at least one of which will not be perfectly conical. If $\Delta_{12} < R$, both high k_T particles will be clustered into a single jet, which might or might not be perfectly conical. The key characteristic here is that relatively low k_T particles do not modify the shape of the jet but relatively high k_T particles do. Figure 4.3 shows an example of anti- k_T clustering results. For this UPC jet analysis, anti- k_T clustering with $R = 4$ was used.

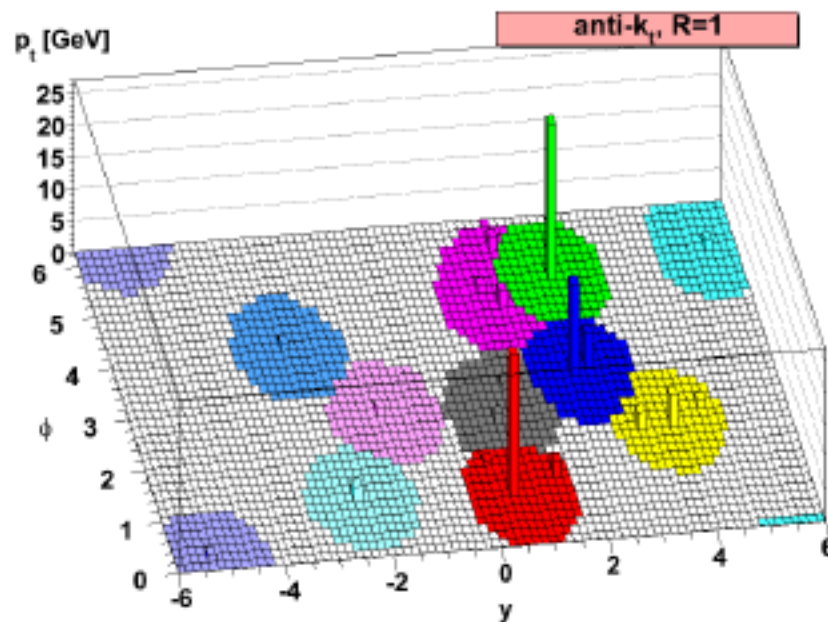


Figure 4.3: ([15], 4) A sample event where jets are identified with the anti- k_T algorithm. In this case, $R=1$. Some of the clusters here are random low k_T objects that might not be true jets. Notice how when two jet clusters overlap, which occurs when there are high k_T (p_T) particles within $R < \Delta_{12} < 2R$ of each other, the relative comparison of each particle's k_T determines how conical their respective jet clusters are.

Chapter 5

ZDC Calibration and Analysis

In order for the ZDC to be used for physics analysis, it first had to be properly calibrated for the 2015 LHC Pb-Pb heavy ion data run. This chapter provides a detailed description of the calibration process and presents the data that were used to undertake the calibration. The results of this calibration were then used in some of the data analyses detailed in Chapter 6.

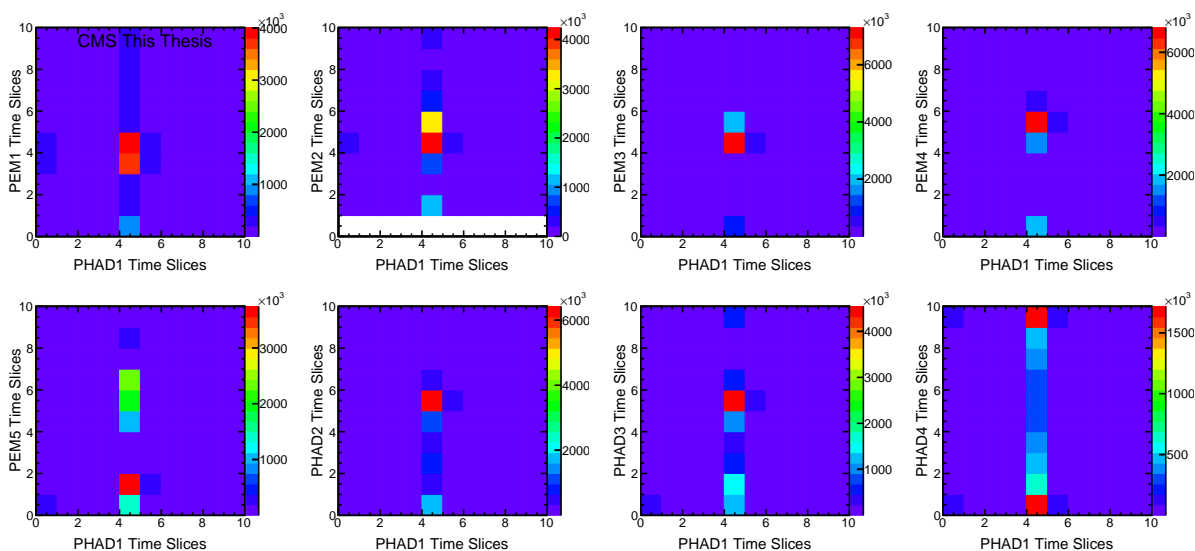


Figure 5.1: Time slice signals compared between ZDC+ HAD1 and all other readout channels on ZDC+.

The first step in the ZDC calibration process was to determine the time slices in which the principal signal lay. The ZDC detector signal is divided into 10 time segments, or time slices. In order to determine the time slice(s) that contained the signal of interest for the UPC jet analysis, as opposed to detector noise, time slices in readout channels 1-5 of both the ZDC+ and ZDC- EM sections and readout channels 2-4 of the ZDC+ and ZDC- HAD sections were compared,

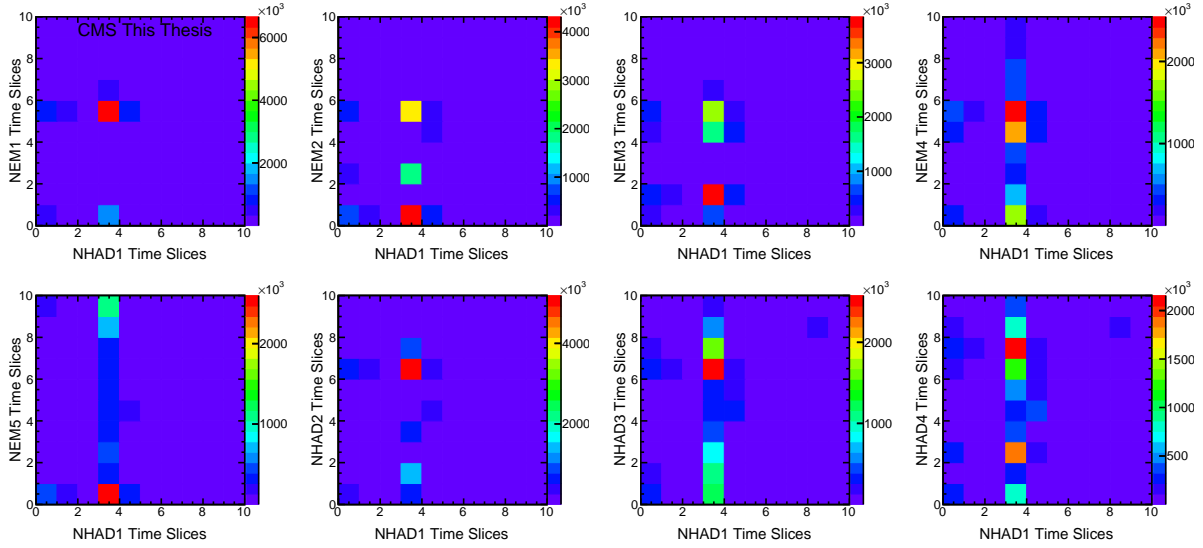


Figure 5.2: Time slice signals compared between ZDC- HAD1 and all other readout channels on ZDC-.

respectively, with the time slices in ZDC+ HAD1 and ZDC- HAD1 readout channels. The data used for this was minimum bias data from the CMS 2015 PbPb data run at all centralities, which used calibration settings from the 2010 LHC Pb-Pb data run. Minimum bias data is data that are taken with minimal trigger criteria – it can be thought of as a representative sample of the results of all interactions in CMS; and centrality is a measurement of the portions of each heavy nuclide that are directly involved in the collision with the other nuclide. To perform the time slice comparisons, the time slice containing the maximum signal for each readout channel in each event in the utilized minimum bias data was determined. The number of maximum signals in each time slice in each readout channel was tallied. These tallies were subsequently plotted in the form of two-dimensional histograms that compared all ten time slices of one selected readout channel to all ten time slices of another selected readout channel. Figures 5.1 and 5.2 show these histograms/comparisons. Based on these results, the time slices evaluated to contain the primary signal for calibration purposes are shown in Table 5.1. Additionally, time slices evaluated to almost solely contain electronic noise, which needed to be subtracted from the ZDC readout channel signal in the data analysis, were determined based on the information in Figures 5.1 and 5.2 and are also

Table 5.1: ZDC Time Slices with Signal, shown in descending order with strongest signal listed first.

Readout Channel	Time Slices with Signal	Time Slices Representative of Noise
ZDC+ EM1	4, 3	7
ZDC+ EM2	4, 5	8
ZDC+ EM3	4	7
ZDC+ EM4	5	7
ZDC+ EM5	1	7
ZDC+ HAD1	4	7
ZDC+ HAD2	5	7
ZDC+ HAD3	5	7
ZDC+ HAD4	0, 9	6
ZDC- EM1	5	7
ZDC- EM2	0	7
ZDC- EM3	1	7
ZDC- EM4	5, 4	8
ZDC- EM5	0	7
ZDC- HAD1	3	7
ZDC- HAD2	6	9
ZDC- HAD3	6, 7	9
ZDC- HAD4	7, 6	9

shown in Table 5.1.

After determining which time slices contained signal and which time slices were representative of electronic noise in the ZDC, the next step was to determine calibration constants for the readout channels of ZDC-. To do this, the same sample of minimum bias data, this time considering only those time slices containing the signal, was used to plot the following ZDC- readout channel ratios: $EM1+EM5/EM3$, $EM2+EM4/EM3$, $HAD2/HAD1$, $HAD3/HAD1$, and $HAD4/HAD1$. These ratios are shown in Figure 5.3. These ratios were then compared to the same ratios from the 2010 LHC Pb-Pb heavy ion data run. The 2010 data was used as a standard for calibration because that was when the ZDC was newly commissioned, and it has since accumulated radiation damage. The 2010 ZDC- readout channel ratios for $EM1+EM5/EM3$, $EM2+EM4/EM3$, $HAD2/HAD1$, $HAD3/HAD1$, and $HAD4/HAD1$ are shown in Figure 5.4. The key item of interest

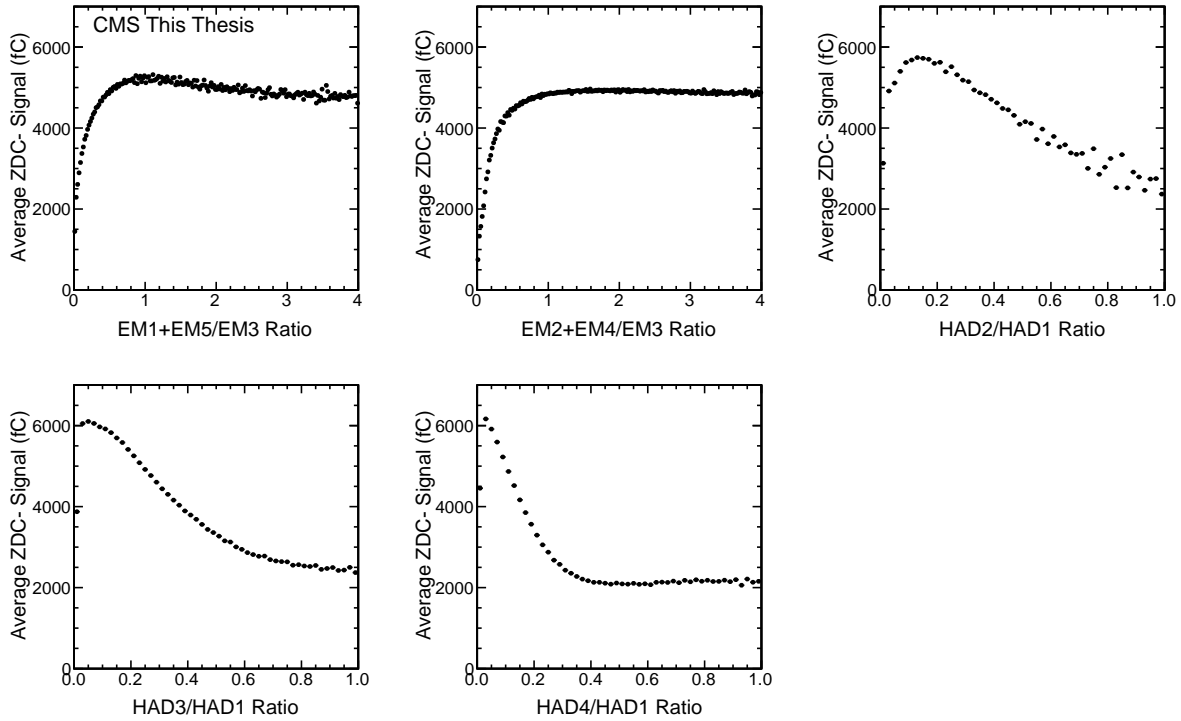


Figure 5.3: Average signal in femtocoulombs (fC) for the ZDC- signal ratios EM1+EM5/EM3, EM2+EM4/EM3, HAD2/HAD1, HAD3/HAD1, and HAD4/HAD1, respectively.

in each of the 2015 and 2010 ZDC- ratio plots shown in Figures 5.3 and 5.4 is the peak ratio, which was read upon magnification and close examination of each of these plots. The 2010 peak ratio for each plot was then divided by the corresponding 2015 peak ratio. This result was multiplied by the 2010 ZDC- readout channel calibration constants in order to arrive at the 2015 ZDC- readout channel calibration constants. These results are shown in Tables 5.2 and 5.3.

ZDC+ calibration constants were measured next. The first step in this process was to find the signal ratio as a function of centrality of each readout channel of ZDC+ to their ZDC- counterparts and fit them with a zero-order polynomial average. This was done after having applied the 2015 ZDC- calibration constants listed in Table 5.3 and using the 2015 minimum bias data used in the previous steps. These are shown in Figure 5.5. To properly calibrate the ZDC+ readout channels, calibration constants that would make the ZDC+/ZDC- signal ratio as a function of centrality approximately equal to 1 needed to be set, in order to ensure that identical particles of equal energy

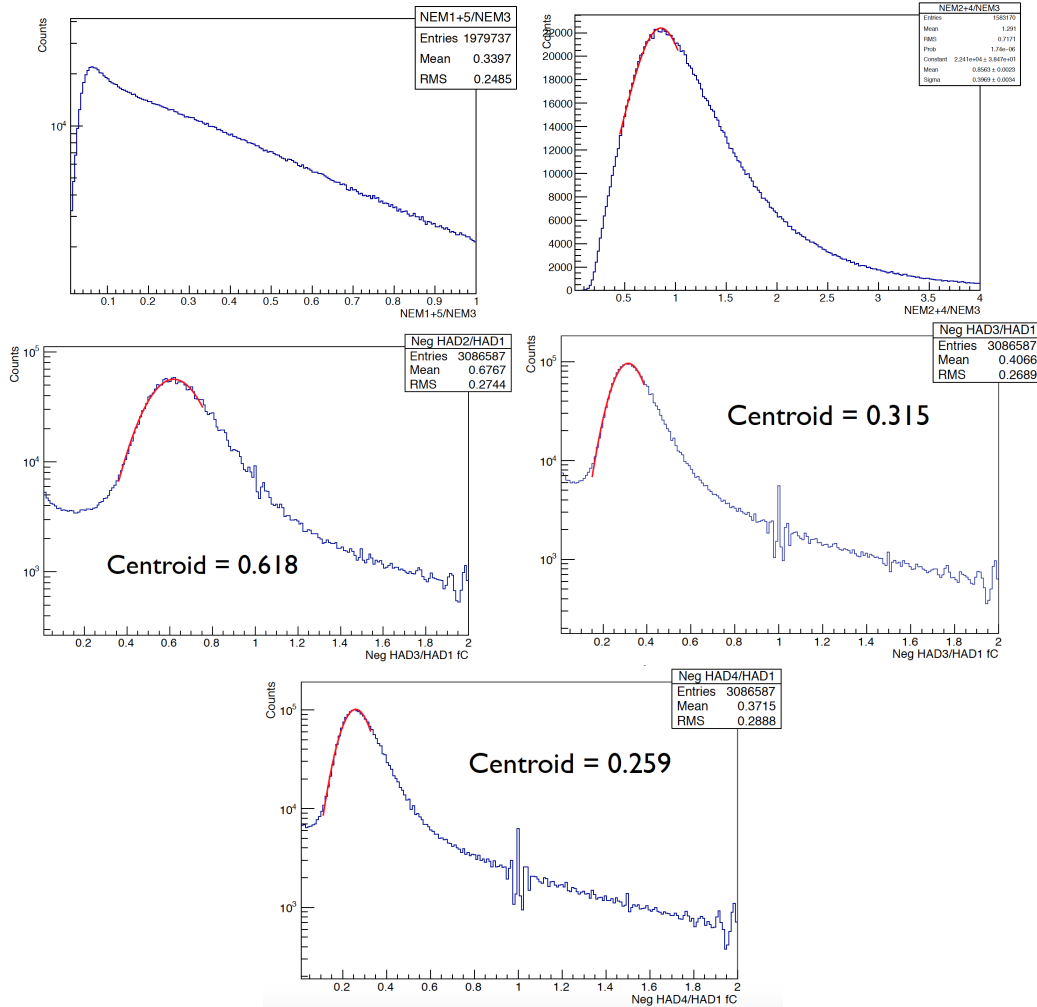


Figure 5.4: (Courtesy of Alice Mignerey) Average signal in femtocoulombs (labeled as counts on the y-axes) for the ZDC- signal ratios EM1+EM5/EM3, EM2+EM4/EM3, HAD2/HAD1, HAD3/HAD1, and HAD4/HAD1, respectively for 2010 LHC Pb-Pb heavy ion data.

and momentum interacting with either ZDC+ or ZDC- would generate a signal with equal strength in each one. To do this, the existing 2010 ZDC+ calibration constants, all equal to 1, were divided by the p_0 value for each readout channel shown in Figure 5.5. Table 5.4 shows these results.

After applying these calibration constants to their respective ZDC+ readout channels, the signal ratio as a function of centrality of each readout channel of ZDC+ to ZDC- was plotted again, shown in Figure 5.6. The average value p_0 was closer to 1 for each readout channel with these new ZDC+ calibration constants. To get them even closer to 1, an adjustment of the ZDC+ calibration constants was performed by repeating the same procedure that was used to find the ZDC+

Table 5.2: ZDC- Peak Ratios

Readout Channel Ratio	2010 Peak Ratio (from Figure 5.4)	2015 Peak Ratio (from Figure 5.3)	Calibration Factor (= 2010 Peak Ratio \div 2015 Peak Ratio)
EM1+EM5/EM3	0.062	1.09	0.057
EM2+EM4/EM3	0.85	1.75	0.486
HAD2/HAD1	0.618	0.13	4.754
HAD3/HAD1	0.315	0.0499	6.313
HAD4/HAD1	0.259	0.0301	8.605

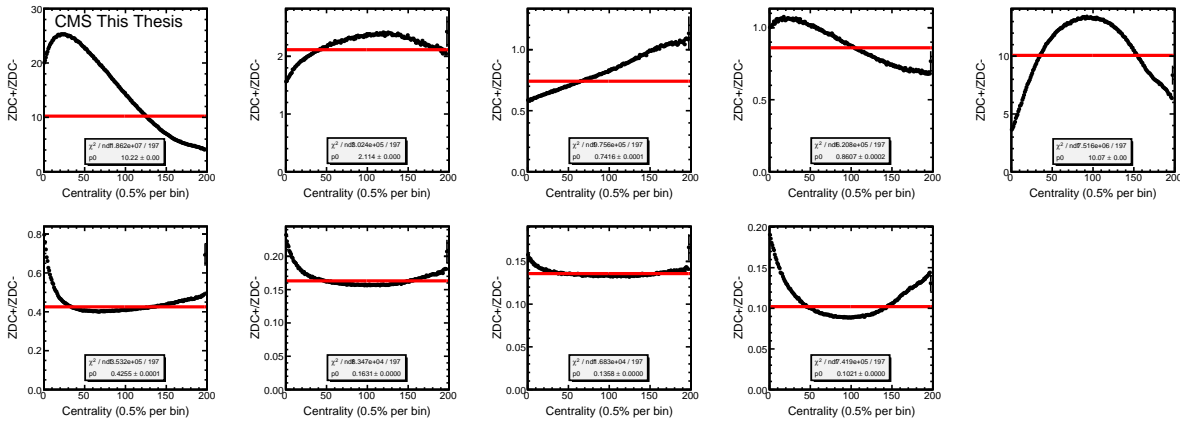


Figure 5.5: ZDC+/ZDC- signal ratio vs. centrality for each readout channel of ZDC+ to their ZDC- counterparts. The red lines are the zero-order polynomial average for each readout channel ratio, the value of which is labeled in each grey box as "p0".

calibration constants listed in Table 5.4. These adjustments are shown in Table 5.5.

After applying the final ZDC+ calibration constants to their respective ZDC+ readout channels listed in Table 5.5, the signal ratio as a function of centrality of each readout channel of ZDC+ to ZDC- was once again plotted. These are shown in Figure 5.7.

With the calibration constants determined, the next step was to examine the ZDC signal in the UPC data. The specific characteristics of this data will be further detailed in Chapters 6 and 7, but for now it is necessary to know that the data for each UPC event included both the data run number and the ZDC signal. It should be noted that the ZDC signal, for both ZDC+ and ZDC-, refers to

Table 5.3: 2015 ZDC- Readout Channel Calibration Constants

ZDC- Readout Channel	Calibration Factor (from Table 5.2)	2010 Calibration Constant	2015 Calibration Constant (=Calibration Factor*2010 Calibration Constant)
EM1	0.057	0.33	0.019
EM2	0.486	0.474	0.23
EM3	1 (calibration reference)	1.875	1.875
EM4	0.486	1.5	0.729
EM5	0.057	1	0.057
HAD1	1 (calibration reference)	0.417	0.417
HAD2	4.754	1.67	7.939
HAD3	6.313	1.68	10.605
HAD4	8.605	1	8.605

net ZDC signal:

$$\begin{aligned}
 \text{ZDC+ Signal} &= (0.1 \times \text{ZDC+ EM Signal} + \text{ZDC+ HAD Signal}) \\
 &\quad - (0.1 \times \text{ZDC+ EM Noise} + \text{ZDC+ HAD Noise}) \\
 \text{ZDC- Signal} &= (0.1 \times \text{ZDC- EM Signal} + \text{ZDC- HAD Signal}) \\
 &\quad - (0.1 \times \text{ZDC- EM Noise} + \text{ZDC- HAD Noise})
 \end{aligned} \tag{5.1}$$

where ZDC+ EM Signal and ZDC- EM Signal are the sums of the respective ZDC+ and ZDC- EM readout channels containing only the time slices with signal as listed in Table 5.1, ZDC+ HAD Signal and ZDC- HAD Signal are the sums of the respective ZDC+ and ZDC- HAD readout channels containing only the time slices with signal as listed in Table 5.1, ZDC+ EM Noise and ZDC- EM Noise are the sums of the respective ZDC+ and ZDC- readout channels containing only the time slices with noise as listed in Table 5.1, and ZDC+ HAD Noise and ZDC- HAD Noise are the sums of the respective ZDC+ and ZDC- readout channels containing only the time slices with

Table 5.4: Initial 2015 ZDC+ Readout Channel Calibration Constants

ZDC+ Readout Channel	p0	2010 Calibration Constant	2015 Calibration Constant (=2010 Calibration Constant/p0)
EM1	9.143	1	0.098
EM2	0.7427	1	0.473
EM3	0.3502	1	1.348
EM4	2.161	1	1.162
EM5	5.101	1	0.099
HAD1	0.4255	1	2.35
HAD2	0.1631	1	6.131
HAD3	0.1358	1	7.364
HAD4	0.1221	1	9.794

noise as listed in Table 5.1. Since the energy deposited in one ZDC end over an extended period of data taking is proportional to the energy deposited in the corresponding HF end, the average UPC ZDC event signal for each event as a function of the run number was examined where the energy deposited in HF+ was > 5 GeV and HF- was < 5 GeV, along with the opposite situation where HF- was > 5 GeV and HF+ was < 5 GeV. In the former situation, it was the ZDC+ signal that was examined, and in the latter, it was ZDC-. These are shown in the top row of Figure 5.8. From these plots, it is evident that there are three general groupings of data runs for both the ZDC+ and ZDC- signals. A zero-order polynomial (p_0) average of each of these three groups was taken for both ZDC+ and ZDC-, and the specifics of these averages are given in Table 5.6.

Given the proportionality between the ZDC and the HF mentioned above, these p_0 averages could be and were used to perform a further calibration on the ZDC. This calibration was based on weighted averages, which are given by

$$a = \frac{w_1 a_1 + w_2 a_2}{w_1 + w_2} \quad (5.2)$$

where a is the weighted average, a_1 and a_2 are quantities being averaged together (in this case they

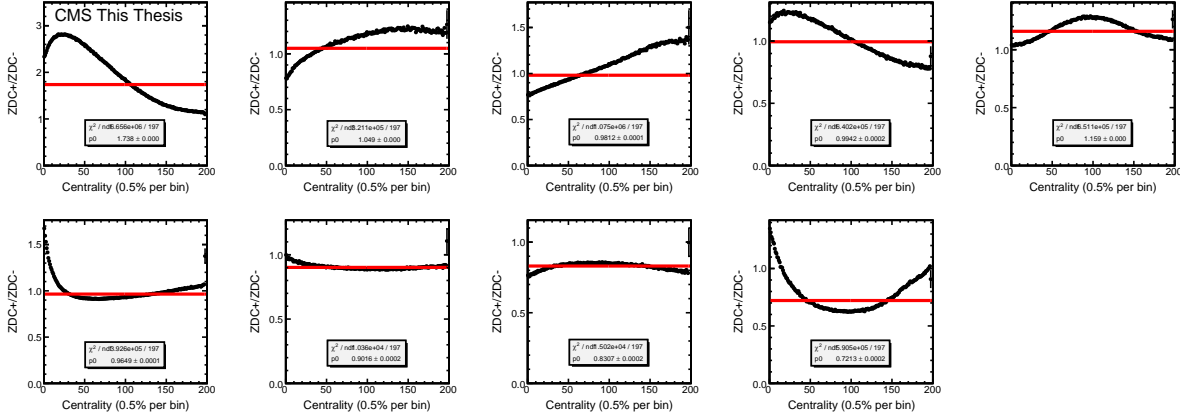


Figure 5.6: ZDC+/ZDC- signal ratio vs. centrality for each readout channel of ZDC+ to their ZDC- counterparts following application of calibration constants for ZDC+ channels listed in Table 5.4.

are p_0 averages of ZDC+ or ZDC- signals that are shown in the top row of Figure 5.8 and given in Table 5.6), and

$$w_1 = \frac{1}{\sigma_1^2}, w_2 = \frac{1}{\sigma_2^2}, \quad (5.3)$$

with σ_1 and σ_2 being the uncertainty associated with a_1 and a_2 (these are also given in Table 5.6 for each p_0). The basic procedure was to find the weighted average of the p_0 s for the two later data run groupings, since they tended to have similar values for both ZDC+ and ZDC-. With this, a correction factor was then found for each p_0 :

$$p_0 \times \text{correction factor} = a \text{ of later two } p_0\text{s}. \quad (5.4)$$

The weighted averages used and the correction factors are also shown in Table 5.6. The correction factors were multiplied by their respective ZDC signals for the respective run numbers of those signals, and the average ZDC signals as a function of run number, as shown in the top row of Figure 5.8, were plotted again. This is shown in the second row of Figure 5.8. The p_0 averages from these are listed in Table 5.7. While the p_0 averages of each of the three groups of data runs for ZDC+ and ZDC- were now considerably closer, it was evident that further corrections were required to make them even.

Table 5.5: Final 2015 ZDC+ Readout Channel Calibration Constants

ZDC+ Readout Channel	p0	Initial 2015 Calibration Constant	Final 2015 Calibration Constant (= Initial 2015 Calibration Constant/p0)
EM1	1.738	0.098	0.056
EM2	1.049	0.473	0.451
EM3	0.9812	1.348	1.374
EM4	0.9942	1.162	1.169
EM5	1.159	0.099	0.085
HAD1	0.9649	2.35	2.435
HAD2	0.9016	6.131	6.8
HAD3	0.8307	7.364	8.865
HAD4	0.7213	9.794	13.578

It turned out that the weighted averages procedure needed to be repeated again, followed by an additional adjustment to bring the p0s for ZDC+ up to these of ZDC-, which were at a consistently higher signal. The first correction factor adjustments used in the second iteration of the weighted average procedure, which were multiplied by the respective correction factors in Table 5.6, are listed in Table 5.7, as are the weighted averages used in this second iteration. The results of the second iteration are shown in the third row of Figure 5.8. The p0 averages that resulted from the second iteration as well as the second correction factor adjustments for ZDC+ used in the additional adjustment (multiplied by the respective correction factor and correction factor adjustments in Tables 5.6 and 5.7) are listed in Table 5.8. The additional adjustment required no new weighted average, since all of the p0s of both ZDC+ and ZDC- were within their respective uncertainty margins. The final p0 averages that resulted from the additional adjustment are listed in Table 5.9. Also listed in Table 5.9 are the final correction factors, which are the respective products of the correction factors and correction factor adjustments in Tables 5.6, 5.7, and 5.8. These were multiplied by their respective ZDC signals for the respective run numbers of those signals to arrive at the final calibrated ZDC signals, which are shown in the bottom row of Figure 5.8.

The final step in ZDC calibration was to review the ZDC signal distributions for both ZDC+

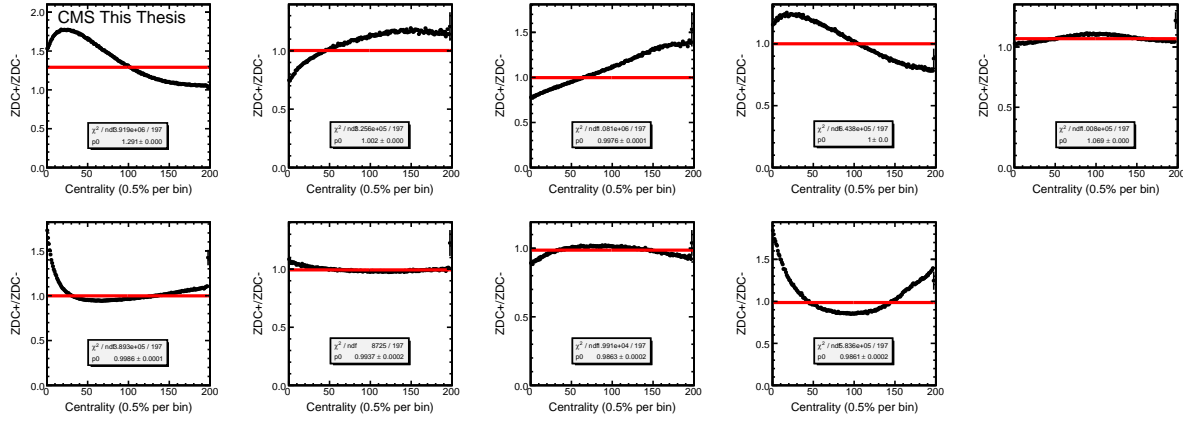


Figure 5.7: ZDC+/ZDC- signal ratio vs. centrality for each readout channel of ZDC+ to their ZDC- counterparts following application of the final calibration constants for ZDC+ channels listed in Table 5.5.

Table 5.6: Average ZDC Signals for Run Number Groups in the first two plots of the top row of Figure 5.8 and Initial Correction Factors

ZDC End	Run Number Range	p0 Average (fC)	a (fC)	Correction Factor
ZDC+	262600-262800	2367.74±48.9039	4124.198697	1.741829211
ZDC+	262801-263134	4116.28±37.1823	4124.198697	1.001923751
ZDC+	263135-263630	4126.54±20.218	4124.198697	0.9994326232
ZDC-	262600-262830	4109.54±59.5661	4302.897463	1.047050877
ZDC-	262831-263132	4370.75±47.6319	4302.897463	0.984475768
ZDC-	263133-263630	4287.75±22.5053	4302.897463	1.00353273

and ZDC- in the UPC jet data. This distribution is shown in Figure 5.9. The signals have similar distributions along each axis, which was to be expected. This completed the ZDC calibration, and the ZDC was now ready to be used for physics analyses.

Table 5.7: Average ZDC Signals for Run Number Groups for the second two plots in the top row in Figure 5.8 and First Correction Factor Adjustments

ZDC End	Run Number Range	p0 Average (fC)	a (fC)	Correction Factor Adjustment
ZDC+	262600-262800	4006.85±84.9412	4108.333332	1.02532746
ZDC+	262801-263134	4109.73±40.4	4108.333332	0.9996601558
ZDC+	263135-263630	4107.92±21.9778	4108.333332	1.000100618
ZDC-	262600-262830	4292.44±67.04	4285.5170337	0.9983871723
ZDC-	262831-263132	4273.1±50.5843	4285.5170337	1.002905861
ZDC-	263133-263630	4288.43±24.4989	4285.5170337	0.9993207383

Table 5.8: Average ZDC Signals for Run Number Groups for the first two plots in the bottom row in Figure 5.8 and Second Correction Factor Adjustments

ZDC End	Run Number Range	p0 Average	Correction Factor Adjustment
ZDC+	262600-262800	4108.33±87.0926	1.043348514
ZDC+	262801-263134	4108.34±40.3863	1.043348514
ZDC+	263135-263630	4108.33±21.98	1.043348514
ZDC-	262600-262830	4285.52±66.9319	1
ZDC-	262831-263132	4285.52±50.7313	1
ZDC-	263133-263630	4286.42±24.4969	1

Table 5.9: Average ZDC Signals for Run Number Groups for the Final Two Plots in the Bottom Row in Figure 5.8 and Final Correction Factors Applied

ZDC End	Run Number Range	p0 Average	Final Correction Factor
ZDC+	262600-262800	4286.42±90.8679	1.863363396
ZDC+	262801-263134	4275.98±41.8447	1.045000399
ZDC+	263135-263630	4277.77±22.7855	1.042861462
ZDC-	262600-262830	4285.52±50.7313	1.045362164
ZDC-	262831-263132	4285.52±50.7313	0.9873365177
ZDC-	263133-263630	4286.42±24.4969	1.002851069

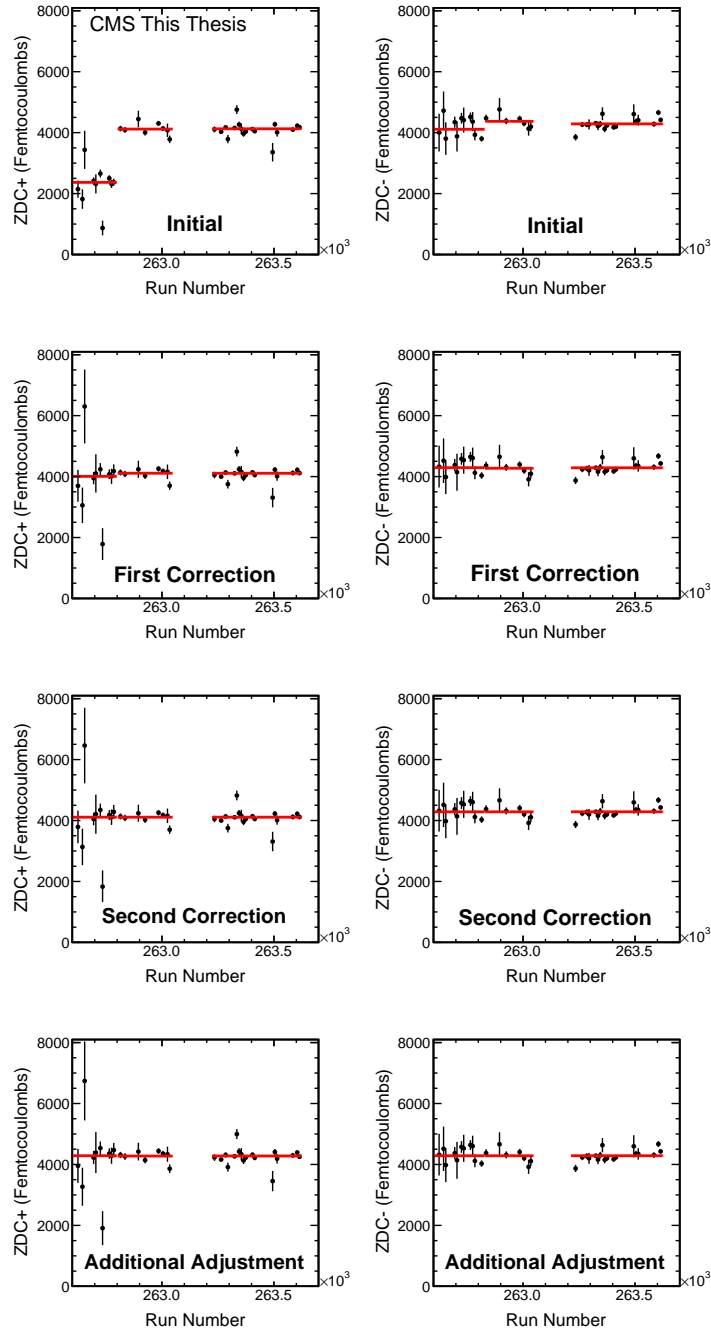


Figure 5.8: Average ZDC signal per event vs. data run number in the 2015 CMS LHC heavy ion run data run is shown here, with ZDC+ signal where HF+ was > 5 GeV and HF- was < 5 GeV in the first column, and ZDC- signal where the energy deposited in HF- was > 5 GeV and HF+ was < 5 GeV in the second column. In the top row, the p_0 averages for three groups of data runs show consistent differences in the ZDC signal strength in each of these groups on both ZDC+ and ZDC-, particularly with the earliest group. In the second row, the correction factors listed in Table 5.6 have been applied. The p_0 averages here for the three groups are considerably closer, but more corrections were clearly required. Another iteration of corrections plus an additional adjustment to equalize ZDC+ and ZDC- were performed, with their results shown in the third and fourth rows, respectively.

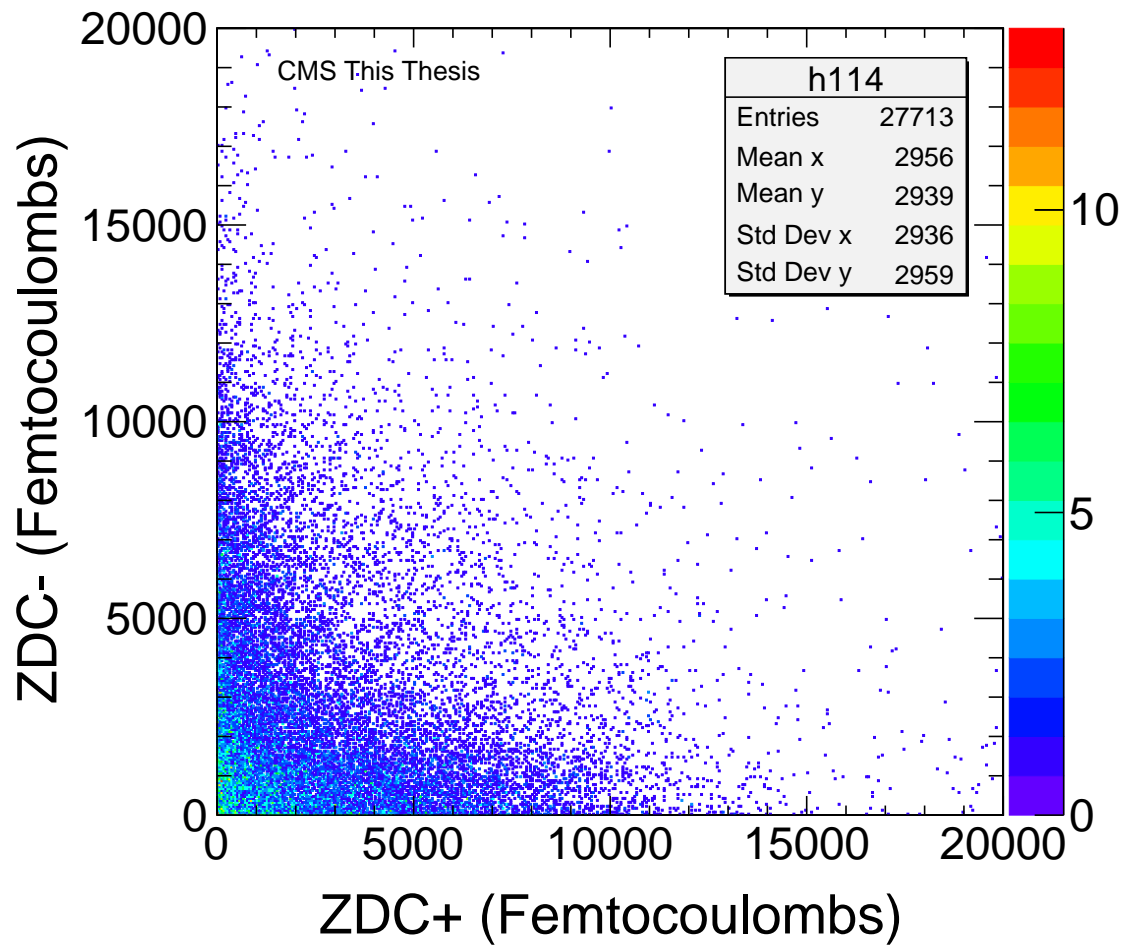


Figure 5.9: ZDC- signal versus ZDC+ signal in UPC jet data. Very low energies for both ZDC+ and ZDC- are consistent with exclusive-type processes.

Chapter 6

Data Analysis

This chapter provides a detailed analysis of the UPC dijet data that were used to arrive at the results presented in Chapter 7. Section 6.1 describes how the jet energy resolution for the CMS data being analyzed was checked. Section 6.2 details the telltale indications that UPC dijets were in fact selected and observed. Section 6.3 defines the pseudorapidity gap that was used in this analysis. Section 6.4 details the principle component of this analysis, the azimuthal correlation analysis between UPC dijets.

6.1 Checking the Jet Energy Scale

UPC jets tend to have energies that are typically about an order of magnitude lower than the hadronic jets that CMS typically measures. For the very low energies typical of UPC events, it is possible that the CMS energy scale depends upon pseudorapidity. To check this effect a tag and probe technique was developed.

The tag and probe procedure worked as follows. Events considered were those passing the UPC trigger that had exactly two jets, a difference in azimuthal angle of at least 0.25 radians, and an average p_T of 15 GeV or greater. The jet energy scale is most reliable at $\eta=0$. Therefore any jet with $|\eta| < 0.3$ was called a probe, and the other jet was designated as the tag. If both jets have $|\eta| < 0.3$ then they are each both tags and probes. For each event the ratio $\frac{p_{T,probe}}{p_{T,tag}}$ was calculated. The pseudorapidity of the probe jet vs. the average of this ratio for that particular pseudorapidity was then plotted. This is shown on the left side of Figure 6.1.

After this, the specific contents of the plot on the left side of Figure 6.1 were used as a correction

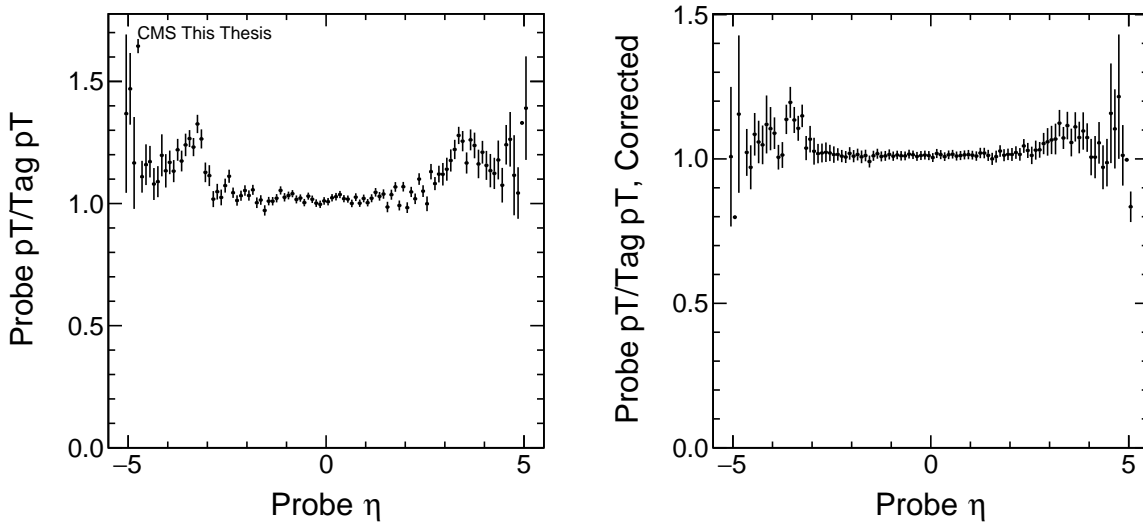


Figure 6.1: Probe jet pseudorapidity η vs. $\frac{p_{T,probe}}{p_{T,tag}}$ are shown here uncorrected (left) and corrected (right). $\frac{p_{T,probe}}{p_{T,tag}}$ is at or close to unity where $|\eta| < 3$.

factor for the p_T of each jet in each UPC event. To do this, the p_T of a particular jet in an event was divided by the ratio $p_{T,probe}/p_{T,tag}$ at the probe jet pseudorapidity in the left plot of Figure 6.1. This was done for the p_T values in all jets for all UPC events that passed the trigger. The tag and probe procedure described in the previous paragraph was then repeated. The results are shown in the plot on the right side of Figure 6.1.

Figure 6.1 reveals that the ratio $p_{T,probe}/p_{T,tag}$ is equal to or nearly equal to 1 where $|\eta| < 3$, demonstrating that the jet energy scale was independent of η for those ranges of η .

6.2 Selecting Exclusive UPC Dijets

The characteristics of UPC dijets that were listed in Chapter 4.1 were:

- Two jets, i.e. dijets, in CMS (that are back to back in azimuth);
- An imbalance of neutrons between the two ZDC ends; and
- A pseudorapidity gap (more on this in Section 6.3).

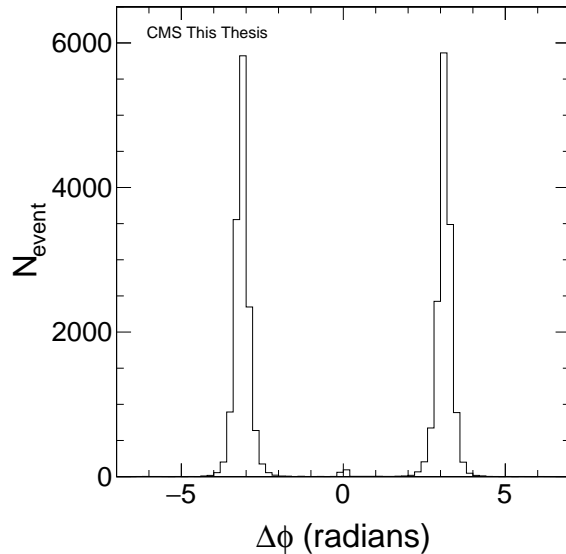


Figure 6.2: Difference of azimuthal angle ϕ in the lab frame between the leading and subleading jets ($\phi_{leading} - \phi_{subleading} = \Delta\phi$) in each dijet event, before the application of the cut of $|\Delta\phi| = 2$ radians. The dijets generally have a difference of π radians. The presence of a small sample that had a difference of about 0 radians necessitated the $|\Delta\phi| = 2$ cut.

For this analysis, events considered were those that passed the trigger discussed in Chapter 4, had a leading jet with a transverse momentum $p_T > 20$ GeV, a subleading jet with $p_T > 15$ GeV, where the leading and subleading jets had $\geq 95\%$ of the total energy in the event, an azimuthal difference of > 2 radians between the leading and subleading jets, an interaction point < 20 cm from the center of CMS in the z-direction (i.e., along the beam pipe), and where the leading and subleading jets had a pseudorapidity $-2.0 \leq \eta \leq 2.0$. The leading jet was defined as the jet with the highest p_T magnitude in each event, and the subleading jet was the jet with the second highest p_T magnitude in the same event. The leading and subleading jet p_T cuts, the 95% energy requirement, and the pseudorapidity limits were implemented based upon consultation with the CMS jet measurement group. All data presented from this section onward have these cuts applied.

In order for momentum to be conserved in a UPC dijet event, the two jets would be expected to have an azimuthal angular difference of π radians, which is demonstrated in Figure 6.2. Leading and subleading jet p_T yield distributions are shown in Figure 6.3. The right hand panel shows the sample of exclusive back to back dijets used in this analysis, while the left hand panel shows the

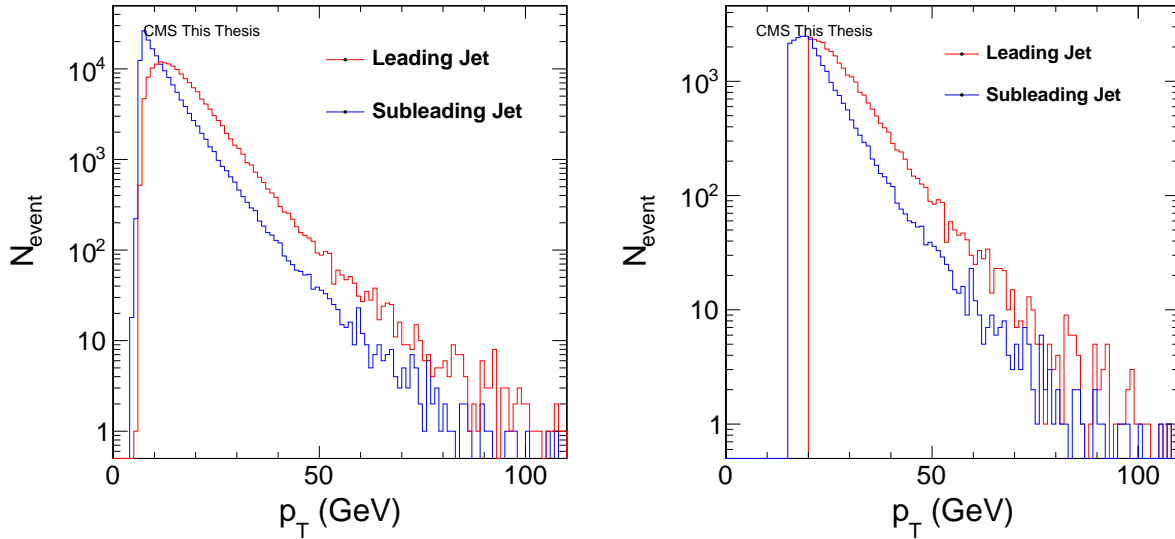


Figure 6.3: Leading and subleading jet p_T are shown here. The left plot includes no cuts on η for either the leading or the subleading jets, and the right plot applies the cuts where the leading jet has $p_T > 20$ GeV and the subleading jet has $p_T > 15$ GeV that were used in this analysis.

distributions for all back to back exclusive dijets. The curvature of the leading jet p_T distribution in left panel clearly shows the effect of the jet energy resolution. The distribution of average pseudorapidity between each leading jet and subleading jet is shown in Figure 6.4. The rapidity gap that is a defining characteristic of the UPC dijet interactions results means that both jets tend to strike one end of the detector, leading to the peaks around $|\eta| = 1.3$ and the trough around $|\eta| = 0$.

A larger neutron presence in one ZDC compared to the other would manifest itself as a strong ZDC signal in one detector but a weak signal in the other. On a two-dimensional histogram of ZDC+ signal and ZDC- signal, this would manifest itself as a strong L-shaped pattern along the axes centered at the origin but weaker signals further away from the axes. Figure 6.5 is a two-dimensional histogram of ZDC+ signal and ZDC- signal, and it shows exactly this.

Additionally, Figure 6.6 shows a two-dimensional histogram of the ratio of signal difference between ZDC+ and ZDC- to signal sum of ZDC+ and ZDC- versus dijet average η . When average η is close to -1, the ZDC asymmetry is close to -1, and when average η is close to +1, the ZDC asymmetry is close to +1. This figure indicates that the dijets are typically produced on the same

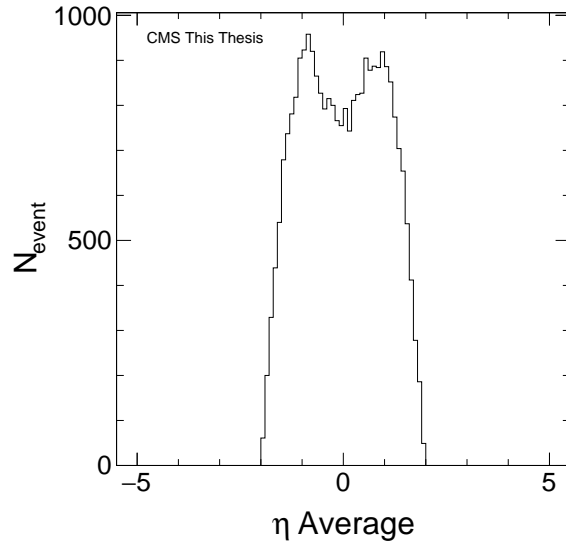


Figure 6.4: Distribution of average pseudorapidity between each dijet is shown here.

end of CMS where the target nuclide breaks up. An important aspect of this analysis was to examine the relationship between ZDC signal and average pseudorapidity of the dijets. This was done by the following methods:

- Developing ZDC examination criteria in which the time slices evaluated to contain the signal on one ZDC end (see Chapter 5) were paired with a signal threshold for that ZDC end to evaluate the presence of a ZDC signal and associated pseudorapidities;
- Using an energy threshold in one HF calorimeter and examining the signal on the corresponding ZDC end; and
- Comparing average pseudorapidities on either end of the CMS detector to the ZDC signal.

For the ZDC examination, two basic requirements were set: 1) at least one of the ZDC readout channels on one ZDC end was required to have its maximum signal in the time slice(s) evaluated to contain the signal (see Table 5.1), and 2) the ZDC end in question was required to have a signal of more than 500 fC. This requirement was set for both ZDC ends, ZDC+ and ZDC-. Each event could satisfy this requirement for both ZDC+ and ZDC-, ZDC+ but not ZDC-, ZDC- but not ZDC+, or neither ZDC+ nor ZDC-. Figure 6.7 shows the ZDC signal and the pseudorapidity for

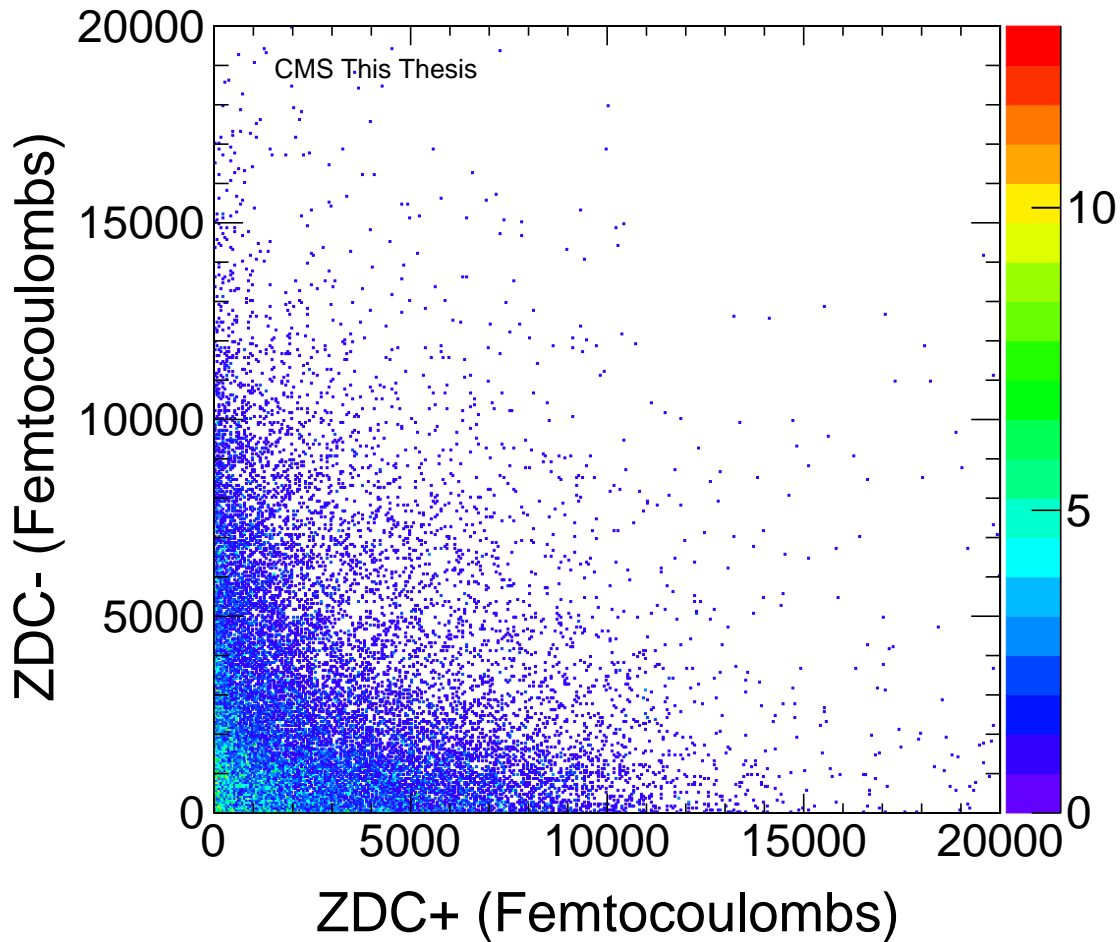


Figure 6.5: Two-dimensional histogram with ZDC+ signal in femtocoulombs on the x-axis and ZDC- signal in femtocoulombs on the y-axis. The tendency of an event’s signal to be strong in one ZDC and weak in the other, resulting in the L-shaped plot here, is indicative of a UPC where one nuclide breaks up and the other one remains intact.

each of these four scenarios. Figure 6.7 shows that there is a strong tendency for UPC dijets to have pseudorapidities on the same end of the the CMS detector where the ZDC signal is strongest, although this is not always the case as shown by the extension of the pseudorapidity distributions into the other end of CMS on the top right and bottom left of Figure 6.7. This indicates that the gluons in the photon-gluon interactions that produce the dijets tend to have greater energies than the photons in the CMS detector reference frame. The longitudinal component of their momentum therefore tends to be in the same direction as the fragments of the target nuclide that the ZDC de-

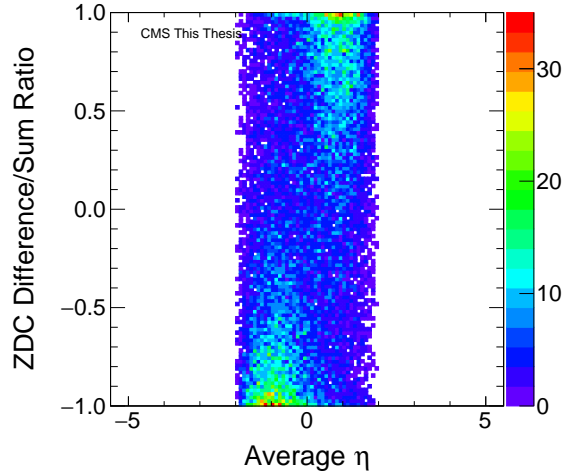


Figure 6.6: Two-dimensional histogram with the ratio of signal difference between ZDC+ and ZDC- to signal sum of ZDC+ and ZDC- versus dijet average η . The tendency of the signal to be strong at a ratio of -1 where $\eta < 0$ and at a ratio of 1 where $\eta > 0$ indicates that the dijets are typically produced on same end of CMS where the heavy nuclide from which they were produced breaks up.

fects but does not always. Using the data provided by Figure 6.7, x_1 , x_2 , and Q can be calculated via Equations 2.94, 2.95, and 2.11, respectively. The scenario where the ZDC examination requirements are met for ZDC+ but not ZDC-, which results in a strong ZDC+ signal but minimal ZDC- signal, resolves the ambiguity between x_1 and x_2 such that x_1 is the gluon momentum fraction and x_2 is the photon momentum fraction. Q for the photon can then be calculated using the x_2 distribution in Equation 2.11. On the other hand, the scenario where the ZDC examination requirements are met for ZDC- but not ZDC+, which results in a strong ZDC- signal but minimal ZDC+ signal, resolves the ambiguity between x_1 and x_2 such that x_1 is the photon momentum fraction and x_2 is the gluon momentum fraction. Q for the photon can then be calculated using the x_1 distribution in Equation 2.11. Figures 6.8 and 6.9 show these calculated distributions.

Comparing HF and ZDC signals was useful given the very forward location of the HF in CMS and therefore the likelihood that some debris from nuclear breakup would be detected by the HF as well as the ZDC. For the HF threshold, two specific scenarios were examined. In the first, there was more than 5 GeV of energy deposited in HF- and less than 5 GeV deposited in HF+ for each event. In the second, there was less than 5 GeV in HF- and more than 5 GeV in HF+. Both of

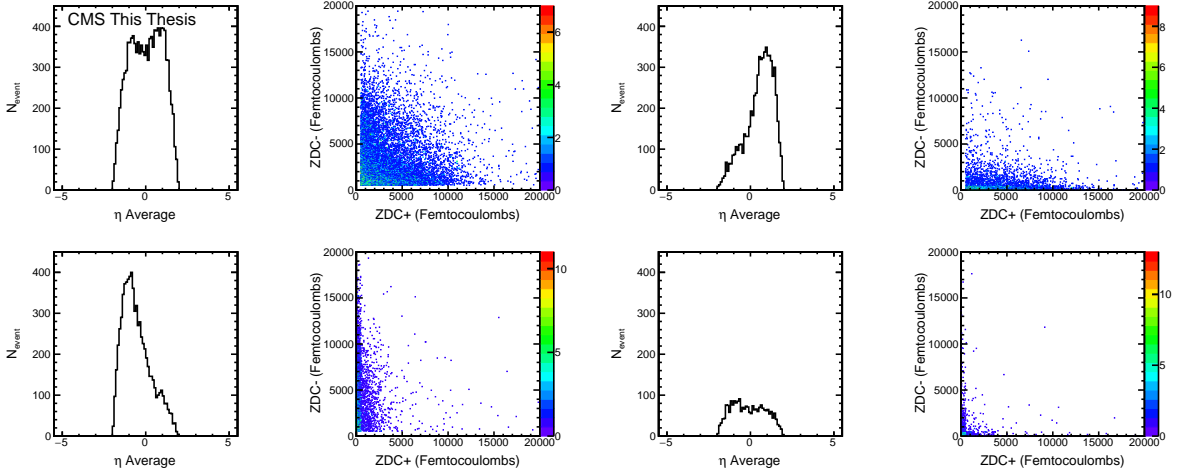


Figure 6.7: Average pseudorapidity (η) and ZDC signal for cases where ZDC examination requirements were met for both ZDC+ and ZDC- (top left), ZDC+ but not ZDC- (top right), ZDC- but not ZDC+ (bottom left), and neither ZDC+ nor ZDC- (bottom right).

these cases are shown in Figure 6.10, where the former case is shown in the top row and the latter case in the bottom row. Again, average pseudorapidity between the leading jet and the subleading jet is compared to ZDC signal. This examination of HF thresholds indicates that the gluons in the photon-gluon interactions that produce the dijets tend to have greater energies than the photons in the CMS detector reference frame, and the longitudinal components of their momenta tend to be in the same direction as the fragments of the target nuclide that the ZDC detects. It is also indicated, again, that this is not always the case, as there is a tail in the average pseudorapidity plots in Figure 6.10 extending to the other end of the detector. However, this effect was not as pronounced here as it was with the ZDC examination. Similarly to the ZDC examination, the scenario where there is more than 5 GeV in HF-, less than 5 GeV in HF+, a strong signal in ZDC-, and a relatively weak signal in ZDC+ resolves the ambiguity between x_1 and x_2 such that x_1 is the photon momentum fraction and x_2 is the gluon momentum fraction. Q for the photon can then be calculated using the x_1 distribution in Equation 2.11. Likewise, the scenario where there is more than 5 GeV in HF+, less than 5 GeV in HF-, a strong signal in ZDC+, and a relatively weak signal in ZDC- resolves the ambiguity between x_1 and x_2 such that x_1 is the gluon momentum fraction and x_2 is the photon momentum fraction. Q for the photon can then be calculated using the x_2

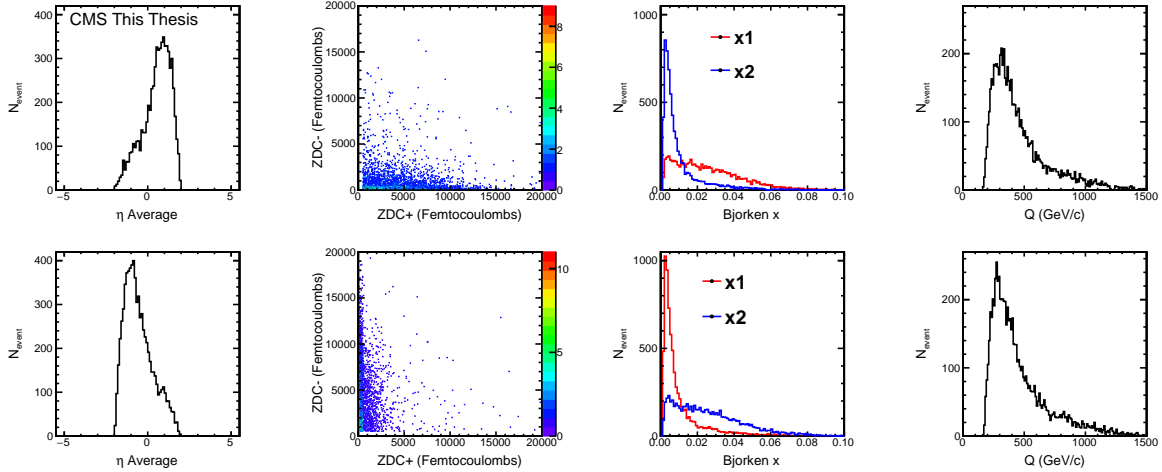


Figure 6.8: Average η and ZDC signal for the cases in Figure 6.7 where ZDC examination requirements were met for ZDC+ but not ZDC- (top row) and ZDC- but not ZDC+ (bottom row), along with their respective corresponding calculations of x_1 , x_2 , and photon Q. ZDC examination requirements being met for ZDC+ but not ZDC- resolves the x ambiguity such that x_1 is the gluon momentum fraction and x_2 is the photon momentum fraction, whereas ZDC examination requirements being met for ZDC- but not ZDC+ resolves the ambiguity between x_1 and x_2 such that x_1 is the photon momentum fraction and x_2 is the gluon momentum fraction.

distribution in Equation 2.11.

ZDC signal was also examined for the average pseudorapidity on either end of the CMS detector. These results are shown in Figure 6.11, in which the average pseudorapidity η of the two jets is greater than zero on the left and less than zero on the right. These plots show a tendency for a strong signal in the ZDC on the side of CMS where the average η for a dijet event lies. However, the plots also reveal that a weaker signal is present in the ZDC on the opposite side of CMS from where the average η lies, which could be consistent with some photons having energies in excess of the gluons they interact with as indicated by Figures 6.7 and 6.10. Note that in the analysis presented from Section 6.4 the ZDC requirements were not applied. At the same time, the ZDC was used as a cross check for the exclusivity selection.

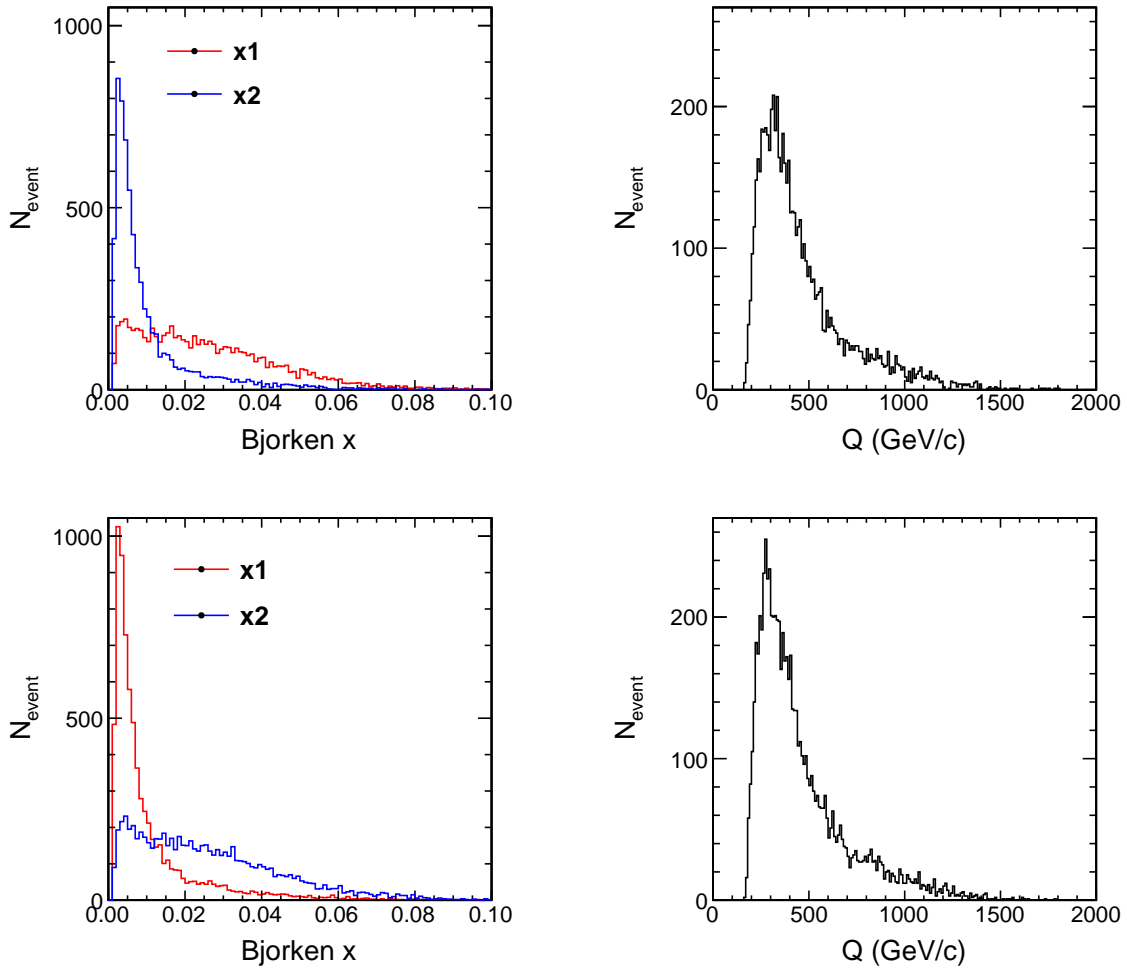


Figure 6.9: Bjorken x and Q distributions from Figure 6.8 are shown here.

6.3 The Pseudorapidity Gap

As stated previously, one characteristic of UPC jets is a pseudorapidity gap. This gap was utilized through the trigger requirement that energy would be measured in the HF calorimeter on only one end of CMS, as described in Chapter 4. For the analysis, in addition, a more restrictive definition of the rapidity gap was needed. Thus, a backward rapidity gap (BRG) and a forward rapidity gap (FRG) were defined as:

$$\text{BRG} = \eta_{\text{min}} + 2.4 \quad (6.1)$$

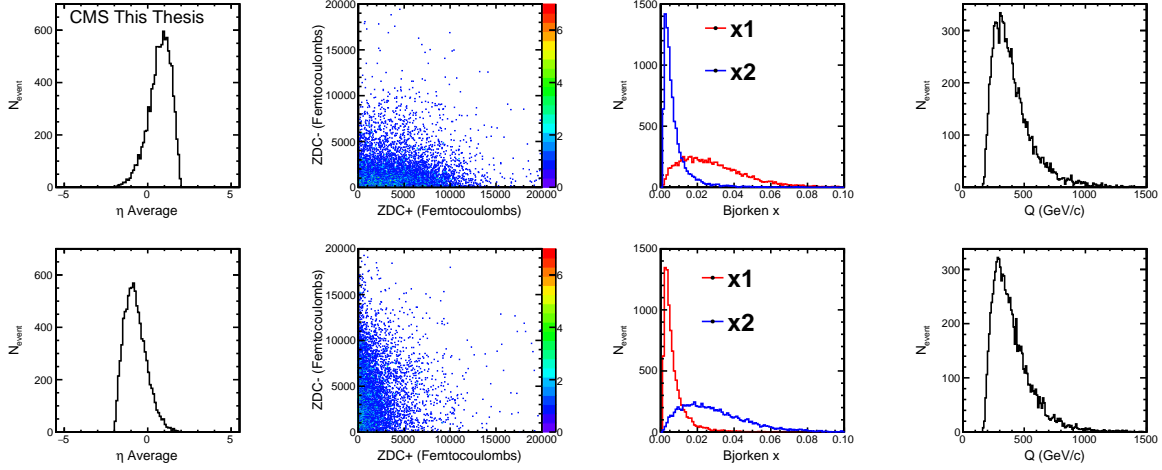


Figure 6.10: Average pseudorapidity, ZDC signal, x_1 and x_2 , and Q where, for each event, more than 5 GeV of energy was detected in HF- and less than 5 GeV in HF+ in the top row, and vice versa in the bottom row. The situation in the top row with stronger signals in HF- and ZDC- along with weaker signals in HF+ and ZDC+ resolves the ambiguity between x_1 and x_2 such that x_1 is the photon momentum fraction and x_2 is the gluon momentum fraction. Likewise, the situation in the bottom row with stronger signals in HF+ and ZDC+ along with weaker signals in HF- and ZDC- resolves x ambiguity such that such that x_1 is the gluon momentum fraction and x_2 is the photon momentum fraction.

$$\text{FRG} = 2.4 - \eta_{\max} \quad (6.2)$$

where η_{\min} was the minimum track pseudorapidity for the UPC dijet event, and η_{\max} was the maximum track pseudorapidity for the UPC dijet event. All terms in Equations 6.1 and 6.2 have units of pseudorapidity (η) and $|\eta| = 2.4$ corresponds to the edges of the silicon tracker. Backward dominant events were then defined to be events where $\text{BRG} > 1.2$ and $\text{BRG} > \text{FRG}$, and forward dominant events were defined to be events where $\text{FRG} > 1.2$ and $\text{FRG} > \text{BRG}$. Figure 6.12 illustrates the basis of these two definitions. Where $\text{BRG} > \text{FRG}$ and vice versa, the largest concentrations of events occur where $\Delta\eta > 1.2$. Furthermore, Figure 6.13 shows the average dijet η for backward dominant and forward dominant events. Backward dominant events tend to correspond to dijets at forward pseudorapidities, and forward dominant events tend to correspond to dijets at backward pseudorapidities. This is consistent with the findings of the previous section, and is further amplified by Figure 6.14. Figure 6.14 shows the difference/sum ratio of the ZDC

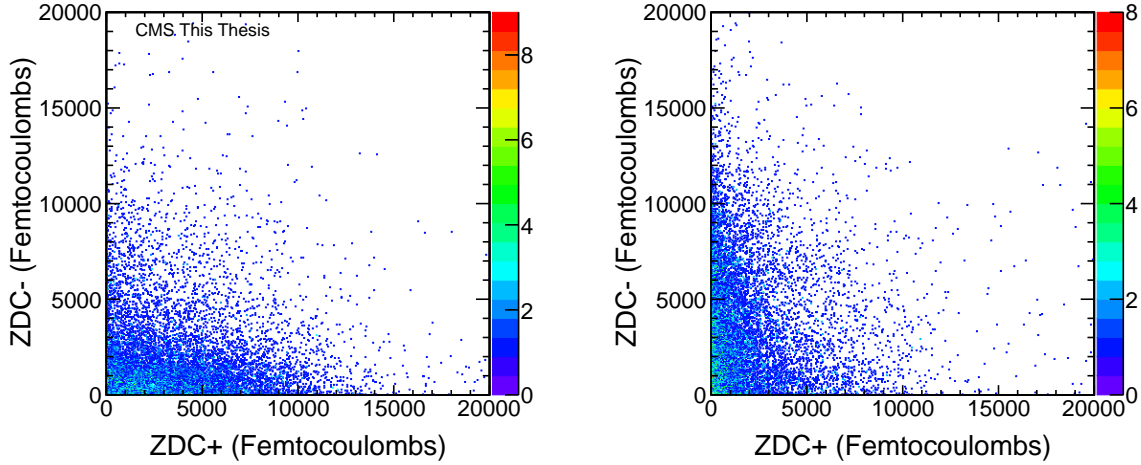


Figure 6.11: ZDC+ and ZDC- signals where average η between the dijets is > 0 on the left and < 0 on the right.

signal, both by as a function of average η and by itself, for backward dominant and forward dominant events. Backward dominant events have a ZDC difference/sum ratio that peaks at $+1$, while forward dominant events have a ZDC difference/sum ratio that peaks at -1 .

6.4 Azimuthal Correlation Analysis

As mentioned in Chapters 1 and 2, the goal of this analysis is to study the correlation between gluons in the nucleus via the azimuthal correlations between the total transverse momentum of the dijets and the momentum difference of the dijets. To do this, an azimuthal correlation analysis, or v_2 analysis, was performed. This process began by considering the vector sum and the vector difference of the leading jet and the subleading jet in each UPC event analyzed, as shown in Figure 6.15. The vector sum of the leading and subleading jet vectors is labeled \mathbf{Q}_T , the vector difference between them is $2\mathbf{P}_T$, and the angle running in a counter-clockwise direction from $2\mathbf{P}_T$ to \mathbf{Q}_T is Φ . The specific definitions of \mathbf{Q}_T and \mathbf{P}_T are as follows:

$$\mathbf{Q}_T = \vec{p}_{T,leading} + \vec{p}_{T,subleading} \quad (6.3)$$

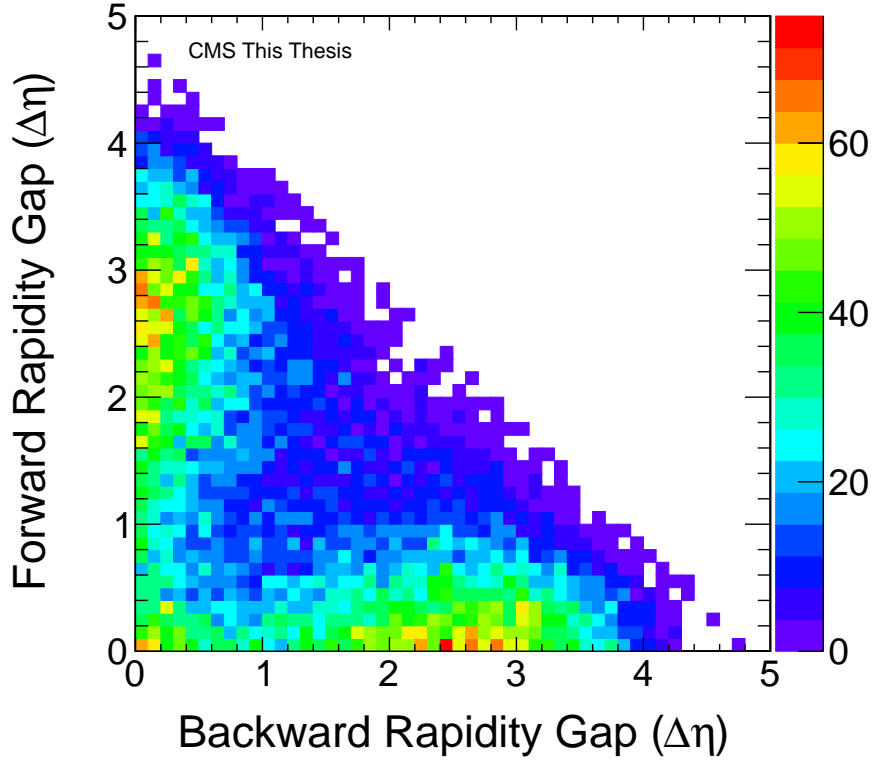


Figure 6.12: Two-dimensional histogram comparing BRG and FRG for all events being analyzed. The high concentrations of events where there is high BRG and low FRG or low BRG and high FRG where $\Delta\eta > 1.2$ motivated the definitions of backward dominant and forward dominant events in this analysis.

$$\begin{aligned}
 \mathbf{P}_T &= \frac{\vec{p}_{T,leading} - \vec{p}_{T,subleading}}{2}, \text{ when leading jet mass} \geq \text{subleading jet mass}, \\
 \mathbf{P}_T &= \frac{\vec{p}_{T,subleading} - \vec{p}_{T,leading}}{2}, \text{ when leading jet mass} < \text{subleading jet mass},
 \end{aligned}
 \tag{6.4}$$

where the energy equivalent of jet mass was defined in Equation 2.79. The distinction between two definitions of P_T based on whether the leading jet or the subleading jet had the greater mass was important in the analysis, because a definition of P_T where the subleading jet was always subtracted from the leading jet would introduce a bias into the calculation of Φ such that Φ would always have a value between 0° - 90° or 270° - 360° . The reason for this is that the leading jet, defined as the jet with the highest p_T magnitude, always had a greater p_T magnitude than the subleading jet (defined as the jet with the second highest p_T magnitude); therefore the sum of these vectors would always be in the same hemisphere if only the first definition in Equation 6.4 was used. To calculate Φ with

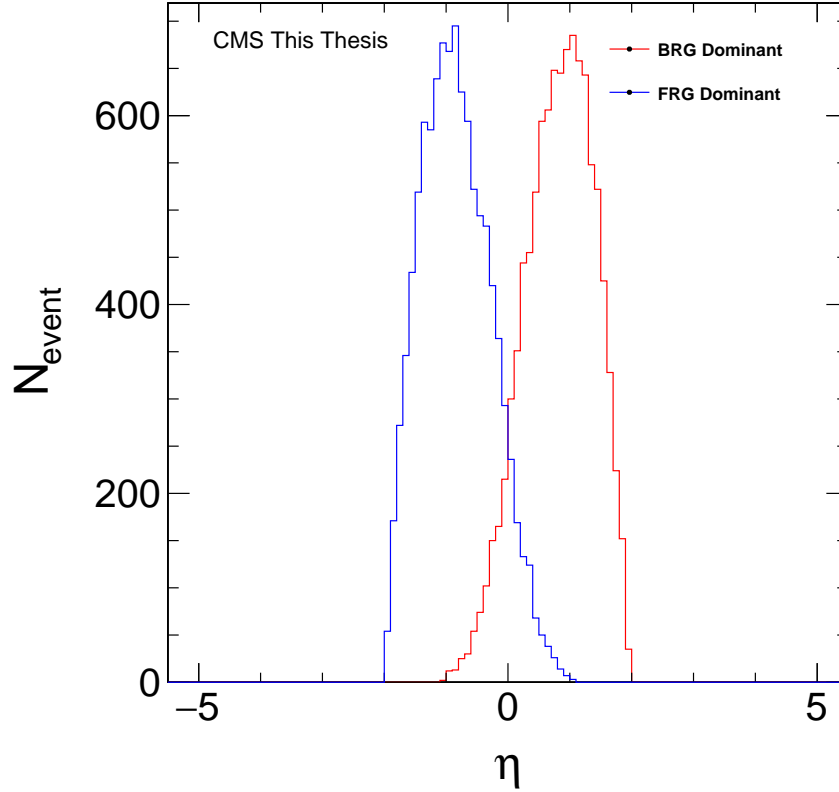


Figure 6.13: Average dijet η for backward dominant events (labeled "BRG Dominant") and forward dominant events (labeled "FRG Dominant"). BRG Dominant corresponds to more forward dijet pseudorapidities and FRG Dominant corresponds to more backward dijet pseudorapidities.

respect to \mathbf{Q}_T , the dot product and the cross product of \mathbf{P}_T and \mathbf{Q}_T were utilized such that

$$\cos \Phi = \frac{\mathbf{P}_T \cdot \mathbf{Q}_T}{|\mathbf{P}_T||\mathbf{Q}_T|}, \quad (6.5)$$

$$\sin \Phi = \frac{|\mathbf{P}_T \times \mathbf{Q}_T|}{|\mathbf{P}_T||\mathbf{Q}_T|}. \quad (6.6)$$

A separate angle α was then defined:

$$\alpha = \arccos |\cos \Phi|. \quad (6.7)$$

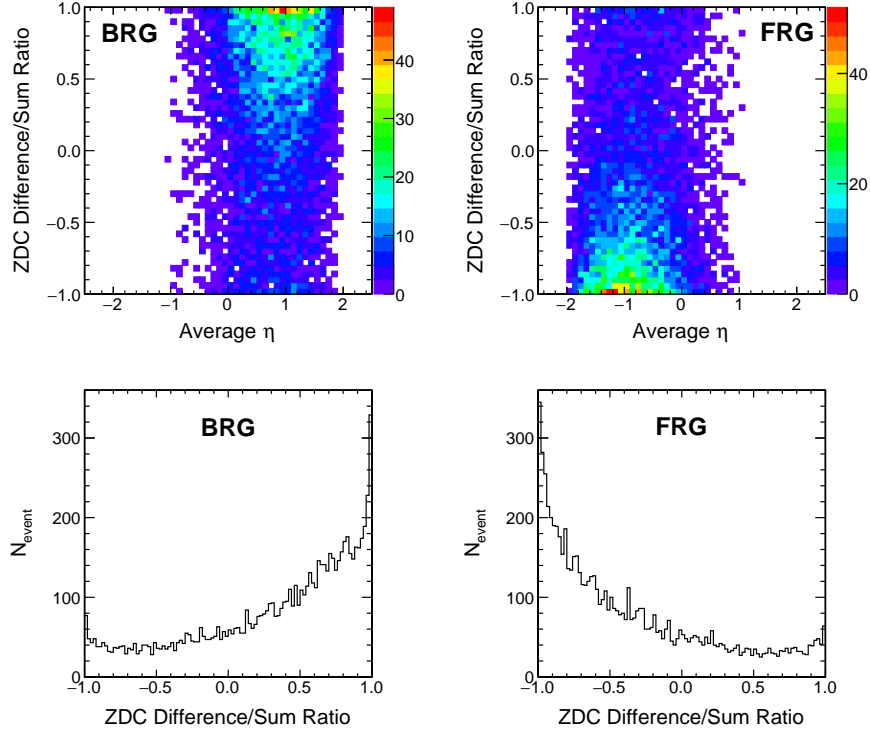


Figure 6.14: The ZDC difference/sum ratio, as a function of average η (top row) and by itself (bottom row), is shown here. Backward dominant event (BRG) are shown in the left column, and forward dominant events (FRG) are shown in the right column. BRG event tend toward a ZDC difference/sum ratio at $\eta \approx 1$, while (FRG) events tend toward to a ZDC difference/sum ratio at $\eta \approx -1$. The BRG dominant events totaled 10294, with a mean difference/sum ratio of 0.321 at a standard deviation of 0.561, and a mean average η of 0.8162 at a standard deviation of 0.5576. The FRG dominant events totaled 10316, with a mean difference/sum ratio of -0.363 at a standard deviation of 0.562, and a mean average η of -0.8196 at a standard deviation of 0.5689.

If Equation 6.5 gives $\cos \Phi \geq 0$ and Equation 6.6 gives $\sin \Phi \geq 0$, $\Phi = \alpha$; if Equation 6.5 gives $\cos \Phi < 0$ and Equation 6.6 gives $\sin \Phi \geq 0$, $\Phi = \pi - \alpha$; if Equation 6.5 gives $\cos \Phi < 0$ and Equation 6.6 gives $\sin \Phi < 0$, $\Phi = \pi + \alpha$; or if Equation 6.5 gives $\cos \Phi \geq 0$ and Equation 6.6 gives $\sin \Phi < 0$, $\Phi = 2\pi - \alpha$. The distribution of Φ is shown in Figure 6.16.

The infinitesimal distribution of exclusive dijet events over Φ , $\frac{dN}{d\Phi}$, can be modeled as a Fourier series. A Fourier series is defined as

$$\frac{dN}{d\Phi} = \sum_{n=0}^{\infty} v_n \cos i\Phi. \quad (6.8)$$

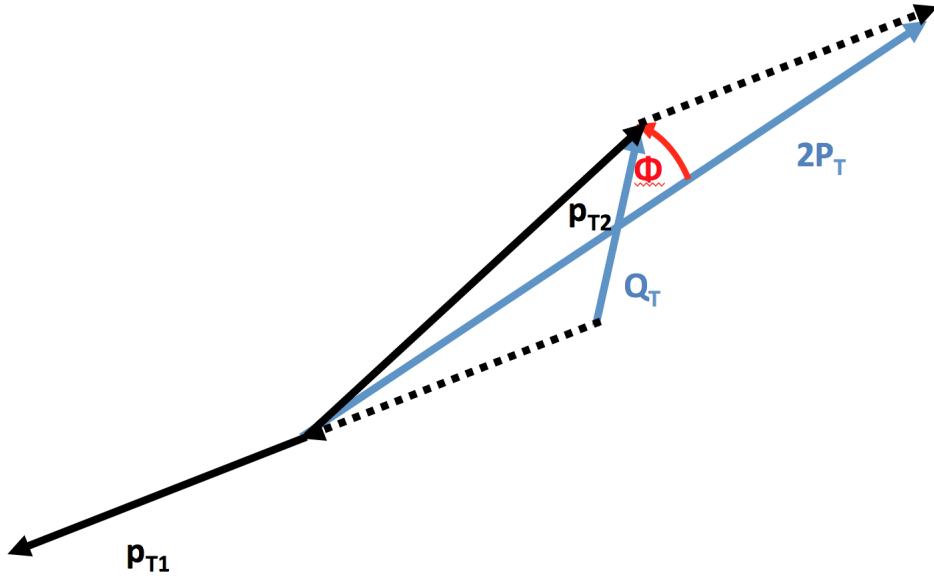


Figure 6.15: Leading and subleading jet vectors, with the leading jet p_T denoted by \mathbf{p}_{T1} and the subleading jet p_T denoted by \mathbf{p}_{T2} . \mathbf{Q}_T and $2\mathbf{P}_T$ are also shown, and the angle between them is denoted as Φ .

The goal was then to calculate the second Fourier component of the distribution $dN/d\Phi$ shown in Figure 6.16, v_2 :

$$v_2 = \langle \cos 2\Phi \rangle, \quad (6.9)$$

where

$$\cos 2\Phi = \cos^2\Phi - \sin^2\Phi \quad (6.10)$$

and the angular brackets denote the average value of $\cos 2\Phi$ over a number of events. v_2 was analyzed over P_T ranges of 18-43 GeV and Q_T ranges of 0-25 GeV, as those ranges were where the bulk of the signal lay, as shown in Figure 6.17 and Figure 6.18. In finding v_2 , it was of interest to examine v_2 separately for backward dominant events and forward dominant events. Figures 6.19 and 6.20 show these results.

It is important to ensure that the v_2 signal is the result of a true physics correlation and not an artifact of the acceptance of CMS. For studies of anisotropic flow in nuclear collisions it is usual to estimate the acceptance effects by constructing the v_2 of mixed events [41]. Mixed events contain

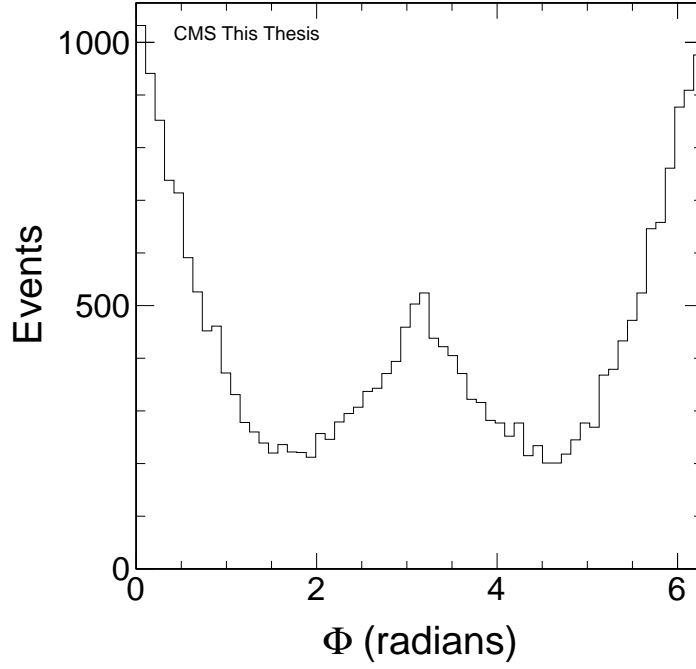


Figure 6.16: Raw distribution of Φ between \mathbf{Q}_T and $2\mathbf{P}_T$.

no physics correlations but are sensitive to the detector acceptance and resolution. Mixed events were constructed by calculating Φ and v_2 using the same procedures as described above, only this time the leading jet was paired with a subleading jet from another event, and this was done up to 5000 times, each time using a different subleading jet from a different event for the leading jet of the current event. Figures 6.21 and 6.22 show the v_2 results for mixed events. This mixed v_2 is then subtracted from raw v_2 to produce $v_{2,subtracted}$ as follows:

$$v_{2,subtracted} = v_{2,raw} - v_{2,mixed}. \quad (6.11)$$

$v_{2,subtracted}$ is shown in Figures 6.23 and 6.24. While this method is standard in heavy ion flow studies, the theoretical framework for handling detector effects in the correlation of UPC dijets is not yet established. For this reason, the three variables, $v_{2,raw}$, $v_{2,mixed}$ and $v_{2,subtracted}$ are presented in this analysis.

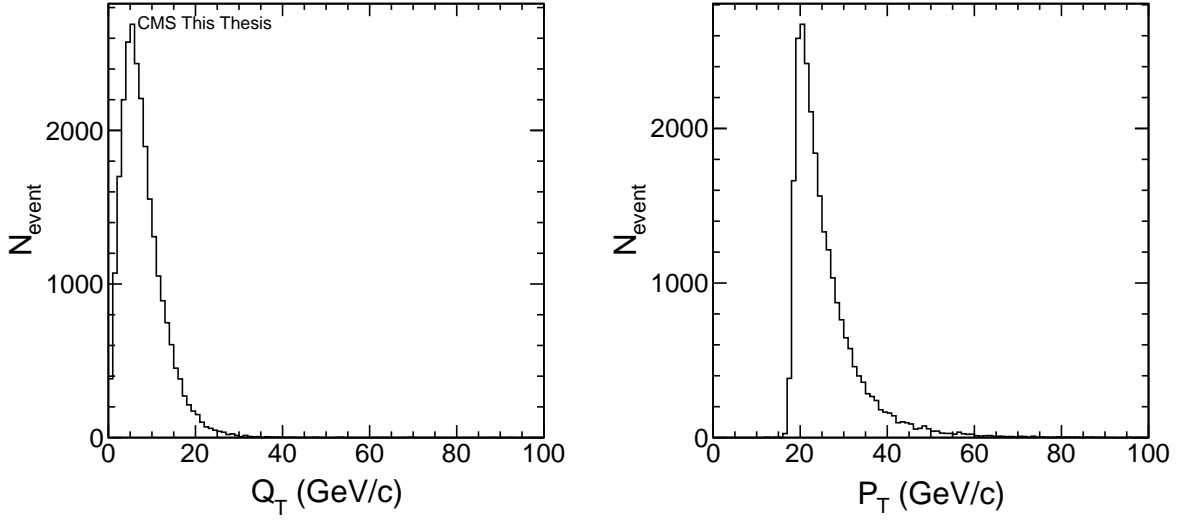


Figure 6.17: Overall ranges of Q_T and P_T signals are shown here. Since most of the Q_T signal was between 0-25 GeV/c and most of the P_T signal was between 18-43 GeV/c, these constituted the analysis ranges for v_2 .

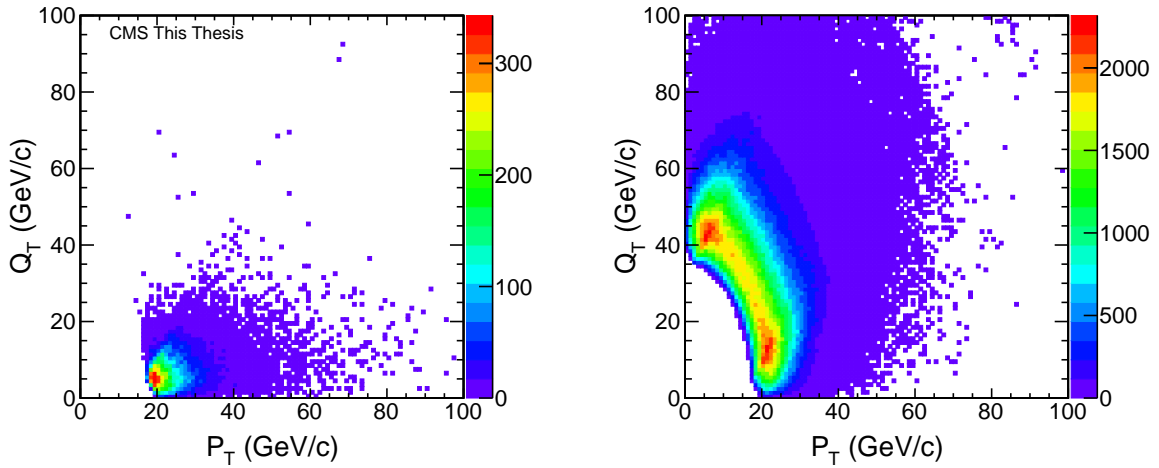


Figure 6.18: Two dimensional histograms of Q_T vs. P_T are shown here for raw signal (left) and mixed events (right). The raw signal again shows the principal Q_T signal between 0-25 GeV/c and the principal P_T signal between 18-43 GeV/c.

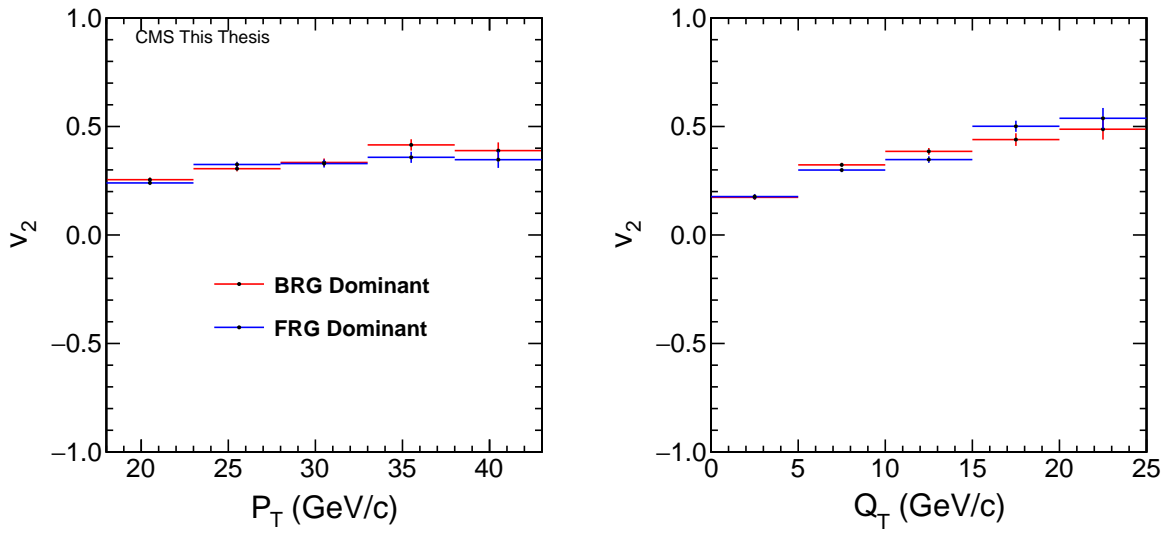


Figure 6.19: Raw v_2 vs. P_T (left) and Q_T (right) for BRG-dominant events and FRG-dominant events.

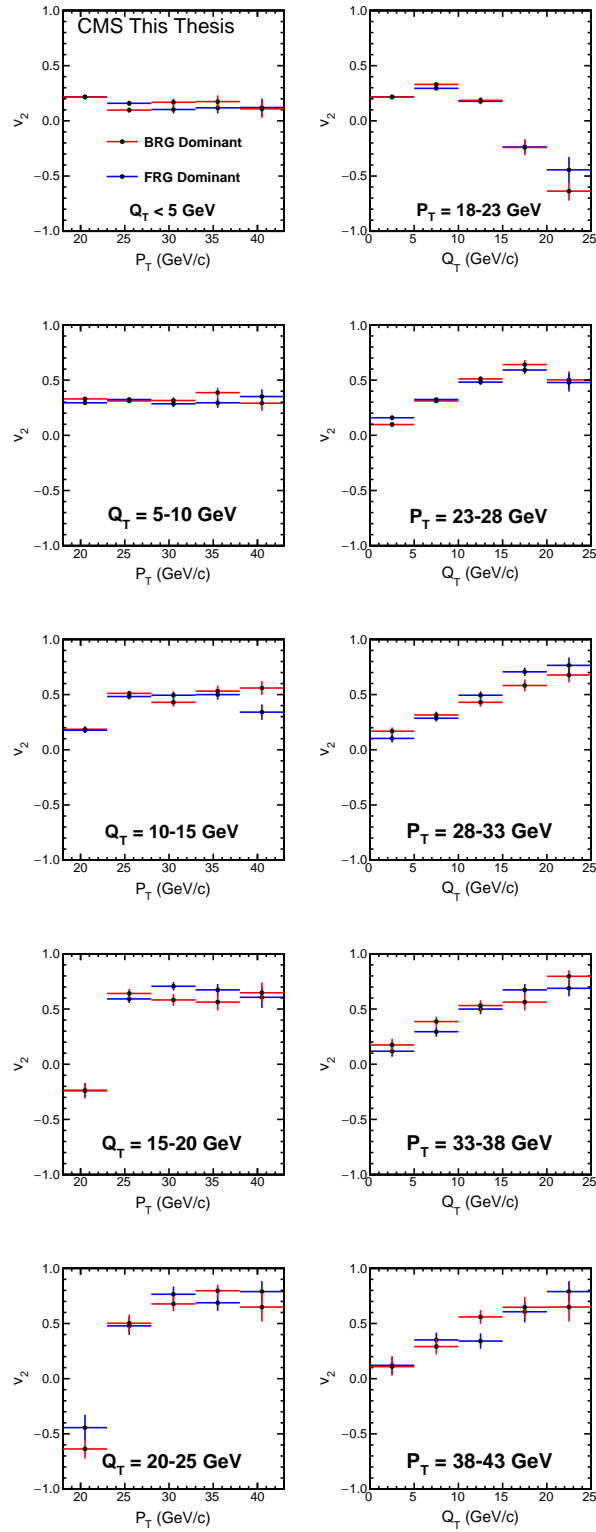


Figure 6.20: Raw v_2 vs. P_T and Q_T for BRG-dominant events and FRG-dominant events within indicated Q_T and P_T ranges.

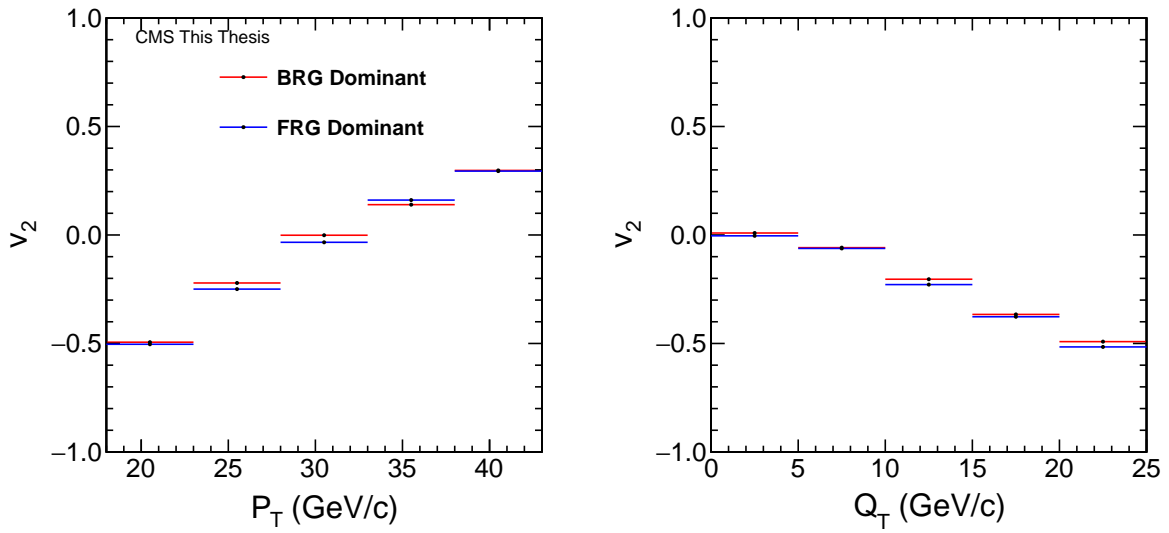


Figure 6.21: Mixed events v_2 vs. P_T (left) and Q_T (right) for BRG-dominant events (red) and FRG-dominant events (blue).

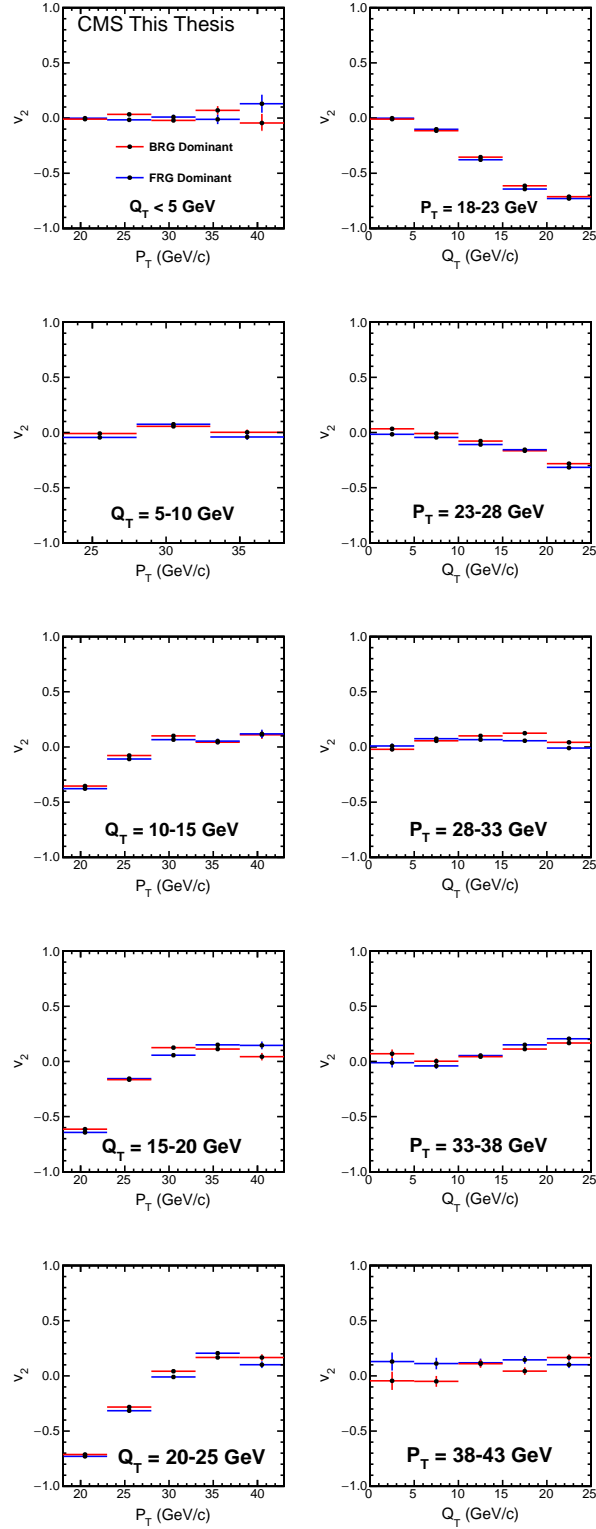


Figure 6.22: Mixed events v_2 vs. P_T and Q_T for BRG-dominant events (red) and FRG-dominant events (blue) within indicated P_T and Q_T ranges. For v_2 vs. Q_T , many of the analysis bins have $v_2 = 0$.

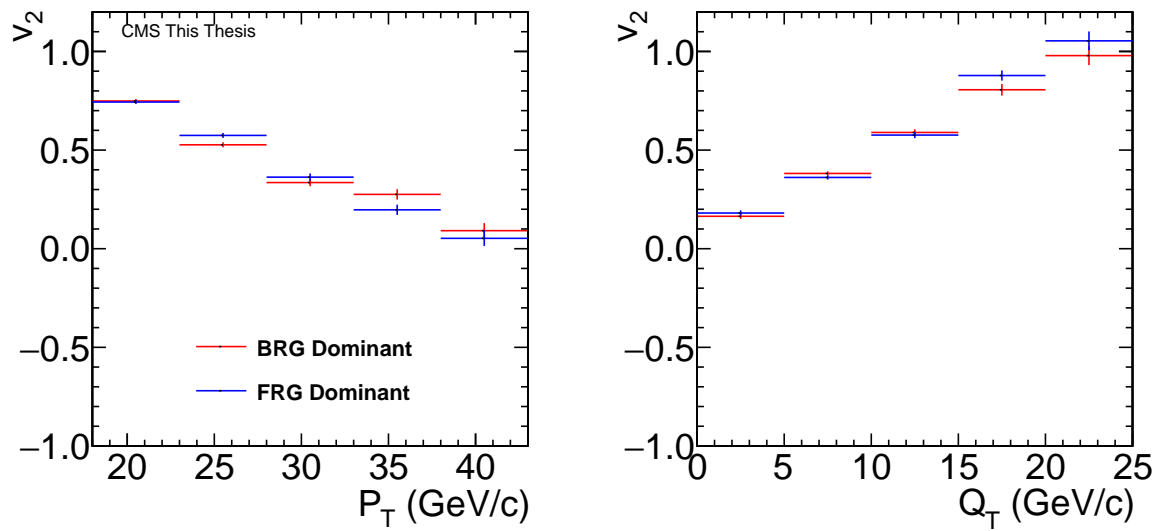


Figure 6.23: $v_{2,subtracted}$ vs. P_T (left) and Q_T (right) for BRG-dominant events (red) and FRG-dominant events (blue).

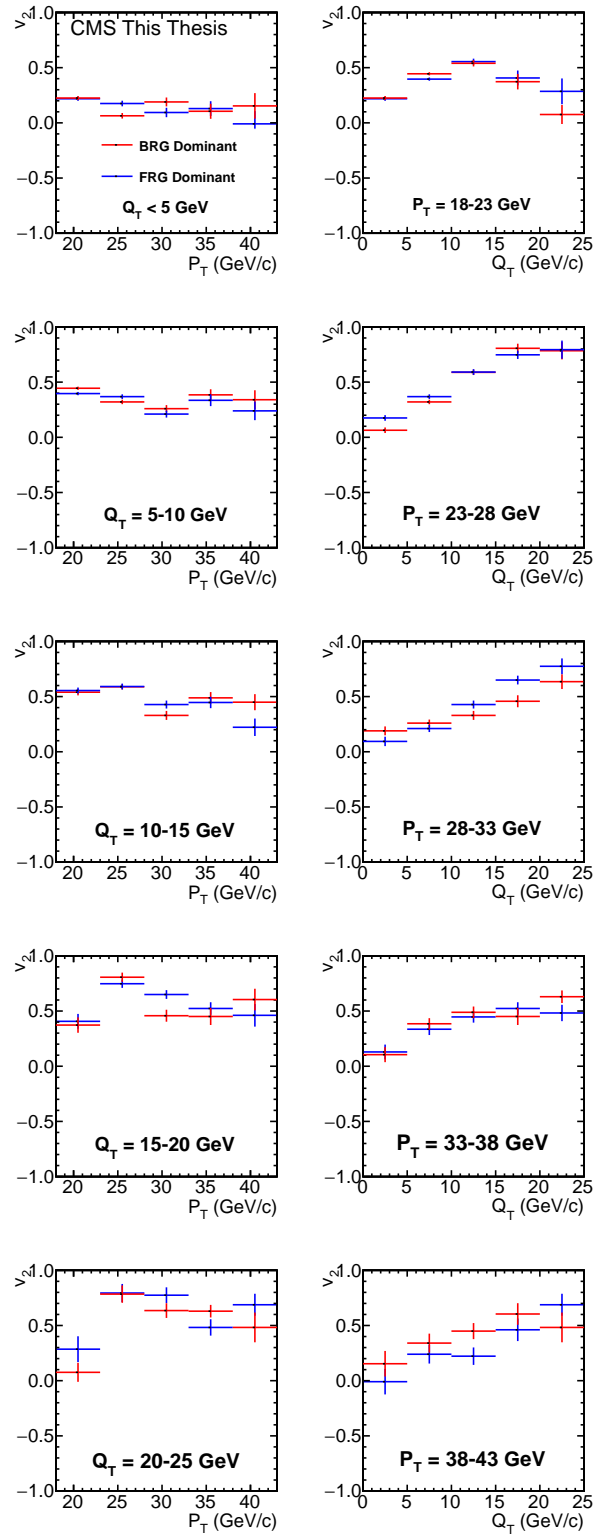


Figure 6.24: $v_{2,subtracted}$ vs. P_T and Q_T for BRG-dominant events (red) and FRG-dominant events (blue) within indicated P_T and Q_T ranges.

Chapter 7

Cross Checks and Systematic Uncertainties

This chapter describes the systematic checks made to test the robustness of the physics results presented at the end of Chapter 6 to variations of cuts used in the analysis. In systematic checks, the effects that specified characteristics of the experimental device have on the experimental results of interest are examined by means of calculating the χ^2 value. The quantity $\Delta v_{2,subtracted}$ is the difference in $v_{2,subtracted}$ that results when one of the experimental cuts is changed from the chosen baseline parameter, that is

$$\Delta v_{2,subtracted, i} = (v_{2,subtracted, i})_{baseline} - (v_{2,subtracted, i})_{changed}. \quad (7.1)$$

The uncertainty on $\Delta v_{2,subtracted}$ is denoted by σ . The definition of σ depends on some specific circumstances. If the changed parameters produce data that are completely independent from the data produced by the baseline parameters, then

$$\sigma_i = \sqrt{\sigma_{i, baseline}^2 + \sigma_{i, changed}^2}, \quad (7.2)$$

where $\sigma_{i, baseline}$ is the statistical error for $(v_{2,subtracted, i})_{baseline}$ and $\sigma_{i, changed}$ is likewise the statistical error for $(v_{2,subtracted, i})_{changed}$. However, if the changed parameters yield data that is completely included in the data yielded by the baseline parameters,

$$\sigma_i = \sqrt{|\sigma_{i, baseline}^2 - \sigma_{i, changed}^2|}. \quad (7.3)$$

In this analysis the χ^2 value has the general form

$$\chi^2 = \sum_{i=1}^{25} \frac{(\Delta v_{2,subtracted, i})^2}{\sigma_i^2}. \quad (7.4)$$

In Equation 7.4 i runs from 1 to 25 because there were a total of 25 $v_{2,subtracted}$ values, that is 5 $v_{2,subtracted}$ values for each of the five intervals of Q_T analyzed between 0 and 25 GeV/c. A χ^2 of 25 or less indicates statistical consistency between data resulting from baseline parameters and data resulting from changed parameters. Therefore, if χ^2 was approximately 25 or less, the cross check between the varied parameter and the baseline parameter was satisfactory. If χ^2 was significantly greater than 25, this was indicative of a systematic error of unknown origin. In the latter case, a systematic error SE was determined by requiring the new χ^2 , χ_{new}^2 , to be 25:

$$\chi_{new}^2 = \sum_{i=1}^{25} \frac{(\Delta v_{2,subtracted, i})^2}{\sigma_i^2 + SE^2} = 25. \quad (7.5)$$

After each check, systematic errors found were combined into a total systematic error as follows:

$$SE_{total} = \sqrt{(SE_1)^2 + (SE_2)^2 + \dots} \quad (7.6)$$

7.1 Comparing Forward and Backward Events

The first systematic check was to compare backward dominant and forward dominant dijet events as defined in Section 6.3 of Chapter 6. Since both ends of the CMS experiment are the same in principle, one would have expected $v_{2,subtracted}$ of backward dominant events and forward dominant events to be statistically consistent. This was therefore the most obvious parameter to explore as a systematic check. Thus the forward/backward symmetry of CMS was the first systematic check.

For this check, the forward dominant $v_{2,subtracted}$ values shown in Figure 6.24 were subtracted

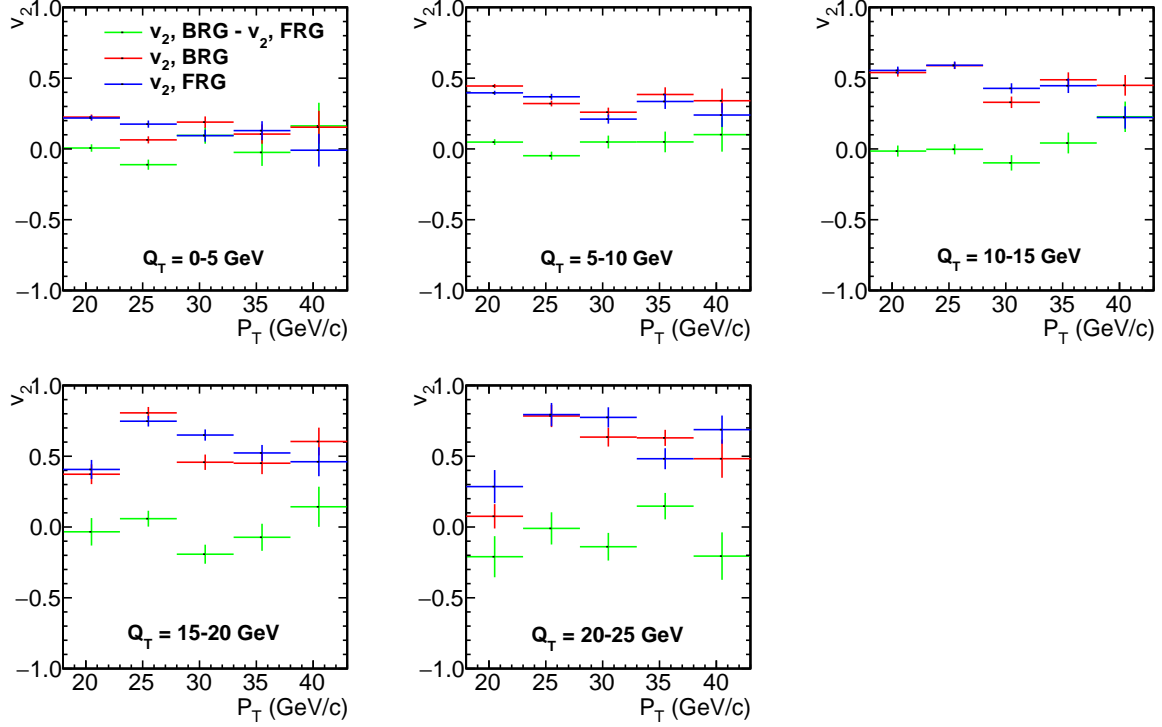


Figure 7.1: $v_{2,subtracted}$ results for backward dominant events, forward dominant events, and their difference is shown here.

from the backward dominant $v_{2,subtracted}$ in that figure. Since these values were completely independent of each other, their statistical errors were combined in accordance with Equation 7.2. Figure 7.1 shows the backward dominant $v_{2,subtracted}$ results, the forward dominant $v_{2,subtracted}$ results, and their difference.

For the difference of $v_{2,subtracted}$ between backward dominant and forward dominant events, the χ^2 was determined to be 51.4. An SE of 0.06 was then found to yield a χ^2 of 25.1. The average values of $v_{2,subtracted}$ between backward dominant events and forward dominant events were taken to be the main results. These will hereafter be referred to as $\langle v_{2,subtracted} \rangle$. In subsequent systematic checks, $\langle v_{2,subtracted} \rangle$ was used as the baseline $v_{2,subtracted}$ as there was no way to decide whether forward dominant or backward dominant was better.

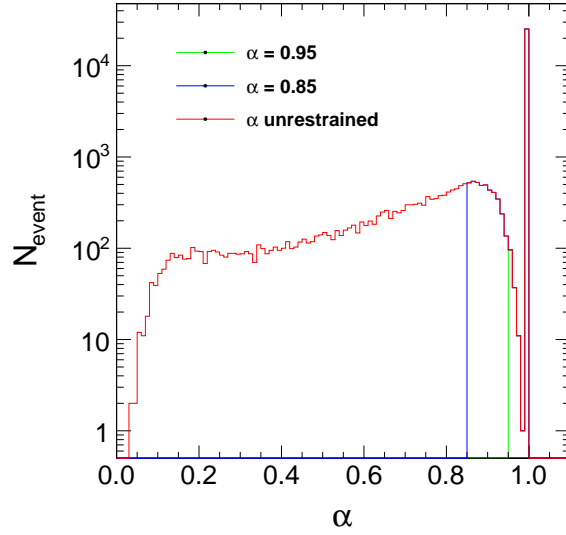


Figure 7.2: Number of events for $\alpha = 0.95$, $\alpha = 0.85$, and no limits on α are shown here.

7.2 Varying the Exclusivity Parameter α

The second systematic check was performed by changing the value of the proportion of event energy required to be contained in the dijets (labeled α). For this and the following systematic checks, $\langle v_{2,subtracted} \rangle$ vs. P_T for the results in Figure 6.24 were calculated, along with the statistical uncertainty. The parameters being checked were then changed, while all other baseline analysis parameters discussed in Section 6.2 were retained. After the parameter in question was changed, $\langle v_{2,subtracted} \rangle$ vs. P_T was then recalculated, along with their statistical errors. The χ^2 value was then calculated as follows:

$$\chi^2 = \sum_{i=1}^{25} \frac{\langle \Delta v_{2,subtracted, i} \rangle^2}{\sigma_i^2}, \quad (7.7)$$

where

$$\langle \Delta v_{2,subtracted, i} \rangle = \langle v_{2,subtracted, i} \rangle_{baseline} - \langle v_{2,subtracted, i} \rangle_{changed}, \quad (7.8)$$

and, since the parameters that were changed yielded data that was completely included in that yielded by the baseline parameters, σ_i^2 was found by Equation 7.3.

For the systematic check on α , α was changed from 0.95 to 0.85 while all other baseline

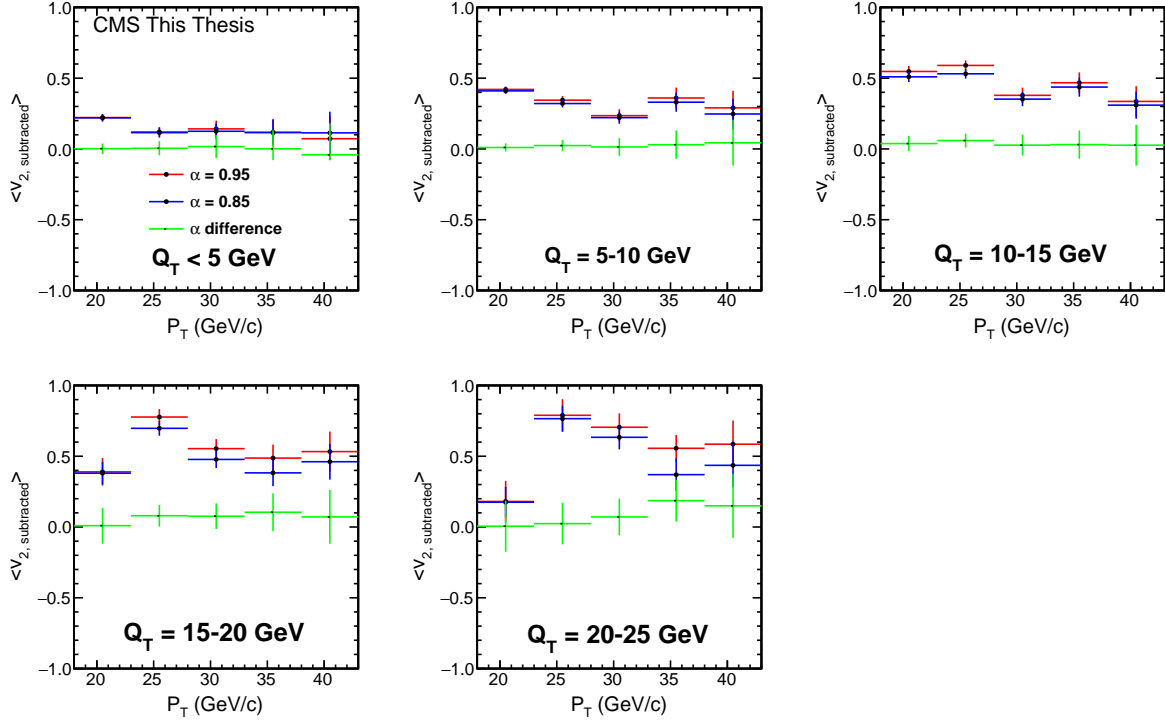


Figure 7.3: $\langle v_{2,subtracted} \rangle$ vs. P_T for Q_T intervals analyzed are shown here for $\alpha = 0.85$ and $\alpha = 0.95$.

parameters were retained. Figure 7.2 shows a comparison for $\alpha = 0.95$, $\alpha = 0.85$, and no limits on α ; and Figure 7.3 shows the effect on $\langle v_{2,subtracted} \rangle$ when $\alpha = 0.95$ and $\alpha = 0.85$. From these values, the χ^2 was found to be 118.8. An SE of 0.044 was found to yield a χ^2 of 25.1.

7.3 Varying the Back to Back Requirement $|\Delta\phi|$

The third systematic check was performed on the minimum azimuthal difference allowed between the dijets (labeled $|\Delta\phi|$). For the systematic check on $|\Delta\phi|$, the requirement was changed from $|\Delta\phi| > 2$ to $|\Delta\phi| > 2.25$, while all other baseline parameters were retained. Figure 7.4 shows the comparison of $\Delta\phi$ for $|\Delta\phi| > 2.25$, $|\Delta\phi| > 2$, and no limits on $|\Delta\phi|$; and Figure 7.5 shows the effect on $\langle v_{2,subtracted} \rangle$ when $|\Delta\phi| > 2.25$ and $|\Delta\phi| > 2$. From these values, the χ^2 was found to be 9.0, and this test was thus considered to be a cross check.

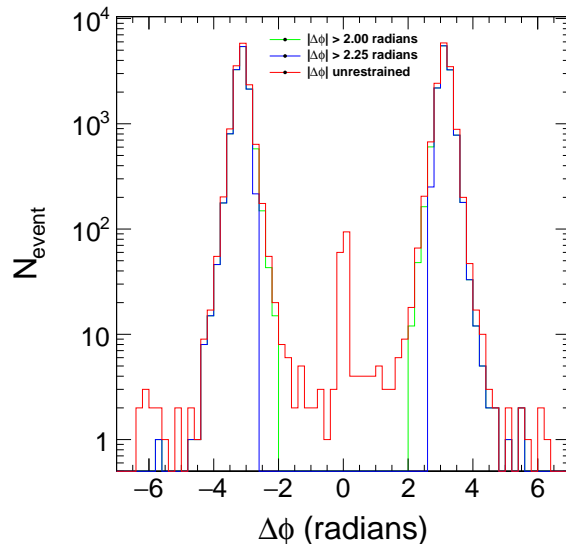


Figure 7.4: $\Delta\phi$ for $|\Delta\phi| > 2.25$, $|\Delta\phi| > 2$, and no limits on $|\Delta\phi|$ are shown here.

7.4 Varying the Vertex Requirement $|v_z|$

The fourth systematic check was performed on the maximum distance from the midpoint of CMS that was allowed (labeled $|v_z|$). For the systematic check on $|v_z|$, the requirement was changed from $|v_z| < 20$ to $|v_z| < 10$, while all other baseline parameters were retained. Figure 7.6 shows the comparison of average dijet p_T for $|v_z| < 10$, $|v_z| < 20$, and no limits on $|v_z|$; and Figure 7.7 shows the effect on $\langle v_{2,subtracted} \rangle$ when $|v_z| < 10$ and $|v_z| < 20$. From these values, the χ^2 was found to be 7.872, a satisfactory cross check.

7.5 Examination of Effect of Setting Limit on Conjugate ZDC

Additionally, the effect of requiring the conjugate ZDC, that is the ZDC that did not register a relatively strong signal in a backward dominant or forward dominant dijet event, to have a signal of < 1000 fC was examined. This was not figured into the final systematic error analysis since the possibility that this could have non-systematic effects could not be ruled out, but was nonetheless thought to be important enough to study. Figure 7.8 shows the effect on $\langle v_{2,subtracted} \rangle$ when the conjugate ZDC had less than 1000 fC for each backward dominant or forward dominant dijet

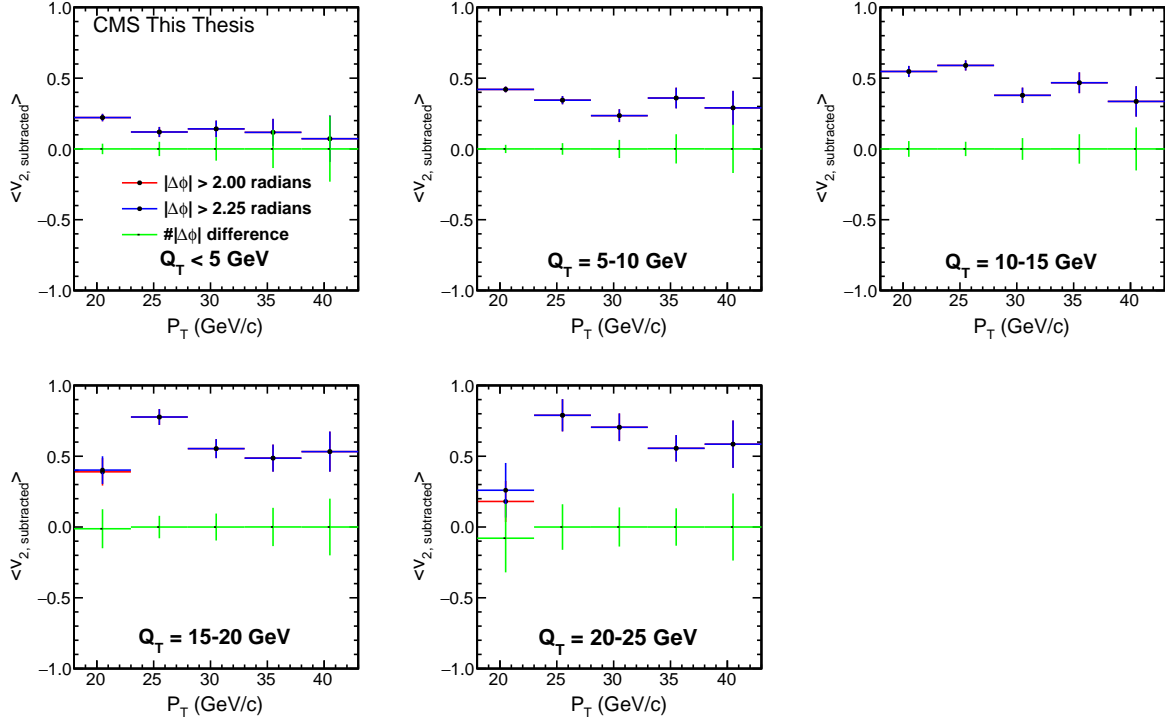


Figure 7.5: $\langle v_{2,subtracted} \rangle$ vs. P_T for Q_T intervals analyzed are shown here for $|\Delta\phi| > 2.25$ and $|\Delta\phi| > 2$.

event as compared to the the baseline rapidity gap requirements for backward dominant events and forward dominant events as stated in Section 6.3.

7.6 Systematic Analysis Results

Table 7.1 summarizes the findings of the systematic analysis. The total systematic uncertainty was determined to be 0.074, with the difference between $v_{2,subtracted}$ for backward dominant and forward dominant events and α being the contributors. Figure 7.9 shows $\langle v_{2,subtracted} \rangle$ with the systematic error bands included. $\langle v_{2,subtracted} \rangle$ is shown because, as stated earlier, the main results were taken to be the average $v_{2,subtracted}$ of backward dominant and forward dominant events.

For the final $\langle v_{2,subtracted} \rangle$ results, it is also important to correct for CMS detector resolution in the determination of Φ . This would involve the application of a resolution correction factor,

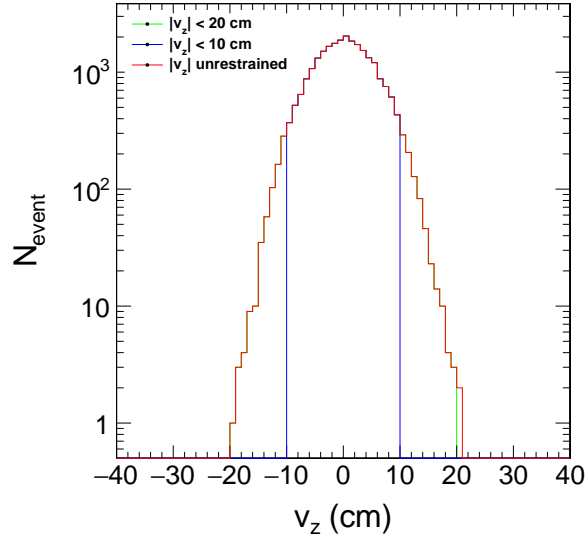


Figure 7.6: Number of events for $|v_z| < 10$, $|v_z| < 20$, and no limits on $|v_z|$ are shown here.

Table 7.1: Systematic Analysis Results on $v_{2,subtracted}$

Systematic Check	χ^2	Statistically Consistent	Systematic Error
Backward/Forward	51.409	No	0.060
α	118.818	No	0.044
$ \Delta\phi $	8.976	Yes	negligible
$ v_z $	7.872	Yes	negligible
Total Systematic Error			0.074

labeled R , to the $\langle v_{2,subtracted} \rangle$ results such that

$$\text{final } \langle v_{2,subtracted} \rangle = \frac{\langle v_{2,subtracted} \rangle}{R}. \quad (7.9)$$

At the time of writing the report on this analysis, studies to determine appropriate R values for the applicable Q_T ranges are ongoing. A Monte Carlo program known as RAPGAP that is instrumental to finding the appropriate R values is in the process of being integrated into CMS [13].

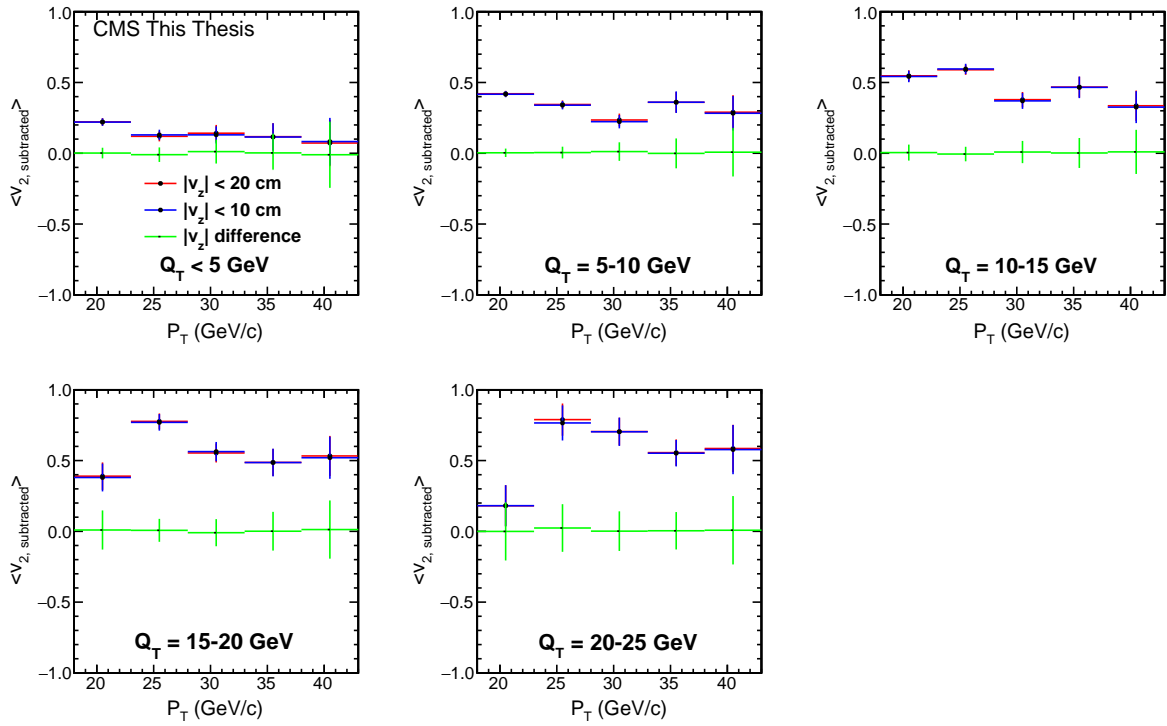


Figure 7.7: $\langle v_{2,subtracted} \rangle$ vs. P_T for Q_T intervals analyzed are shown here for $|v_z| < 10$ and $|v_z| < 20$.

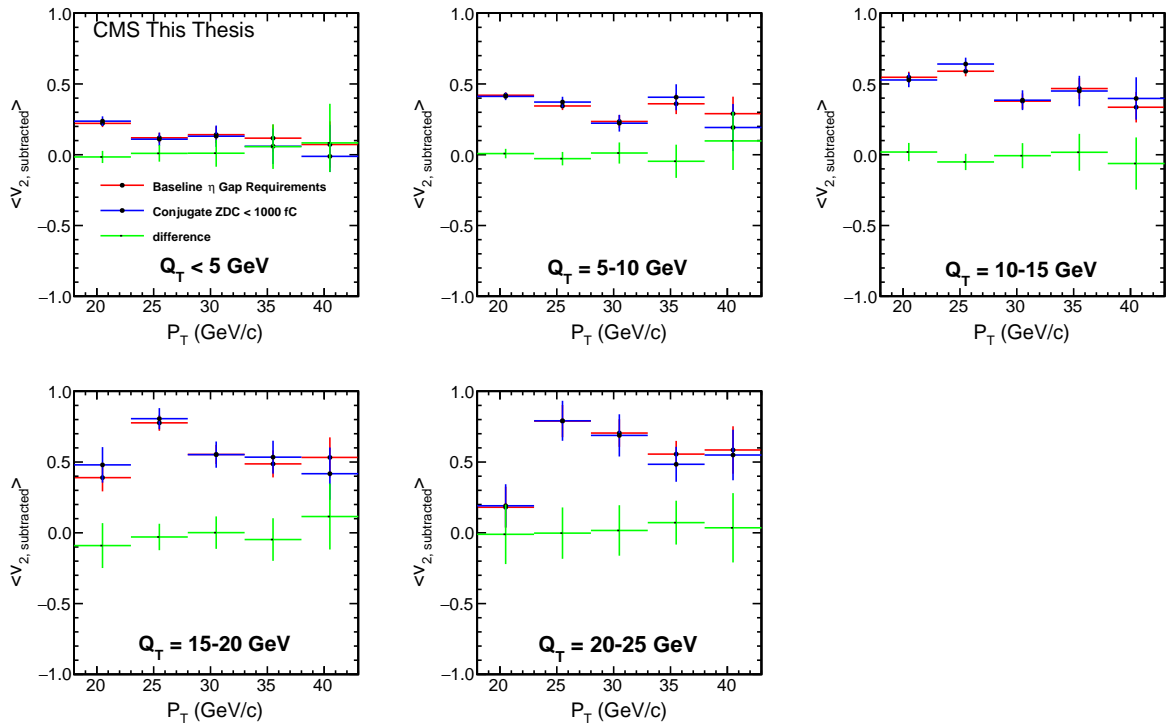


Figure 7.8: $\langle v_{2,subtracted} \rangle$ vs. P_T for Q_T intervals analyzed are shown here for where backward dominant and forward dominant dijet events are required to have less than 1000 fC in the conjugate ZDC as compared to dijet events meeting the baseline backward dominant and forward dominant criteria.

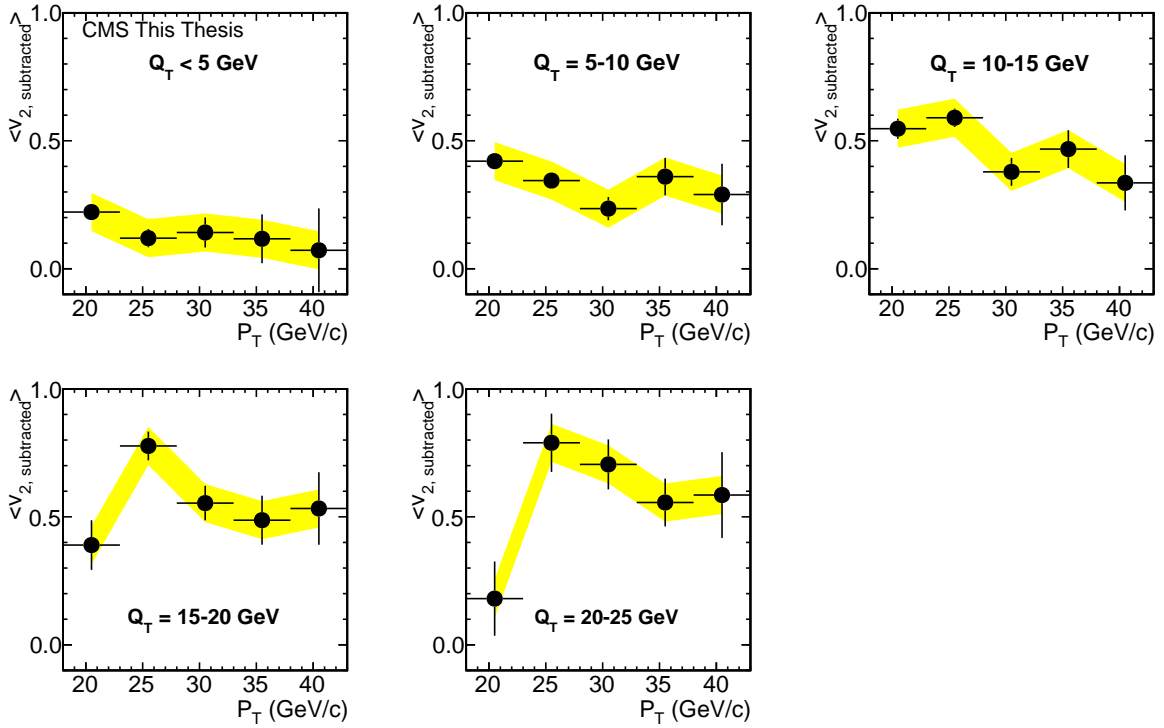


Figure 7.9: $\langle v_{2, \text{subtracted}} \rangle$ with the systematic error bands included are shown here.

Chapter 8

Results and Conclusion

This dissertation presents a measurement of dijets produced in ultra-peripheral lead-lead collisions at $\sqrt{s_{NN}}=5.02$ TeV. The triggers and analysis cuts selected events that had two jets in CMS, a signal in only one HF, an imbalance of signal between ZDC+ and ZDC-, and an η gap in one hemisphere of CMS. In this study, the events were selected where the leading jet had a $p_T > 20$ GeV/c and the subleading jet had a $p_T > 15$ GeV.

There are four principal conclusions that can be drawn from this analysis of this measurement. The first conclusion is that UPCs produce dijet events with where the leading jet has p_T up to at least 100 GeV. The p_T distribution of these dijets is shown in Figure 6.3. The second conclusion is that these events are asymmetric in η , that is they populate either the forward or backward hemispheres of CMS. Figure 6.10 shows the average η distributions and associated ZDC signals for dijets selected by these cuts while Figure 6.12 shows the η gap distribution. The asymmetry is prominently evident in both of these figures. Using the ZDC and HF, photon Bjorken x , gluon Bjorken x , and Q appeared to be determined. The x and Q distributions are also shown in Figure 6.10.

We also focused on the study of the angular correlation between dijet \mathbf{P}_T and \mathbf{Q}_T , i.e., the difference and sum of the dijet p_T values. The presence of a non-zero correlation would be an indication that the two partons that were struck by the incoming photon were correlated. The third conclusion is that there seems to be such a correlation between dijet \mathbf{P}_T and \mathbf{Q}_T . The raw distribution of the angle between \mathbf{Q}_T and \mathbf{P}_T is shown in Figure 6.16. This distribution is not flat, indicating an angular correlation between \mathbf{Q}_T and \mathbf{P}_T . Figure 6.16 has two prominent dips, suggesting a strong second harmonic in the distribution. This harmonic is measured by $\langle v_{2,subtracted} \rangle$.

Figure 8.1 shows $\langle v_{2,subtracted} \rangle$ as a function of P_T and Q_T . It was found that $\langle v_{2,subtracted} \rangle$ is always greater than zero. For $P_T > 23$ GeV/c, $\langle v_{2,subtracted} \rangle$ tends to rise with Q_T and fall with P_T . Further refinement of these positive results is pending the completion of efforts to correct for the resolution of CMS in the measurement of the Φ angle between \mathbf{P}_T and \mathbf{Q}_T .

The fourth conclusion is that the correlation between P_T and Q_T is independent of the neutron signal in the conjugate ZDC. Figure 7.8 shows $\langle v_{2,subtracted} \rangle$ for the baseline analysis and for the events where the conjugate ZDC had less than 1000 fC. The additional cut on the conjugate ZDC does not appreciably affect $\langle v_{2,subtracted} \rangle$. This implies that the physical processes that result in a signal in the conjugate ZDC are separate from those that produce the dijet.

Ongoing and future studies on UPC dijets at CMS could involve the following. Comparison of UPC dijets produced in p-Pb UPCs to those produced in Pb-Pb UPCs could be examined. Increased beam luminosity in the 2018 PbPb data run could result in significantly greater numbers of dijets at higher p_T being measured, which would allow for a viable analysis of v_2 at $P_T > 43$ GeV/c and $Q_T > 25$ GeV/c. Additionally, the theoretical uncertainties concerning whether and how $v_{2,mixed}$ should be subtracted from $v_{2,raw}$ in order to compensate for detector effects need to be addressed. Finally, UPC heavy flavor jets, that is, UPC jets involving bottom quarks, could also be studied [43].

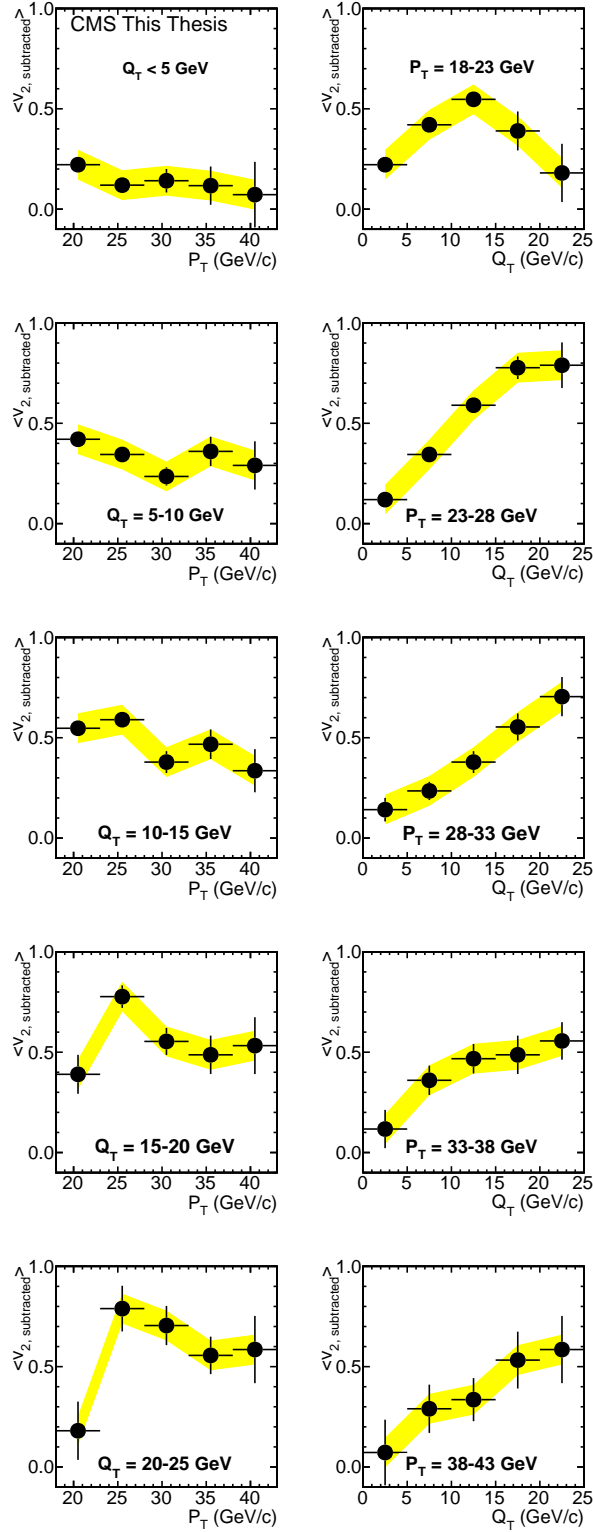


Figure 8.1: $\langle v_{2,subtracted} \rangle$ vs. P_T over Q_T ranges and Q_T over P_T ranges containing the principal signal. A positive $\langle v_{2,subtracted} \rangle$ between Q_T and P_T is generally present.

Bibliography

- [1] "Radiofrequency Cavities". Sep 2012: <http://cds.cern.ch/record/1997424>.
- [2] "HL-LHC Industry", 30 NOV 2017: <https://project-hl-lhc-industry.web.cern.ch/>.
- [3] "Accelerators for Society", 8 December 2017: <http://www.accelerators-for-society.org/case-studies/index.php?id=12>.
- [4] *Applied Engineering Principles, Rev 3*. Bettis Atomic Power Laboratory and Knolls Atomic Power Laboratory, December 1995.
- [5] John Adams et al. "Experimental and theoretical challenges in the search for the quark gluon plasma: The STAR Collaboration's critical assessment of the evidence from RHIC collisions". *Nucl. Phys.*, A757:102–183, 2005.
- [6] K. Adcox et al. "Formation of dense partonic matter in relativistic nucleus-nucleus collisions at RHIC: Experimental evaluation by the PHENIX collaboration". *Nucl. Phys.*, A757:184–283, 2005.
- [7] Ayman Al-bataineh. *J/ψ production in ultra-peripheral proton-lead and lead-lead collisions with CMS*. PhD thesis, University of Kansas, 2017.
- [8] Ahmed Ali, Jens Sören Lange, and Sheldon Stone. "Exotics: Heavy Pentaquarks and Tetraquarks". *Prog. Part. Nucl. Phys.*, 97:123–198, 2017.
- [9] I. Arsene et al. "Quark gluon plasma and color glass condensate at RHIC? The Perspective from the BRAHMS experiment". *Nucl. Phys.*, A757:1–27, 2005.
- [10] B. B. Back et al. "The PHOBOS perspective on discoveries at RHIC". *Nucl. Phys.*, A757:28–101, 2005.

- [11] G. L. Bayatian et al. CMS Physics: Technical Design Report Volume 1: Detector Performance and Software. 2006.
- [12] Carlos A. Bertulani, Spencer R. Klein, and Joakim Nystrand. “Physics of Ultra-Peripheral Nuclear Collisions”. *Annual Review of Nuclear and Particle Science*, 55 (2005):271–310, 13 July 2005.
- [13] Samuel Steed Boren. Ph.D. Candidate, University of Kansas, CMS Heavy Ion Forward Physics Group, 4 June 2018.
- [14] Oliver S. Bruning, P. Collier, P. Lebrun, S. Myers, R. Ostojic, J. Poole, and P. Proudlock. *LHC Design Report Vol.1: The LHC Main Ring*. 2004.
- [15] Matteo Cacciari, Gavin P. Salam, and Gregory Soyez. "The Anti-k(t) jet clustering algorithm". *JHEP*, 04:063, 2008.
- [16] Ivan Amos Cali. "HIL1 Trigger Studies Upgrade", 10 June 2015: <https://twiki.cern.ch/twiki/bin/viewauth/CMS/HIL1TriggerStudiesUpgrade>.
- [17] Mario Campanelli. *Inside CERN's Large Hadron Collider, From the Proton to the Higgs Boson*. World Scientific Publishing Co. Pte. Ltd., Singapore, 2016.
- [18] S. Chatrchyan et al. "Precise Mapping of the Magnetic Field in the CMS Barrel Yoke using Cosmic Rays". *JINST*, 5:T03021, 2010.
- [19] Serguei Chatrchyan et al. "Description and Performance of Track and Primary-Vertex Reconstruction With the CMS Tracker". *JINST*, 9(10):P10009, 2014.
- [20] ALICE Collaboration. “Coherent ρ^0 photoproduction in ultra-peripheral Pb–Pb collisions at $\sqrt{s_{NN}}=2.76$ TeV”. *Journal of High Energy Physics*, 31 March 2015.
- [21] ALICE Collaboration. “Charmonium and e+e- pair photoproduction at mid-rapidity in ultra-peripheral Pb-Pb collisions at $\sqrt{s_{NN}}=2.76$ TeV”. *European Physical Journal C*, 73 (2013):2617, 7 November 2014.

- [22] ALICE Collaboration. “Coherent j/ψ photoproduction in ultra-peripheral Pb-Pb collisions at $\sqrt{s_{NN}}=2.76$ TeV”. *Physics Letters B*, 718 (2013):1273–1283, 8 March 2013.
- [23] CMS Collaboration. *The CERN Large Hadron Collider, Accelerator and Experiments: The CMS Experiment at the CERN LHC*. Institute of Physics Publishing and SISSA, <http://www-spires.fnal.gov/spires/find/books/www?cl=QC787.P73C37::2009>, 2008.
- [24] CMS Collaboration. “CMS Detector Design”, 23 November 2011: <http://cms.web.cern.ch/news/cms-detector-design>.
- [25] CERN Education Communications and Outreach Group. “LHC faq the guide”, 30 NOV 2017: <http://cds.cern.ch/record/2255762/files/CERN-Brochure-2017-002-Eng.pdf>.
- [26] Enrico Fermi. “Über die Theorie des Stoßes zwischen Atomen und elektrisch geladenen Teilchen.”. *Zeitschrift für Physik*, 29 (1924):315–327, December 1924.
- [27] Francois Gelis, Edmond Iancu, Jamal Jalilian-Marian, and Raju Venugopalan. “The Color Glass Condensate”. *Ann. Rev. Nucl. Part. Sci.*, 60:463–489, 2010.
- [28] Victor P. Gonçalves. “photon induced interactions at the LHC”. In *New trends in high energy physics and QCD school; International Institute of Physics, Federal University of Rio Grande do Norte; Natal, Brazil*, 21-31 October 2014.
- [29] David J. Griffiths. *Introduction to Electrodynamics, Third Edition*. Prentice Hall, Inc., Upper Saddle River, NJ, Upper Saddle River, NJ, U.S.A., 1999.
- [30] David J. Griffiths. *Introduction to Elementary Particles, Second, Revised Edition*. WILEY-VCH Verlag GmbH and Co. KGaA, Weinheim, Weinheim, Baden-Württemberg, F.R.G., 2008.
- [31] Miklos Gyulassy and Larry McLerran. “New forms of QCD matter discovered at RHIC”. *Nucl. Phys.*, A750:30–63, 2005.

- [32] Yoshikazu Hagiwara, Yoshitaka Hatta, Roman Pasechnik, Marek Tasevsky, and Oleg Teryaev. Accessing the gluon wigner distribution in ultraperipheral pa collisions. *Phys. Rev.*, D96(3):034009, 2017.
- [33] Jr. Humphries, Stanley. *Principles of Charged Particle Acceleration*. John Wiley and Sons, Inc., New York, NY, U.S.A., 1986.
- [34] Bora Isildak. *Measurement of the Differential Dijet Production Cross Section in Proton-Proton Collisions at $\sqrt{s} = 7$ TeV*. PhD thesis, Bogazici U., 2011.
- [35] John David Jackson. *Classical Electrodynamics, Third Edition*. John Wiley and Sons, Inc., Hoboken, NJ, U.S.A., 1999.
- [36] Japan Joint Institute for Computational Fundamental Science, University of Tsukuba. "Getting to the Heart of Matter", 2011: <http://www.jicfus.jp/en/promotion/pr/mj/guido-cossu>.
- [37] L. M. Jones and H. W. Wyld. "Charmed Particle Production by Photon Gluon Fusion". *Phys. Rev.*, D17:759, 1978.
- [38] P. Kovtun, Dan T. Son, and Andrei O. Starinets. "Viscosity in strongly interacting quantum field theories from black hole physics". *Phys. Rev. Lett.*, 94:111601, 2005.
- [39] T. D. Lee and G. C. Wick. "Vacuum Stability and Vacuum Excitation in a Spin 0 Field Theory". *Phys. Rev.*, D9:2291–2316, 1974.
- [40] Michael E. Peskin and Daniel V. Schroeder. *An Introduction to Quantum Field Theory*. Westview Press, www.westviewpress.com, 1995.
- [41] Arthur M. Poskanzer and S. A. Voloshin. Methods for analyzing anisotropic flow in relativistic nuclear collisions. *Phys. Rev.*, C58:1671–1678, 1998.
- [42] Philipp Schieferdecker. "Jet Algorithms", 17 April 2009: <https://twiki.cern.ch/twiki/bin/view/Sandbox/PhilippSTalk>.

- [43] Mark Strikman, Ramona Vogt, and Sebastian N. White. “Probing small x parton densities in ultraperipheral AA and pA collisions at the LHC”. *Phys. Rev. Lett.*, 96:082001, 2006.
- [44] Ramona Vogt. *Ultrarelativistic Heavy Ion Collisions*. Elsevier B. V., Oxford, U.K., 2007.
- [45] C. F. von Weizsäcker. “Ausstrahlung bei Stößen sehr schneller Elektronen.”. *Zeitschrift für Physik*, 88 (1934):612–625, September 1934.
- [46] E. J. Williams. “Nature of High Energy Particles of Penetrating Radiation and Status of Ionization and Radiation Formulae”. *Physical Review*, 45 (1934):729–730, 1934.
- [47] Edmund Wilson. *An introduction to Particle Accelerators*. Oxford University Press, Oxford, U.K., 2001.